Theses and Dissertations | 1. Thesis and Dissertation Collection, all items

2000-03

A comparison of output from the Los Alamos National Laboratory (LANL) Parallel Ocean Program (POP) model with surface velocity data from drifting Buoys in the North Atlantic Ocean

Pelton, Jimmy W.

Monterey, California. Naval Postgraduate School

http://hdl.handle.net/10945/7648

NAVAL POSTGRADUATE SCHOOL
Monterey, California

THESIS

A COMPARISON OF OUTPUT FROM THE LOS ALAMOS
NATIONAL LABORATORY (LANL) PARALLEL OCEAN
PROGRAM (POP) MODEL WITH SURFACE VELOCITY
DATA FROM DRIFTING BUOYS IN THE
NORTH ATLANTIC OCEAN

by

Jimmy W. Pelton

March 2000

Thesis Advisor: Julie L. McClean

REPORT DOCUMENTATION PAGE

Public reporting burden for this collection of information is estimated to average 1 hour per response, including the time for reviewing instruction, searching existing data sources, gathering and maintaining the data needed, and completing and reviewing the collection of information. Send comments regarding this burden estimate or any other aspect of this collection of information, including suggestions for reducing this burden, to Washington headquarters Services, Directorate for Information Operations and Reports, 1215 Jefferson Davis Highway, Suite 1204, Arlington, VA 22 202-4302, and to the Office of Management and Budget, Paperwork Reduction Project (0704-0188) Washington DC 20503.

1. AGENCY USE ONLY *(Leave blank)*	2. REPORT DATE March 2000	3. REPORT TYPE AND DATES COVERED Master's Thesis

4. TITLE AND SUBTITLE A Comparison Of Output From The Los Alamos National Laboratory (LANL) Parallel Ocean Program (POP) Model With Surface Velocity Data From Drifting Buoys in the North Atlantic Ocean	5. FUNDING NUMBERS
6. AUTHOR(S) Pelton, Jimmy W.	

7. PERFORMING ORGANIZATION NAME(S) AND ADDRESS(ES) Naval Postgraduate School Monterey, CA 93943-5000	8. PERFORMING ORGANIZATION REPORT NUMBER

9. SPONSORING / MONITORING AGENCY NAME(S) AND ADDRESS(ES)	10. SPONSORING / MONITORING AGENCY REPORT NUMBER

11. SUPPLEMENTARY NOTES

The views expressed in this thesis are those of the author and do not reflect the official policy or position of the Department of Defense or the U.S. Government.

12a. DISTRIBUTION / AVAILABILITY STATEMENT Approved for public release; distribution is unlimited.	12b. DISTRIBUTION CODE

13. ABSTRACT *(maximum 200 words)*

Surface velocity fields from two configurations of the Los Alamos National Laboratory (LANL) Parallel Ocean Program (POP) model are compared to surface velocity data from satellite-tracked buoys in the North Atlantic. Separate analyses are conducted for each model configuration. In the first analysis, output from a 1/6-degree, 20-level model version is compared with five years (1993-1997) of drifter data, based on both Eulerian and Lagrangian statistics. In the second analysis, newly-available output from a 1/10-degree, 40 level version is compared to a two-year subset (1993-1994) of the data, and to 1/6-degree output over the same time frame. The latter comparison is based on Eulerian statistics alone.

The five-year comparison shows that the 1/6-degree model produces inaccuracies in some features, and generally underestimates velocity variance. Modeled Lagrangian time scales are too long, while the length scales are too short. The two-year comparison shows that at the higher vertical and horizontal resolution of the 1/10-degree model, there is a striking improvement in the spatial distribution of energy and resolution of the variance field.

14. SUBJECT TERMS Numerical Modeling, Ocean Forecasting, Model Evaluations	15. NUMBER OF PAGES 155
	16. PRICE CODE

17. SECURITY CLASSIFICATION OF REPORT Unclassified	18. SECURITY CLASSIFICATION OF THIS PAGE Unclassified	19. SECURITY CLASSIFICATION OF ABSTRACT Unclassified	20. LIMITATION OF ABSTRACT UL

NSN 7540-01-280-5500

Standard Form 298 (Rev. 2-89)
Prescribed by ANSI Std. 239-18 298-102

A COMPARISON OF OUTPUT FROM THE LOS ALAMOS NATIONAL LABORATORY (LANL) PARALLEL OCEAN PROGRAM (POP) MODEL WITH SURFACE VELOCITY DATA FROM DRIFTING BUOYS IN THE NORTH ATLANTIC OCEAN

Jimmy W. Pelton
Lieutenant, United States Navy
B.S. North Carolina State University, 1993

Submitted in partial fulfillment
of the requirements for the degree of

MASTER OF SCIENCE IN OPERATIONS RESEARCH

from the

NAVAL POSTGRADUATE SCHOOL
March 2000

ABSTRACT

Surface velocity fields from two configurations of the
Los Alamos National Laboratory (LANL) Parallel Ocean Program
(POP) model are compared to surface velocity data from
satellite-tracked buoys in the North Atlantic. Separate
analyses are conducted for each model configuration. In the
first analysis, output from a 1/6-degree, 20-level model
version is compared with five years (1993-1997) of drifter
data, based on both Eulerian and Lagrangian statistics. In
the second analysis, newly-available output from a 1/10-
degree, 40 level version is compared to a two-year subset
(1993-1994) of the data, and to 1/6-degree output over the
same time frame. The latter comparison is based on Eulerian
statistics alone.

The five-year comparison shows that the 1/6-degree
model produces inaccuracies in some features, and generally
underestimates velocity variance. Modeled Lagrangian time
scales are too long, while the length scales are too short.
The two-year comparison shows that at the higher vertical
and horizontal resolution of the 1/10-degree model, there is
a striking improvement in the spatial distribution of energy
and resolution of the variance field.

TABLE OF CONTENTS

EXECUTIVE SUMMARY

To meet future Navy operational ocean forecasting requirements, a high-resolution, coupled air/ocean/ice model with data assimilation capability will be needed. Current-generation ocean general circulation models have evolved to a point that suggests evaluating them for this role. The Los Alamos National Laboratory's (LANL) Parallel Ocean Program (POP) is one of the ocean models currently under consideration by the Office of Naval Research (ONR). The purpose of this study is to evaluate the ability of the POP to reproduce surface features and processes of interest to the Navy, by statistical comparison of its velocity fields to those of surface drifters in the North Atlantic Ocean.

We compare output from a 1/6-degree, 20-level version of the model to five years of drifter data spanning the period January 1, 1993 to December 31, 1997, on the basis of Eulerian and Lagrangian statistics. Trajectories for the Lagrangian analysis are generated by numerical integration, using bilinear interpolation over the model's discrete velocity fields.

To assess the effect of increased horizontal and vertical resolution in the model, we use Eulerian statistics to compare two years of newly-available output from a 1/10-degree, 40-level model run to the first two years of the drifter data.

The Eulerian analysis of the 1/6-degree model indicates that this version performs best at higher latitudes (roughly north of 60°N); the northern boundary currents are particularly well represented. Model effects noted in previous studies (a spurious anticyclone and front, and a displaced northward branching of the Gulf Stream) distort the mean flow in other locations. The spatial distribution of mean kinetic energy (MKE) is likewise distorted, although the frequency distribution of MKE and the total MKE over the ocean appear to be basically correct. Mean flow vector diagrams show the model fails to capture much of the disorganized nature of surface flow in the North Atlantic. This observation is reflected in plots of standard deviation ellipses, which show the model's variance to be low over most of the North Atlantic, particularly so in the south and southeast Subtropical Gyre.

Lagrangian integral time scales for the 1/6-degree model are overestimated, on average, by factors of about about 1.9 and 1.8 in the zonal and meridional directions, respectively. Integral length scales are slightly underestimated on average, by factors of slightly greater than unity and about 1.2 in the zonal and meridional directions, respectively.

The higher vertical and horizontal resolution of the 1/10-degree model make a significant improvement in the spatial distribution of energy and representation of the mean flow. The magnitudes of variance are greatly improved,

the rich eddy structure of the Gulf Stream evident, and the complex recirculation patterns of the mid-Subtropical Gyre much closer to that revealed by the drifters. The weak Azores Front is resolved in the 1/10-degree model, whereas it was absent in the 1/6-degree model. The spurious features of the 1/6-degree model are either absent or greatly attenuated in the 1/10-degree version.

Our evaluation indicates that the displaced branching of the North Atlantic Current, spurious circulation effects, under-resolved variability, and limited feature definition of the 1/6-degree model make it inadequate for use in a global coupled forecasting model. Although the 1/10-degree comparison is considered preliminary on the basis of its abbreviated time domain, the results of the higher resolution run clearly indicate substantial improvement in the above areas and are strong enough to nominate the 1/10-degree model for consideration in the coupled system.

ACKNOWLEDGMENT

I.   INTRODUCTION

The paradigm for Navy forecasting of ocean conditions in the next millennium is that of a global high-resolution atmosphere/ocean/ice coupled model with the ability to assimilate data. Currently computer resources are unavailable for such as system; however, as multi-processor super computing technology continues to evolve, it is appropriate to evaluate candidate high-resolution global ocean models for potential use in a coupled forecasting system. This is done by quantitatively assessing the ability of the models to reproduce features and processes with short time scales (up to 2 weeks). In this thesis we evaluate one particular high-resolution model, the Los Alamos National Laboratory (LANL) Parallel Ocean Program (POP) model. Two different formulations are considered, a 1/6-degree near-global version, and a recent advancement of a 1/10-degree version covering only the North Atlantic Ocean.

Surface drifting buoys provide one of several standards by which to assess the fidelity of general circulation models in representing ocean flow. The frame of comparison they offer is unique, as they suffer neither the immobility of moored instruments nor the coarser temporal resolution (~10 day resampling period) associated with altimetry. Drifter data have been archived for well over two decades and some regions, the North Atlantic Ocean basin in particular, have been extensively sampled. An improved method for conditioning raw drifter data, in place since

1996 (Hansen and Poulain, 1996), has produced a large, consistent data set of velocity values. These are provided as uniform six-hour time series, facilitating both Eulerian and Lagrangian computations. This study compares output from the 1/6-degree and 1/10-degree models to data from North Atlantic surface drifters on the basis of Eulerian and Lagrangian velocity statistics.

Previous comparisons of the 1/6-degree POP model to actual data sources include TOPEX/POSEIDON (T/P) altimetry (McClean et al., 1997), Pacific basin surface drifters (Lemon, 1997), current meters and altimetry (T/P and GEOSAT) (Maltrud et al., 1998), and tide gauges (Tokmakian, 1996). The 1/10-degree model has been compared to satellite altimetry data and various in situ sources, and intercompared with the 1/6-degree model (Smith et al., 1999).

The purpose of this study is to provide an independent assessment of the model's reproduction of the North Atlantic surface circulation in both the 1/6-degree and 1/10-degree versions. The results of this analysis will address the tradeoff between adequate grid resolution and the need to minimize machine time and memory; the latter concern is significant as we consider a global coupled forecasting system. Specific objectives of the study are to characterize regions of agreement and disagreement between model and data, assign likely causes for areas of significant

departure, and to determine locations where the 1/6-degree formulation is adequate.

Several intercomparison schemes are used, based on the following data and model output:

1.   Actual drifter velocities at each recorded track point, referred to simply as "drifter data".

2.   Velocities obtained from numerically simulated (appendix A) trajectories calculated from the 1/6-degree model's velocity fields. The modeled particles are "released" at the same locations and times as their real counterparts. This set of trajectories will be referred to by the name "same start".

3.   Modeled drifter velocities, as in (2), but using random start times and locations. There are 615 random deployments, corresponding in quantity to the actual drifter releases. The record lengths of these simulated drifters are also randomized, following an exponential distribution with mean lifetime equal to that of the actual drifters. This trajectory set will be referred to by the term "random start".

4.   Velocities at model grid points closest to actual drifter measurements in time and space. The extraction of these velocities was done by applying a binary mask to the model lattice, hence this output will be referred to as "masked". Masked output sets are generated using both the 1/6-degree model grid and the 1/10-degree model grid.

A comparison between 1 and 4 (both 1/6 and 1/10 model versions) will be made on the basis of Eulerian, or location based, statistics. Lagrangian, or trajectory-based, statistics will be used to compare 1 with 2. Because only two years of 1/10-degree model output were available at the time of these analyses, only Eulerian comparisons are made

for this version. A full description of the Eulerian and Lagrangian statistics is given in Chapter IV.

Finally, a comparison between sets 2 and 3 will give a rough estimate of the degree of bias incurred in the 1-2 comparison through differences in deterministic and random sampling patterns.

The model/data comparisons are made quantitatively, and simple statistical rejection tests for equal means are conducted under the null hypothesis that the model output does not significantly differ from the actual data. This approach is conservative in that it seeks to identify areas of significant deficiency in the model's representation of the surface circulation.

Chapter II provides an overview of the surface circulation of the North Atlantic Ocean, including relatively recent findings. It is provided as a framework for understanding our results and those of others cited. Chapter III gives a history and description of both 1/6-degree and 1/10-degree models, and describes the drifter data set. A review of previous POP comparisons is also provided. Chapter IV presents the methods used in the Eulerian analysis, and describes our results. Chapter V describes the methods and results of the Lagrangian analysis. Finally, Chapter VI summarizes our findings and offers recommendations.

II. SYNOPSIS OF CIRCULATION AND ITS VARIABILITY IN THE NORTH ATLANTIC OCEAN

This section is intended to familiarize the reader with the mean circulation patterns and variability in the North Atlantic ocean, as an aid to understanding the findings of this work and others cited. Figure 1 illustrates the major currents referenced herein. Figure 2 shows the topography of the Atlantic Ocean.

The basin-wide mean circulation is driven by two gyres, the North Atlantic Subpolar and Subtropical Gyres, themselves driven by the large-scale wind stress curl. The Subpolar Gyre consists of the East Greenland Current (EGC) and West Greenland Current (WCG) to the north, the Labrador Current to the west, the North Atlantic Current (NAC) to the south, and the Irminger Current (IC) to the east. The Subtropical Gyre is formed by the Gulf Stream to the west and northwest, the NAC to the northeast, the Portugal and Canary Currents to the west, the North Equatorial Current (NEC) to the south, and the Antilles Current and Florida Current to the southwest. There are additionally recirculation currents within the gyre, which transport water toward the NEC.

The two gyres meet in a broad confluence south of the Newfoundland Grand Banks. Here cold, relatively fresh water from the Labrador shelf comes into contact with the warmer, more saline waters of the Sargasso Sea. It is a site of intense eddy activity, where Gulf Stream meanders form both
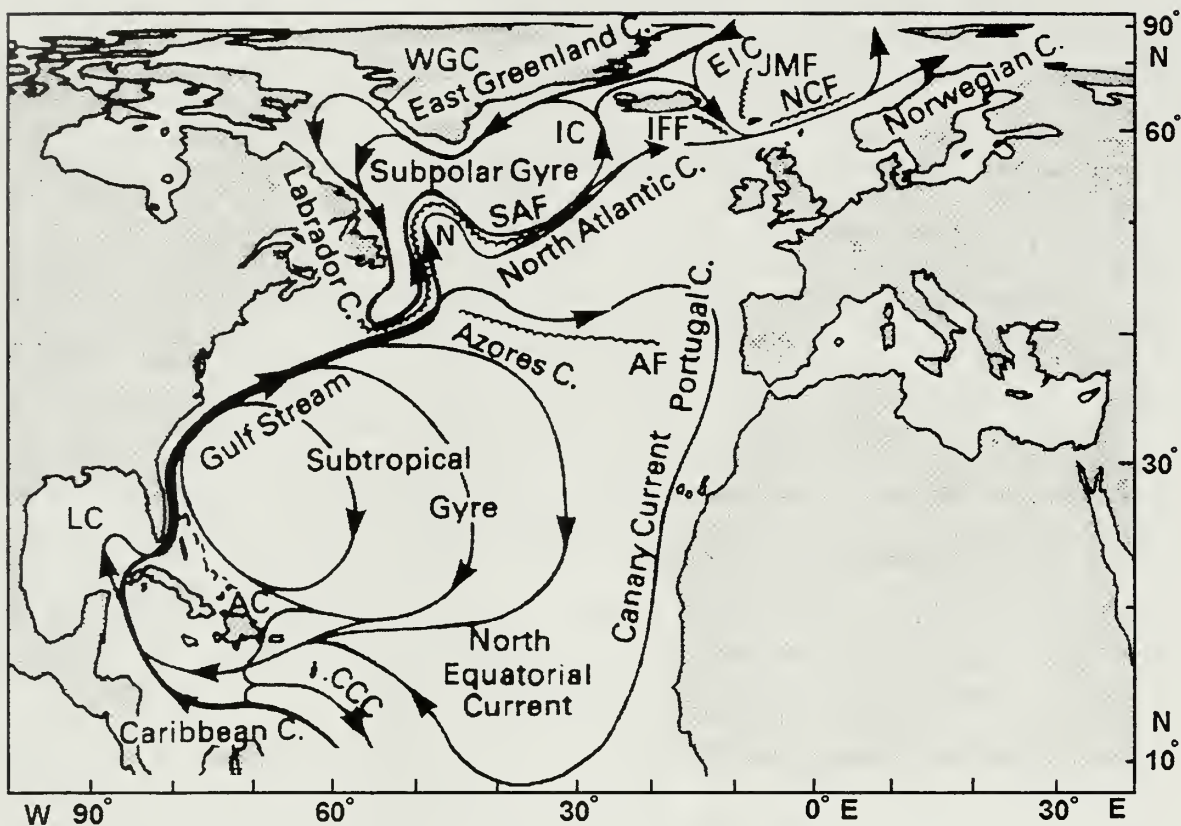
Figure 1. Mean Currents and Fronts of the North Atlantic Ocean. Abbreviations used are for the East Iceland Current (EIC), East Greenland Current (EGC), West Greenland Current (WGC), Irminger Current (IC), Antilles Current (AC), Loop Current (LC), Caribbean Countercurrent (CCC), Jan Mayen Front (JMF), Norwegian Current Front (NCF), Iceland-Faroe Front (IFF), Subarctic Front (SAF), and Azores Front (AF). After Tomczak and Godfrey, (1994).

6
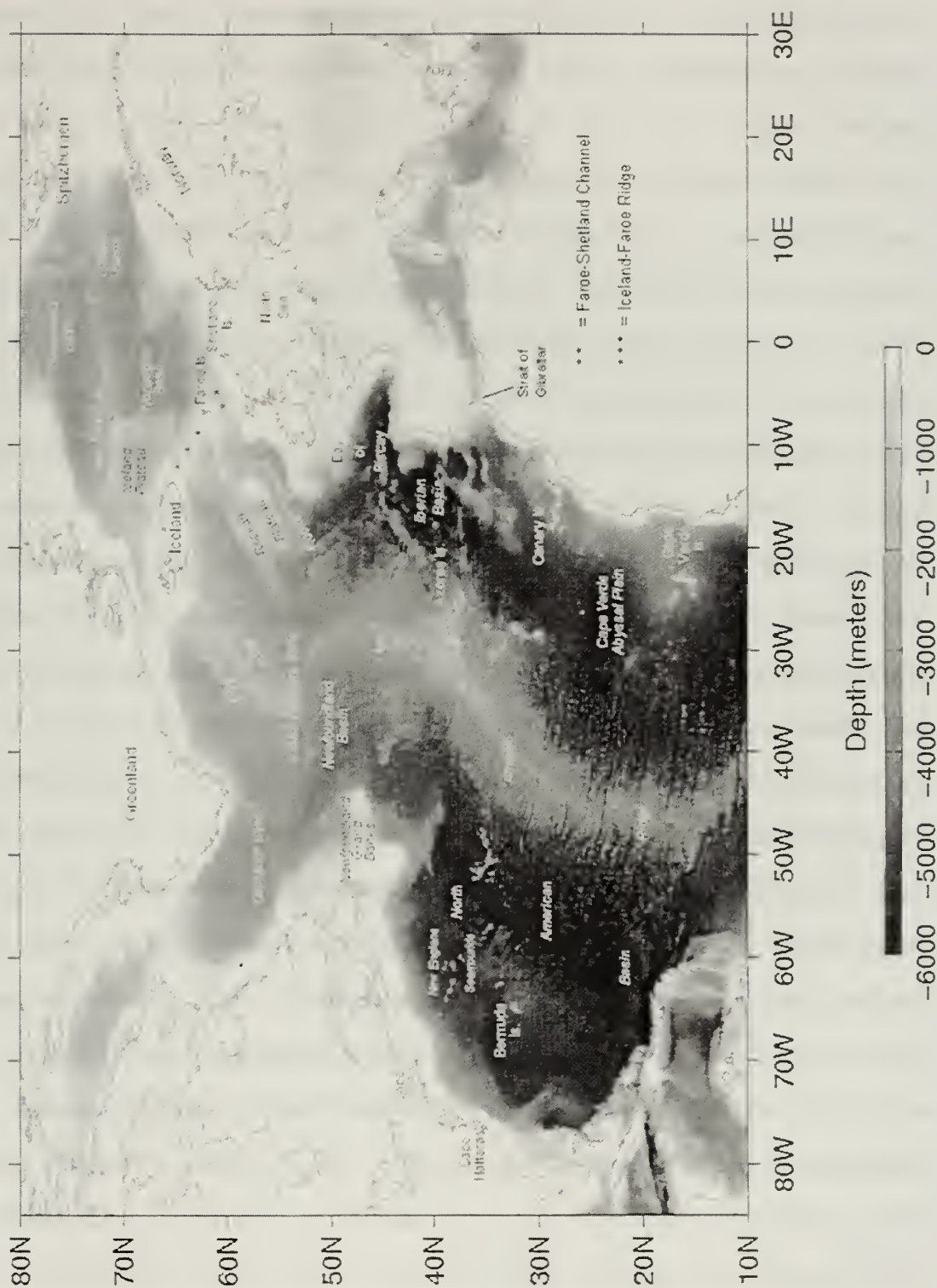
Figure 2. Bottom topography of the North Atlantic Ocean.
Bathymetry is from the ETOPO5 database, courtesy of the
National Oceanographic Data Center.

7

cyclonic and anticyclonic rings, transporting cold shelf water southward and warm Sargasso water northward, respectively.

The greatest current velocities in the Atlantic Ocean are observed in the Gulf Stream, specifically between Cape Hatteras and Cape Cod. Johns et al.(1995) analyze the output from an array of 13 current meters in this area, finding a maximum velocity of about 200 cm/s at the surface, decreasing to 70 cm/s at 1000 m. It is noteworthy that Johns et al. (1995) employ a "stream-coordinate" system, where the coordinate axes are always aligned with the instantaneous direction of the Gulf Stream. They point out that a simple Eulerian averaging with bins aligned to the standard axes will give an inaccurate picture of the mean flow if any recirculations or counterflows are present, whereas the stream-coordinate method will separate these effects from the larger flow. Richardson (1983) makes a related point regarding averages, namely, that resolving long-term mean velocities in the Atlantic requires enormous amounts of data. This is because most of the energy is contained in the eddy field rather than the mean field, and because the dominant time scales are in the range 30-100 days. Richardson's (1983) study of eddy kinetic energy (EKE) in the Atlantic gives a peak value in the Gulf Stream of 3000 cm^2/s^2, based on a 2°x2° binning scheme, where large amplitude meanders begin to form at 37°N, 67°W. He further identifies three high energy tongues associated with the

Stream's downstream course, the strongest coinciding with its flow around the Grand Banks into the Newfoundland Basin.

The Gulf Stream exhibits pronounced temporal and spatial variability. The Florida Current, which feeds into the Gulf Stream, shows significant seasonal variability in transport levels, with March volume transports 11 Sverdrup (Sv) higher than in November (Tomczak and Godfrey, 1994). Larson and Bushnell (1995) also demonstrate decade-scale variations in Florida Current transport. Spatially, mean transports increase from about 30 Sv off Miami, Florida (Niiler and Richardson, 1973) to a maximum of 150 Sv near 65°W (Worthington, 1976) due to contributions from gyre recirculation and cold-core ring reabsorption. Thereafter the Gulf Stream begins to lose flow to Sargasso Sea recirculation and ring formation, decreasing to 120 Sv by the Tail of the Grand Banks (Worthington, 1976). Finally, there is substantial variability in the Gulf Stream's location, on both annual and interannual scales. In a five-year survey, Auer (1987) shows the mean position between 70°W and 44°W to reach a northern extreme in September and a southerly limit in February, with the magnitude of the annual shifts increasing to a maximum near the Newfoundland Grand Banks.

The part of the subtropical gyre just east of 50°W is known as the Gulf Stream Extension. Here the North Atlantic Current (NAC) breaks off as a northward flow, makes an acute turn to the southeast, then just as sharply veers to the

northeast. This sinuous course forms a loop in the vicinity of 50°N, 42°W which has become known as the "Northwest Corner". Beyond this point, the NAC continues as a frontal jet reaching velocities of 100 cm/s (Krauss, 1986). Southward of the jet a strong eddy field extends westward to the Mid-Atlantic Ridge. EKEs in this field, based on a 3°x3° grid, range from 1500 cm^2/s^2 south of Newfoundland to 600 cm^2/s^2 in the Northwest Corner to 300 cm^2/s^2 at the Mid-Atlantic Ridge (Krauss and Käse, 1984).

As the NAC continues to the northeast it loses flow to the northward-flowing Irminger Current, which branches off Southwest of Iceland. It then sheds a small amount of flow to the south, which supplies the Portugal and Canary currents. By this point the NAC has slowed and diffused into a slow northeast drift in the direction of Scotland (Pickard and Emery, 1990).

The region to the west and southwest of Iceland is characterized by low, seasonally variable velocities generally below 5 cm/s and punctuated by a band of EKE of about 200 cm^2/s^2 (based on 2° longitude, 1° latitude bins) coinciding with the Sub-Arctic Front (SAF) (Otto and Van Aken, 1996). The currents west of Iceland and around the tip of Greenland are primarily driven by thermohaline gradients, with speeds of up to 70 cm/s observed in the outer edges of both the East and West Greenland Currents (Krauss, 1995).

The Norwegian Atlantic Current (NwAtC), also called the Norwegian Current, is formed as the convergence of the NAC

and the East Iceland Current (EIC), with additional contribution from a weak northeast drift to the west of the Iceland-Faroe Front (IFF). Within a rectangle bounded roughly by Iceland, Norway, Spitzbergen, and the east coast of Greenland are the Greenland, Iceland, and Norwegian Seas, collectively called the Nordic Seas. Beneath these lie the Norwegian, Greenland and Lofoten Basins, and the Iceland Plateau. The seas are bounded on the east by the West Spitzbergen Current, a branch of the NwAtC, and to the north by the EGC. Poulain et al. (1996), study the tracks of 107 drifters released in the vicinity of Iceland and the IFF. The tracks reflect earlier evidence that the NwAtC passes along the coast of Norway as separate coastal and continental margin flows. They measure maximum velocities of over 110 cm/s where the flow branches reassimilate off the north end of the Norwegian peninsula. The currents along the entire periphery of the seas appear to be driven by sharp thermohaline fronts, though the authors also reveal topography to be a major influence. In particular, Poulain et al. (1996) identify a western branch of the NwAtC deflected by sloping bathymetry into the region of Jan Mayen Island, and the segregation of the larger circulation into separate sub-basin gyres by submarine ridges. Finally, their study shows EKE to scale roughly with the mean flow in this region, with maximum values close to 700 cm^2/s^2 (based on 2° longitude, 1° latitude bins), corresponding to the maximum flow found off the northwest Norwegian coast. The Iceland

Plateau, in contrast, is distinctively low in both mean kinetic energy (MKE) and EKE.

The drifter study of Poulain et al. (1996) represents one of many that have greatly aided our knowledge of the North Atlantic circulation. Richardson (1983), using 110 buoys, maps EKE across the entire North Atlantic basin, revealing the rich turbulent structure of the Gulf Stream and noting that EKE measurements from ship drift underestimate the true values by a factor of about two. In a similar study of the eastern North Atlantic, Krauss and Käse (1984) identify a homogeneous pool of low EKE water (less than 100 cm^2/s^2, based on a 3°x3° grid) southward of about 40°N, in agreement with Richardson's (1983) 2°x2° measurements of 100 cm^2/s^2 in the eastern North Atlantic and North Equatorial Current, and 200 cm^2/s^2 in mid-gyre.

The works of Krauss (1995) and Otto and Van Aken (1995) have already been cited; additionally, both studies clearly reveal an northeastward flow in the region south of Iceland, which divides at the Faroe Islands to enter the Norwegian Sea via the Iceland-Faroe Ridge and the Faroe-Shetland Channel. Krauss' (1995) drifters also show the Irminger Current to split into westward and eastward flowing branches at the Reykjanes Ridge. Both these studies add valuable insight, as knowledge about the weak currents in this region is particularly poor.

Colin de Verdiere (1983) investigates the Lagrangian properties of 16 drifters deployed in a 100 km diameter area

in the eastern North Atlantic, finding good agreement up to 30 days with homogeneous dispersion theory. Based on centers of gravity of energy spectra, Lagrangian time scales are about 12 days, and Eulerian time scales about 26 days. Krauss and Böning (1987) study the tracks of 113 drifters in eddy field associated with the Gulf Stream Extension, again finding good agreement with homogeneous dispersion theory over 60 days, and a decreasing trend in Lagrangian time scales from the subtropics to the NAC. They find eddy length scales to be fairly homogeneous across the Atlantic, and eddy diffusivity (the integral of the Lagrangian autocovariance) to increase by a factor of about four from 30°N to 50°N.

THIS PAGE INTENTIONALLY LEFT BLANK

III. MODEL OUTPUT AND DRIFTER DATA SETS

A.   MODEL DESCRIPTION, OUTPUT, AND PREVIOUS COMPARISONS

The POP model is a 3-dimensional, z-level, eddy-resolving, primitive equation ocean general circulation model. The code derives from that developed by Bryan (1969), Cox (1970, 1984) and Semtner (1974). Semtner and Chervin (1988) modify the code for a 1/2° grid and improve the realism of the topography. Further refinements produce a 1/4° version (Semtner, 1997) which includes a free surface formulation by Killworth et al. (1991) to allow the use of unsmoothed topography. These improvements increase the model's EKE and topographically-related eddy energy in the Southern Ocean, where comparisons to Geosat altimetry had indicated deficits (Wilken and Morrow, 1994).

The 1/6-degree, 20 level, POP model is a further refinement of this 1/4° version; it is reformulated for massively parallel architecture (Smith et al., 1992) and uses an implicit free-surface method for the barotropic mode (Dukowicz and Smith, 1994). The spatial domain extends from 75°S-65°N to 77°S-77°N. Salinity and temperature restoring to Levitus (1982) climatology is implemented over the upper kilometer of the water column in the zone poleward of latitude 70° (Maltrud et al., 1998).

A higher resolution 1/10°, 40-level simulation of the North Atlantic only is run by Smith et al. (1999). The spatial domain is 20°S - 72°N, 98°W - 17°E, which includes

the Gulf of Mexico and the western Mediterranean Sea. The 1/10°, 40-level North Atlantic run evaluated in this study is an advancement of the above model; it includes the mixed layer formulation known as K-Profile Parameterization (KPP) developed by Large et al. (1994). This later run is forced with daily wind stresses from the Navy Operational Global Atmospheric Prediction System (NOGAPS), while the former run is forced with wind stresses from the European Centre for Medium Range Weather Forecasts (ECMWF). For clarity in the following discussion, the latter will be referred to as the NOGAPS version and the former the ECMWF version.

1.   Forcing and Equilibration: 1/6-Degree Model

Semtner's (1997) 1/4-degree model is initialized using the output from a 35 year integration at 1/2°, (which in turn is initialized from Levitus (1982) climatology), and a subsequent 5 year equilibration at 1/4°. Following a 3-year run, the end state is interpolated to 1/6° resolution and used to initialize the 1/6° version, which is allowed to equilibrate for 5 years. (McClean et al., 1997)

Three consecutive runs (POP5, POP7, POP11) are made at 1/6°, with the last three initialized from snapshots of the end state of their predecessors. The three sequential runs are made to investigate the effects of different wind and heat forcings. Salinity and temperature restoration is obtained by interpolation from Levitus (1982) monthly climatology, and wind forcing fields are interpolated from

16

2.5° wind grids provided by ECMWF. POP5 uses 3-day wind fields temporally interpolated from ECMWF monthly averages, while POP7 and POP11 use 3-day fields averaged from twice-daily ECMWF winds. POP11 additionally employs heat flux forcing from a method developed by Barnier et al. (1995), based on ECMWF climatological fields. (Maltrud et al., 1998)

A fourth run is initialized from POP11 output for the end of 1992 and run through 1997. Wind forcing is supplied by daily ECMWF wind stresses interpolated to every model time step (30 minutes), rather than by the monthly or 3-daily averages of the previous runs. Upper level velocities for the run under study are saved as daily snapshots.

2.   1/6-Degree Model Grid and Bathymetry

The 1/6-degree POP model is defined over a lattice of 20 concentric Mercator grids, one for each depth representation. On a given depth surface, there are 1280 longitudinally-spaced grid points for each of 896 represented latitudes. The longitude range is global; the latitudes are defined from 77°S to 77°N. The vertical spacing is 25 m for the first four levels, and varies between 35 m and 550 m for the remainder. The average horizontal resolution is ~1/5° (22.42 km at the surface) with lowest resolution of 0.28° (surface, ~31 km) at the equator to 0.06° (surface, ~6.5 km) at the poleward boundaries. Because the Rossby radius of deformation decreases poleward from the equator, a Mercator grid is

17

advantageous as its horizontal resolution also increases toward the poles. The POP grid allows resolution of the first baroclinic Rossby radius at all latitudes $|\lambda| < \sim 40°$; hence, the model should be expected to represent eddy formation processes at least up to the mid-latitudes. (Maltrud et al., 1998)

The bathymetry is interpolated to the 1/6° grid from the National Geophysical Data Center's high-resolution (1/12°) ETOPO5 database.

3. Forcing and Equilibration: 1/10-Degree Model

The ECMWF 1/10-degree model is initialized from June Levitus (1982) temperature and salinity climatology, and allowed to spin up from rest, beginning 1 June 1985, for a period of 5.3 years. Wind and salinity forcing are as per the 1/6-degree version; the Barnier et al. (1995) heat fluxes are also used, except that solar radiation is treated as an independent quantity and allowed to penetrate to depth. At the end of the spinup (1 October 1990), the wind stress is reset to 1 October 1995 and the integration continued until 1 July 1996. (Smith et al., 1999).

The NOGAPS 1/10-degree run is initialized using the restart file from the ECMWF run at the end of 1992. This version uses daily NOGAPS wind stresses temporally interpolated to every model time step (7 minutes) and spatially interpolated from a 1.25° grid to the model grid.

Output from the first two years of this 1993-1997 run forms the 1/10-degree database for this study.

4.   1/10-Degree Model Grid and Bathymetry

The horizontal sections of the 1/10-degree model lattice are mercator grids, with resolutions varying from 11.1 km at the equator to 3.2 km at the northern boundary. In contrast to the 1/6-degree model, the 1/10-degree model resolves the first baroclinic Rossby radii at all latitudes up to 60°N. There are 40 vertical levels, varying in thickness from 10 m at the surface to 250 m at depth (Smith et al., 1999). Again, ETOPO5 bathymetry is interpolated to the model grid.

5.   Output Fields and Binning

Zonal (u) and meridional (v) velocity fields from the midpoint of the 1/6-degree model's upper level (12.5 m) are saved as daily snapshots spanning the period January 1, 1993 to December 31, 1997. Likewise, daily second level (15.0 m) snapshots from the 1/10-degree model are saved for the period January 1, 1993 to December 31, 1994. These depths are picked to most closely match the depth of the drifters (15m). The final spatial domain of the analysis is chosen as 80°W - 20°E, 20°N - 70°N, an area defined by the bulk of the drifter data. Both drifter data and model output are binned onto 2°x2° and 5°x5° grids for the Eulerian and Lagrangian comparisons, respectively, with the exception that no

Lagrangian statistics are calculated for the 1/10-degree model.

6.   Results of Previous Comparative Studies

This section gives a brief description of the results of previous comparisons of the POP model with various data sources in our region of interest.

Maltrud et al. (1998) provide a comparative evaluation of POP5, POP7, and POP11, and remark that on the whole each faithfully reproduces the wind-driven circulation. They note, however, that problems remain in the model's resolution of the turbulent energy spectrum and its representation of meridional overturning. Though the stream functions from all three simulations closely resemble the profiles of the Sverdrup balance, where most of the departures can be explained by thermohaline, topographic, or inertial effects, Maltrud et al. (1998) point to a significant exception in the excessively poleward separation of the northern hemisphere western boundary currents. In particular, the Gulf Stream separation point at 37°N is displaced northward in the model by a large, persistent anticyclone, an artifact of the model. The authors note that this effect may be a native feature of Brian-Cox type models run at medium to high resolutions, though recent runs at both 1/6-degree using greater vertical resolution (Chao et al., 1996) and at 1/10-degree (Smith et al., 1999) show improved realism. The addition of ECMWF surface heat flux

forcing to the formulation for temperature restoration give POP-11 an improved mass transport in the lower Gulf Stream, though all three versions of the model suffer from an under-represented proportion of flow through the Florida Strait (Maltrud et al., 1998). This is apparently due to a loss, versus augmentation, of flow through the Windward Passage, caused possibly by exaggerated resistance through the Yucatan Channel (Maltrud et al., 1998). Both the Atlantic and global meridional heat transports, and the phase and amplitude of sea surface temperature and height, are improved by the use of heat flux forcing (Maltrud et al., 1998); difficulties remain, however, in representing western boundary undercurrent depth and water properties, partly due to biases in initial conditions. The runs using 3 day averaged wind fields (POP-7 and POP-11) produce great improvement in sea surface height (SSH) variability, though the observed values are still low compared to altimetry (Maltrud et al., 1998).

McClean et al. (1997) compare the mesoscale variability of the 1/6-degree model output (along with a 1/4-degree version called the Parallel Ocean Climate Model (POCM)) to TOPEX/POSEIDON (T/P) altimetry. Their objectives are to assess the impact of decreased friction and increased resolution between the 1/4-degree and 1/6-degree models, and to validate the models on the basis of SSH variability, EKE, and length scales.

21

The POP model is found to explain about 60% of the variability globally, and the POCM about 50%. Locally the POP outperforms the POCM and closely tracks with T/P in the vicinity of strong currents; otherwise both models generally underestimate variability by about 50%. The spatial distribution of the variability resembles that of T/P, except for an excessive eastward displacement of the Northwest Corner (Fu and Smith, 1996). In all versions of the model, EKE is found to be underestimated, due possibly to the quality of the wind forcing fields, the periodicity of the wind averaging, and inadequate modeling of the mixed layer. Length scales are more realistic in the POP than in the POCM, though both models correctly reproduce their spatial distributions, as observed by T/P altimetry.

To infer the relative effects of increased resolution over decreased friction between the two models, McClean et al. (1997) calculate a zonally-averaged meridional section of SSH in a latitudinal region where both models resolve the first baroclinic Rossby radius, and argue that the observed absence of a significant increase in SSH variability indicates the friction coefficient plays a subordinate role (refer to Figure 3). This result is supported by Treguier (1992), using a comparison of EKEs in a similar model, by varying only the mixing coefficients.

Tokmakian (1996) compares output from the POCM and POP to global tide gauge data, finding that the quality of the wind forcing fields is the primary factor affecting the
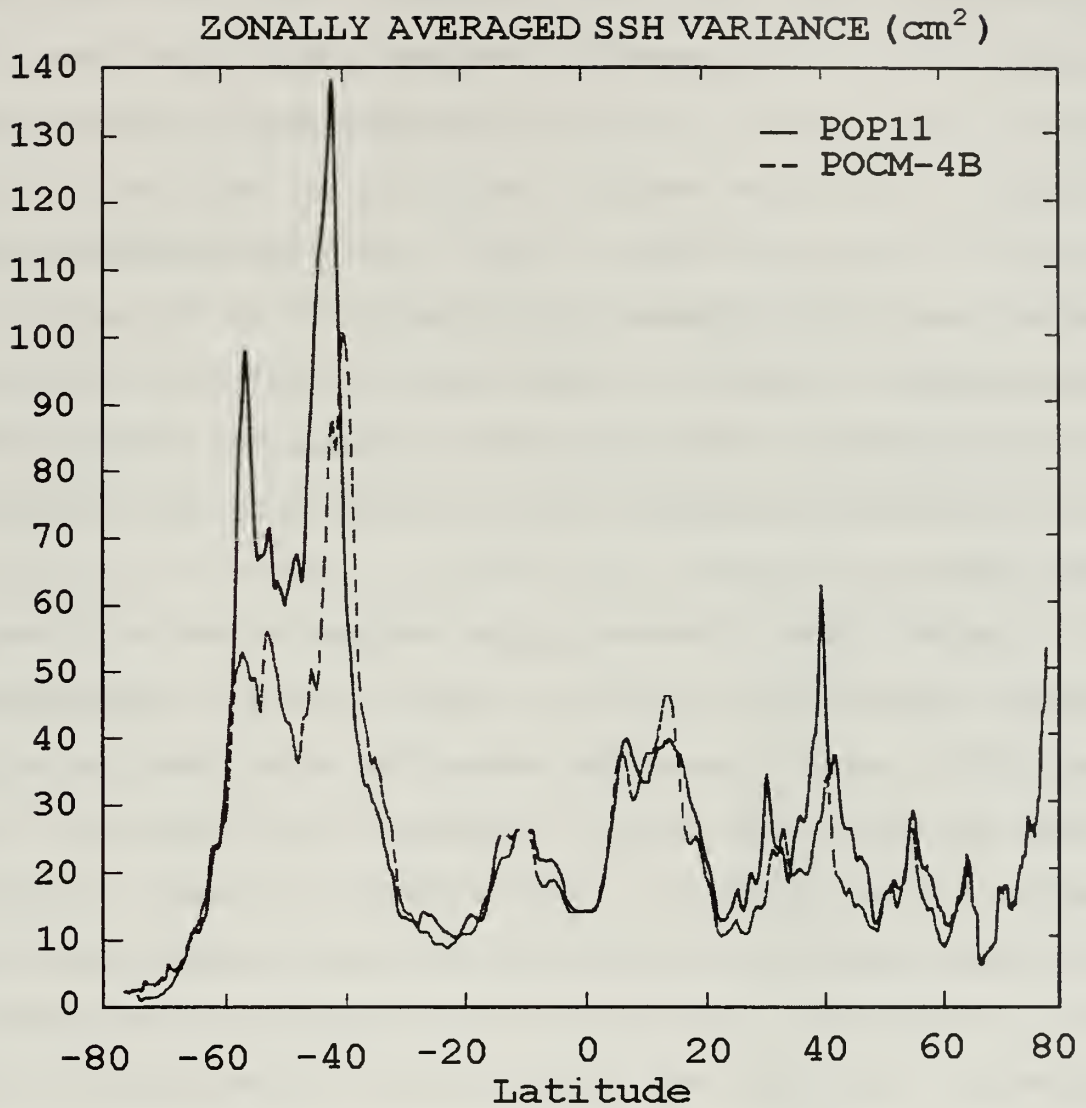
Figure 3. Meridional section of zonally-averaged sea surface height variance (cm^2) from POP-11 (solid line) and POCM-4B (dashed line) models. After McClean et al. (1997).

model's representation of SSH. Specifically, she notes no significant differences in the models' performance at latitudes below 35°N. Fu and Smith (1996) note that sea level variance is generally underestimated by a factor of about two, mainly in areas of high eddy activity, and suggest that better spatial resolution is required to fully resolve mesoscale eddies. They, too, find an improvement when heat flux forcing is substituted for temperature restoration. Finally, Fu and Smith (1996) note that the model represents fairly well the intraseasonal fluctuations at and above midlatitude and the interannual variability of the tropics.

Smith et al. (1999) compare results of the 1/10-degree model to various in situ sources (e.g., hydrography, drifters, current meters), satellite data, and to output from the POP-5/POP-7/POP-11 sequence. They note the 1/10-degree model produces a substantial improvement over the 1/6-degree model's representation of the time-averaged North Atlantic circulation, and find the former much more closely captures the shape and magnitude of the mesoscale energy spectrum. Smith et al. (1999) find the 1/10-degree model to distribute about 70% of the total basin kinetic energy as EKE, and note the spatial distribution of this EKE to be much more in line with observations than that of the 1/6-degree model.

Smith et al. (1999) note continuing difficulties in modeling the Gulf Stream and the North Atlantic Current at

1/10°, however. They find the separation point of the North Atlantic Current, in the region of the Northwest Corner, to lie too far to the northwest. The Gulf Stream also appears too far south, and its meander envelope too wide to the west of the New England Seamounts.

B.   DRIFTER DATA SET

In 1988 the World Climate Research Program organized the Global Drifter Program (GDP) to collect, interpret, and disseminate sea surface temperature and velocity data from globally deployed drifters. One of GDP's objectives was to design and build a relatively inexpensive, long-lived satellite-tracked drifter with specific water following and slip characteristics. Their drifter was developed at the Scripps Institution of Oceanography in La Jolla, California. It is hereafter referred to as the WOCE/TOGA Lagrangian drifter, as the specifications are those of the Surface Velocity Program sponsored by those international programs. Sybrandy and Niiler (1991) provide details of its construction and a parts list in the WOCE/TOGA Lagrangian Drifter Construction Manual. (Niiler, 1995).

In 1988 a coordinated effort to seed the tropical Pacific Ocean with GDP drifters was begun as the "Pan-Pacific Current Study". This project was followed in 1991 with Atlantic deployments, which provide the drifter database for this study.

1. The WOCE/TOGA Lagrangian Drifter

The GDP's Lagrangian drifter consists of a cylindrically-framed nylon "holey-sock" drogue tethered to a fiberglass surface float. The length of the tether is such that the center of the drogue travels in the mixed layer at 15 m. Figure 4 shows the dimensions of the entire drifter assembly. Within the surface buoy are housed submergence and sea surface temperature sensors, and a battery, transmitter and antenna for transmitting temperature readings to satellite-carried service Argos instruments. Due to the cost of satellite connectivity (Gianetti, 1993) the transmitters are programmed to be on for one day, then off for two days. The battery packs are designed for two years life under this duty cycle. The submergence sensor is installed as an aid to detecting drogue loss, as the floats frequently submerge when drogued (Niiler, 1995).

2. Data Collection and Conditioning

Drifter transmitter signals are received passively by ARGOS instruments aboard polar-orbiting National Oceanic and Atmospheric Administration (NOAA) satellites. There are at least two such satellites operating, in sun-synchronous orbits, at a given time. Their equatorial crossings occur in a fixed westward procession at 102-minute intervals. Mean pass duration is ten minutes, and the repetition period for a drifter's transmissions is 90 seconds. (Service Argos, 1984)
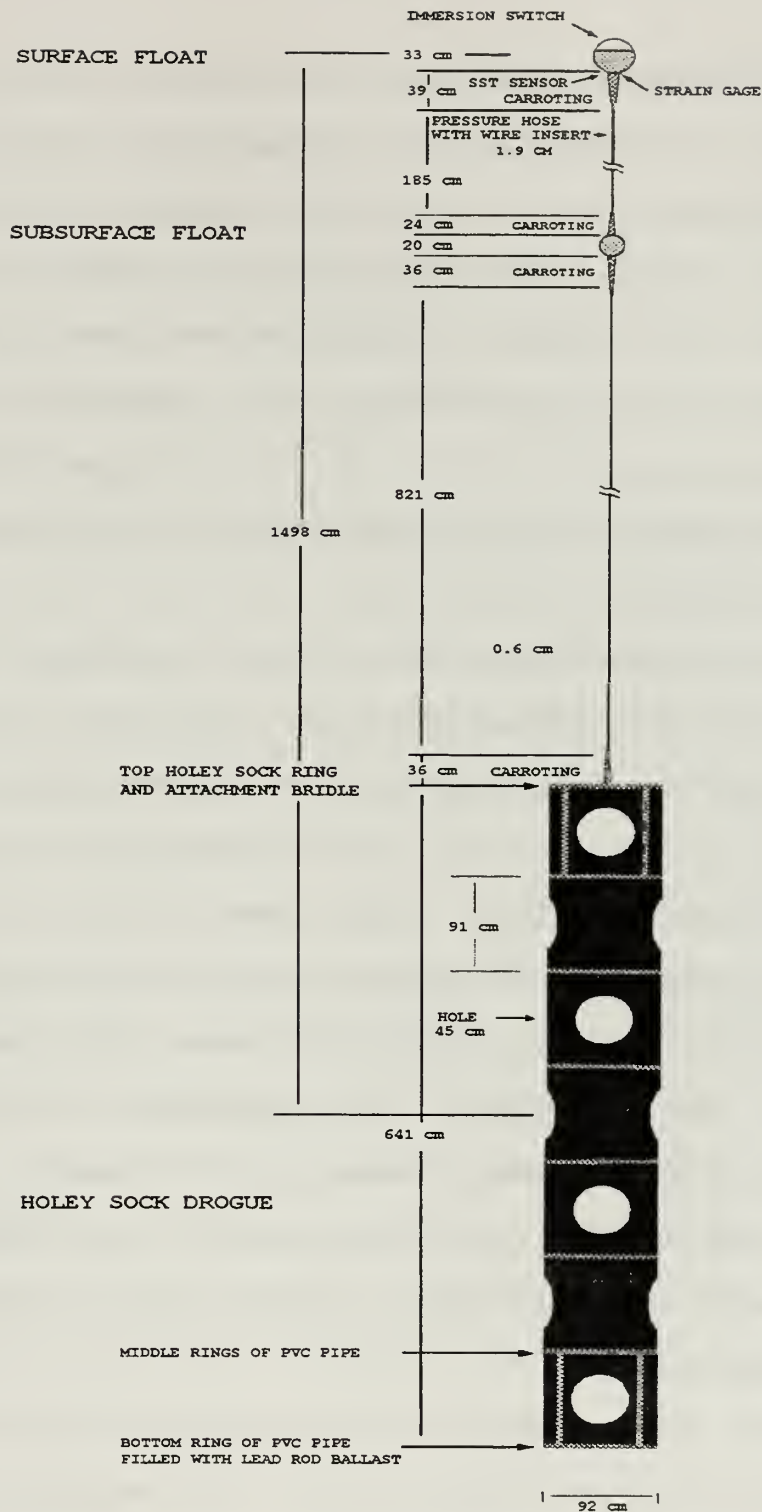
26

Figure 4. Diagram of the WOCE-TOGA Global Lagrangian Drifter, showing dimensions in cm. After Poulain et al. (1996).

Each transmission localizes the drifter, via doppler shift, to a cone formed with the satellite at the apex. The orbital elements of the satellite, based on its reception of reference signals from fixed ground transmitters, further restrict the possible locations to the branch of a hyperbola. The intersection of the hyperbolas formed from the satellite pass finally place the drifter at one of two possible locations. Argos then resolves the final ambiguity using geofeasibility criteria.

Position and temperature data are then forwarded to NOAA's Atlantic Oceanographic and Meteorological Laboratory (AOML). The data received from Argos are subject to errors from instrument instability, variations in number of transmissions received, and inaccuracies in measuring tracking geometry; the temporal spacing is uneven as well (Hansen and Poulain, 1996). To make the raw data more suitable for analysis, AOML applies an editing and interpolation technique developed by Hansen and Poulain (1996), and briefly outlined below, to remove any erroneous values and create uniform six-hour time series of velocity and temperature.

Bad position data are identified using a sequential point-rejection algorithm, where a new position is rejected if the velocity it implies compared to the previous position exceeds a certain threshold. The threshold is specified from known circulation characteristics of the region or from histograms of measured velocity. Temperature data are

considered bad if they exceed a running weighted mean, where the weights have been determined experimentally. For both positional and temperature data, the respective algorithms are applied in the forward and reverse directions. Only values that are offenders in both directions are rejected, so that good data are not unnecessarily lost. (Hansen and Poulain, 1996)

Once the position and temperature data are screened for errors, they are optimally interpolated to uniform 6-hour time series. Position data are treated as separate latitude and longitude time series; velocity values are then obtained by center-differencing the interpolated longitude and latitude values (Poulain, 1993).

The interpolation method is a unidimensional variant of kriging, a procedure used in mining and hydrology, where interpolated values are calculated as linear combinations of neighboring measurements. The weights are normally determined by minimizing the kriging variance, or mean squared difference between true and interpolated values. Because the interpolation variable in the present application is position, however, the kriging variance as defined is not guaranteed to have general existence. It is therefore specified in terms of an analytic structure function model whose parameters are determined empirically using actual drifter data. (Hansen and Poulain, 1996)

3. Drogue Slippage

A major concern in the design of the WOCE/TOGA Lagrangian drifter was that it have a predictable slip through the water (Sybrandy and Niiler, 1991), where slip is defined as the difference between drogue velocity and the current velocity averaged over the length of the drogue. Additionally, to avoid compounding error, it was desired to keep the slip within the limits of the average daily velocity uncertainty incurred from ARGOS tracking. This uncertainty was estimated at 1 cm/s, based on a conservative value of 1 km for positional error (Niiler et al., 1995).

Nonlinear motion effects were controlled by choosing a spherical float shape to minimize aliasing of wave-induced motion into the horizontal plane, a thin, stiff tether to reduce looping or kicking from waves, and a drogue shape that was resistant to kiting. To investigate the water-following characteristics of the resulting design, a series of field tests was performed under various water shear and wind conditions using a drifter outfitted with calibrated current meters, one at each end of the drogue. The average meter velocity was taken as the slip speed (Sybrandy and Niiler, 1991).

From these tests, wind is deduced to be the dominant force producing slip, and a statistical model is offered to correct for velocity measurements using the formula

$$U = 3.5\,(W/R) + 9.5\,(DU/R), \tag{1}$$

where U (cm/s) represents the slip velocity, W (m/sec) the wind velocity at 10 m, DU (cm/s) the velocity difference across the drogue, and where R is defined as the ratio of the product of the drogue area and its drag coefficient to the sum of the products of the tether and submerged floats and their drag coefficients. The equation associates a slip speed of 1 cm/s and a wind speed of 10 m/sec with an R value of 35; the WOCE/TOGA drifter has an R value of 40, so that the design criterion is met. (Niiler, 1995)

4.   Wind Correction

Niiler et al. (1995) provide a detailed description of the above experiment, but add that no buoy deployments were made in winds above 10 cm/s because the floats proved undeployable in the resulting sea conditions. Subsequent regression analysis of a much more complete worldwide database of drifters and global wind products has produced a simpler but improved formula for the WOCE/TOGA drifter (Stephen Pazan, personal communication):

$$U_{corr} = U_{uncorr} - 0.12\,W, \tag{2}$$

where U_{corr} is in cm/s, U_{uncorr} is in cm/s, and W is in m/s. We use the latter equation in this study to compute corrected

velocities for both Eulerian and Lagrangian analyses. The multiplier W is obtained for each observation by spatial bilinear interpolation of the corresponding daily NOGAPS wind components.

5. Temporal and Spatial Domains

Our drifter data set includes 624 of the GDP drifters deployed in the Atlantic. The total record length extends from January 1, 1993 to December 31, 1997. The drifter data are subsampled at daily intervals (every 4 data points) to match the daily sampling of model output. Figure 5 shows the temporal distribution of the subsampled drifter observations. The number of deployed drifters is between 50 and 100 for nearly every day in the time domain. Significant peaks occur in October, 1993 (127 drifters), and March of 1997 (126 drifters). Years 1994 and 1995 see nearly monotonic decreases and increases, respectively, with the lowest population in the time domain (46 drifters) occurring in January, 1995. Drifter population is near 100 for most of 1996.

The spatial domain is chosen to include the greater part of the drifter coverage. Though the Gulf of Mexico, western Caribbean, and latitudes as far south as 12°S are represented by the drifters in this 5 year period, the coverage is considered too sparse for meaningful comparisons. Additionally, we choose 70°N as an upper
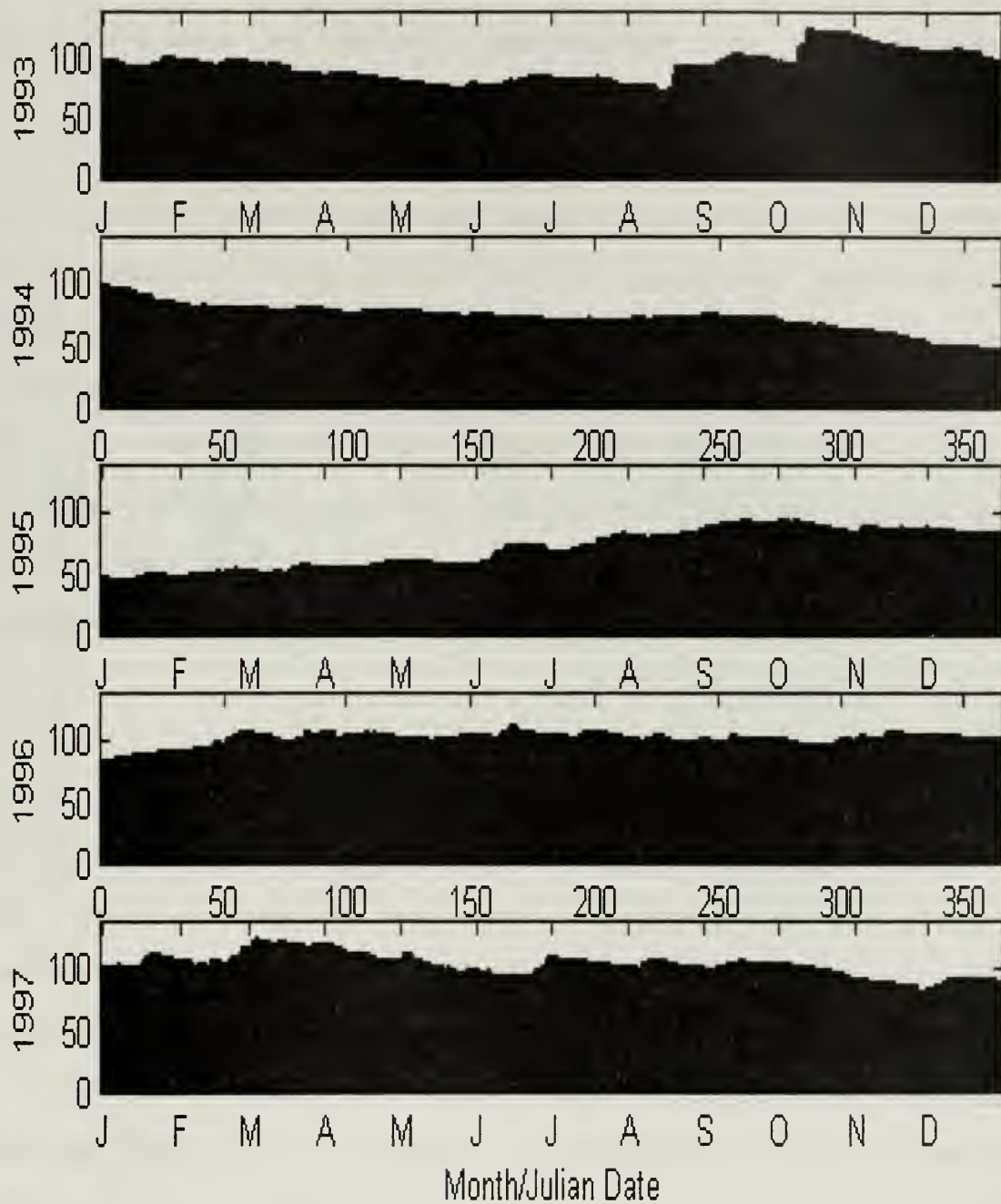
Figure 5. Temporal distribution of daily drifter observations, January 1, 1993 to December 31, 1997, over the geographical region 20°N - 70°N, 80°W - 20°E.

boundary to remain outside the restoring buffer zone. Our choice of an eastern limit is driven simply by the northern boundary and land constraints. We define our region of interest as 80°W to 20°E, 20°N to 70°N.

Figure 6 gives the deployment locations of the actual drifters, while Figure 7 shows the "deployment" locations of the simulated drifters for the "random start" scheme. There is no discernable pattern, naturally, for the "random starts". The actual drifter plot, however, is punctuated by concentrated releases off Cape Cod and the coasts of Iceland and Norway, between the Azores and Canary Islands, east of the Mid Atlantic Ridge between 44°N and 49°N, and in the Labrador Sea. In mid-ocean, the deployments are otherwise fairly uniformly scattered.

6.   Drifter Tracks and Simulated Trajectories

The "spaghetti" plot of actual drifter tracks, Figure 8, reflects the dispersion from the deployment sites, with high track densities corresponding to the areas of intense deployment. The coherent Gulf Stream and northern boundary currents are clearly seen, while the southeast basin is characterized by circuitous, rambling patterns. An eastward surface flow across the Iceland-Faroe Ridge is clearly shown by the concentrated deployments south of Iceland, whereas the path of the North Atlantic Current through the Rockall Channel into the Faroe-Shetland Channel is sparsely sampled.
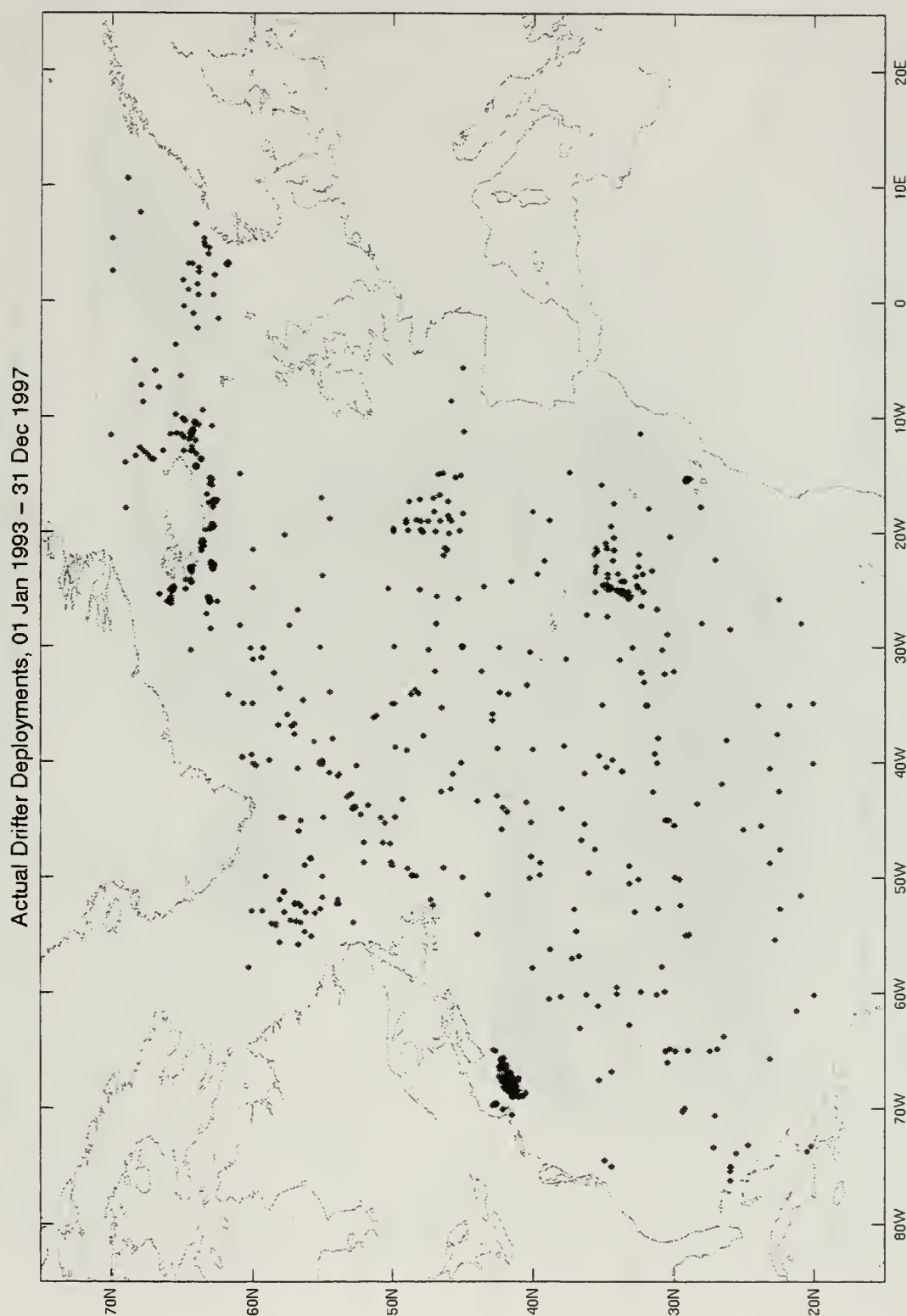
Figure 6. Deployment sites of actual drifters released in geographical region 20°N - 70°N, 80°W - 20°E, during time period January 1, 1993 to December 31, 1997.

35

Figure 7. Sites of 615 simulated drifter "deployments" from
the "same start" regime. Spatial and temporal boundaries are
those of the actual drifters, 20°N - 70°N, 80°W - 20°E,
January 1, 1993 to December 31, 1997.

36

Figure 8. "Spaghetti" diagram of actual drifter tracks, January 1, 1993 to December 31, 1997. Sampling frequency is daily.

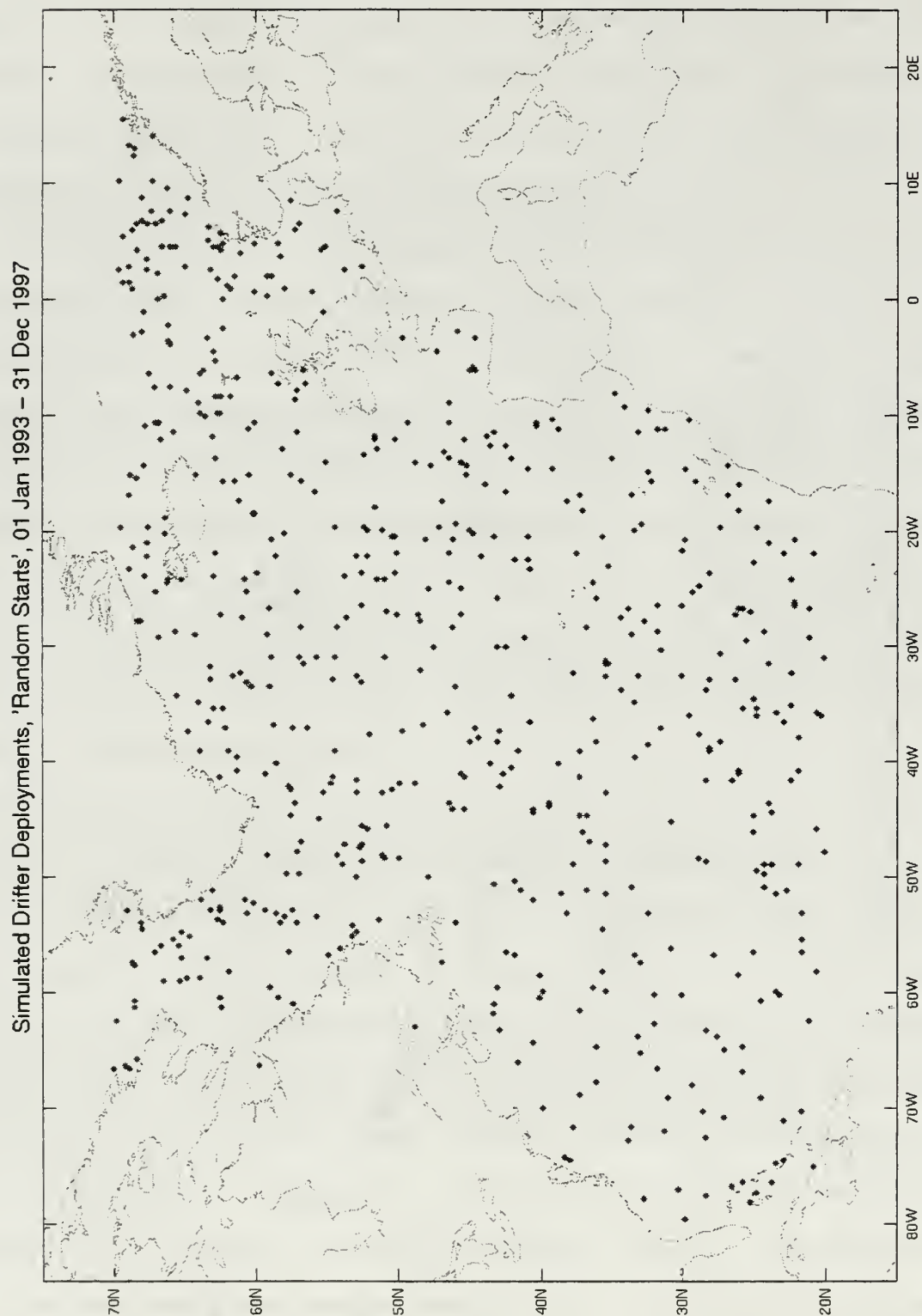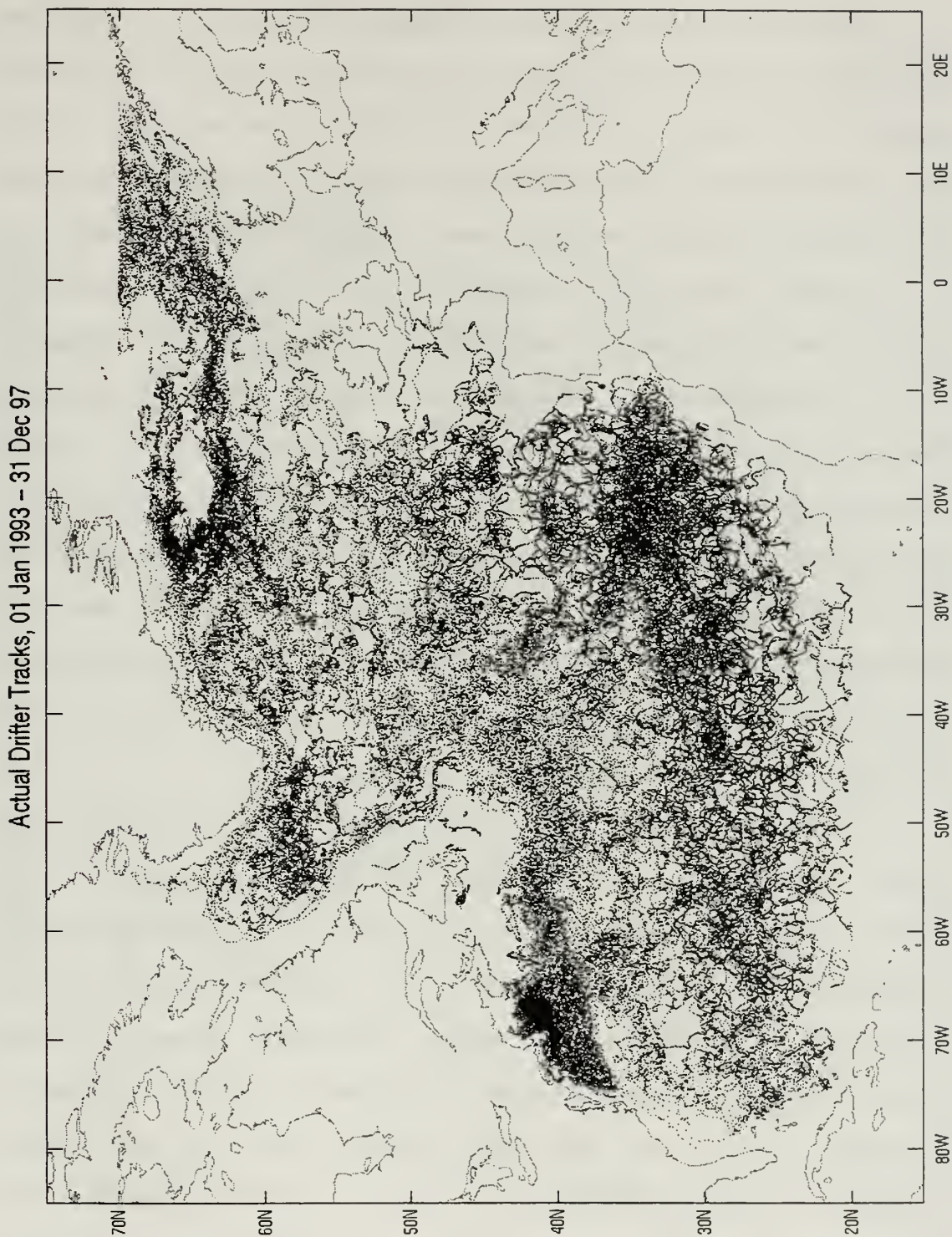Notable "holes" in the coverage occur over the eastern boundary of the Labrador Sea, the Iceland Plateau and region north of Iceland, the wide continental shelves off Canada and the southern North American coast, in the marginal seas off western Europe, and southwest of the Canary Islands.

Tracks from the "random start" regime (Figure 9) reflect more frequent inner shelf "deployments", especially in the Labrador Sea. There, the ring of coherent boundary flow is in stark contrast to the more static central Labrador Sea. The simulated drifters released west of Scotland correctly show the parallel northeast flows of the North Atlantic Current in the Rockall Channel and the drift currents north of the Rockall Plateau. The flow across the Iceland-Faroe Ridge agrees with that indicated by the drifters.

Coverage is lower in other areas, such as the Iceland shelf, which is nearly devoid of drifters except to the north, and the region west of the Strait of Gibraltar. Significantly, the absence of "random start" tracks outlining the Reykjanes Ridge reflects Krauss' (1995) bifurcation of the Irminger Current. Other lapses in coverage occur in the same places as for the actual drifters. The northwest Nordic Seas, southern Newfoundland Grand Banks, and the eastern reaches of the Labrador Sea are sparsely covered. Except for the North Sea, the European marginal seas are infrequently sampled by the "random start" trajectories.
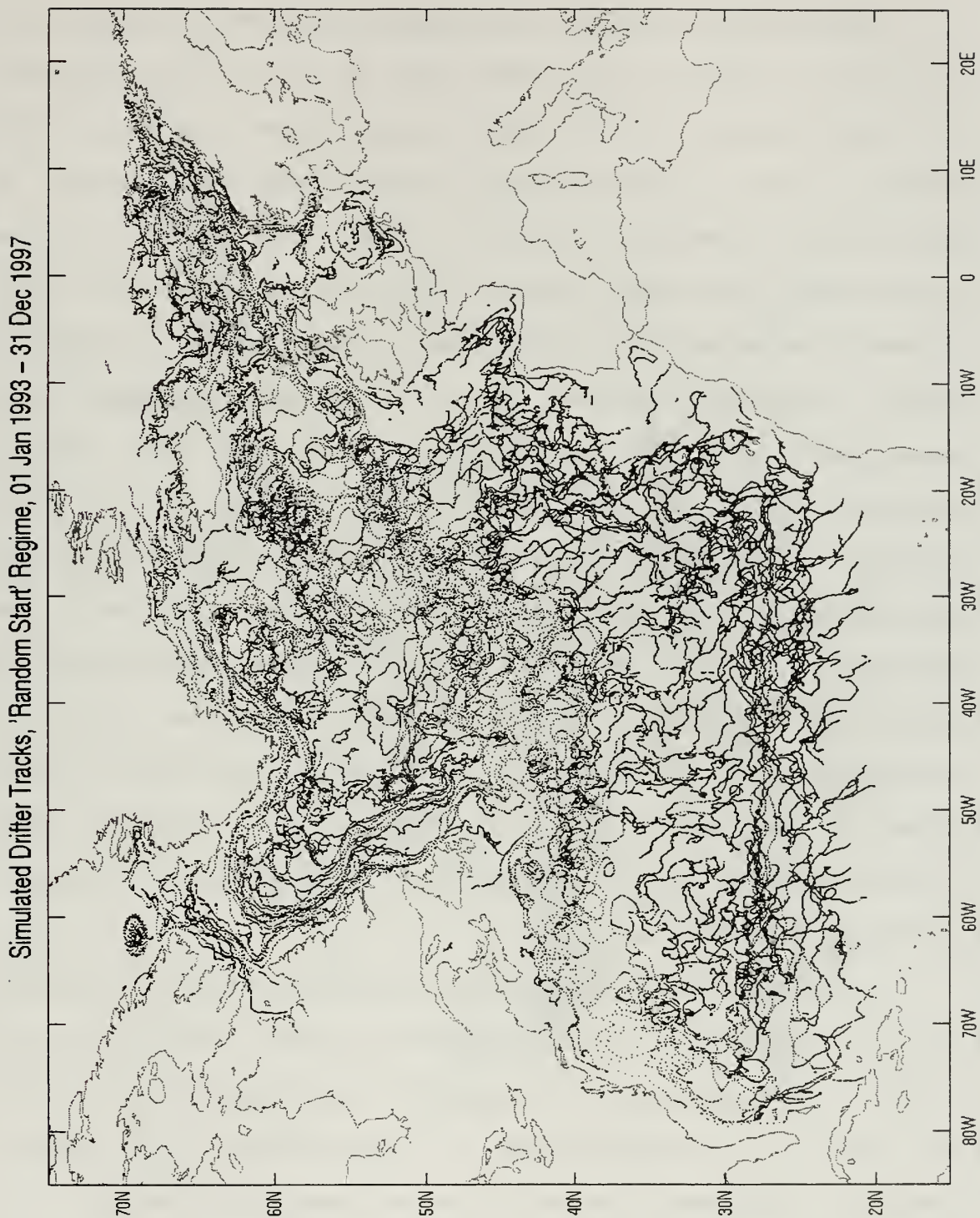
Figure 9. "Spaghetti" diagram of numerical drifter tracks from the "random start" simulation. January 1, 1993 to December 31, 1997. Sampling frequency is daily.

Track density in the Subtropical Gyre from roughly 30°N to 40°N is lower for the model than for the actual drifters. The more direct "random start" trajectories are due to the model's overly uniform gyre recirculation patterns, as described in section IV.B.2. A comparison of the drifter tracks with the "same starts" trajectories (Figure 10) more clearly reflects the differences in flow dynamics. South of 45°N the model has two very strong zonal signals, one associated with the Gulf Stream, and the other with a spurious front to be described in section IV.B.2. In contrast, the actual drifter tracks have a more homogeneous distribution. Another notable difference concerns the northward turn of the Gulf Stream along the Newfoundland Grand Banks. Whereas the data show the flow continuing northward into the Northwest Corner, the "same start" tracks show a premature eastward banking at roughly 45°N, consistent with the previously observed eastward displacement of this feature.

Figure 11 shows the spatial distribution of the drifter data in number of daily observations per 2°x2° bin. The peaks in the regions of concentrated deployments noted above are obvious. The entrainment of the drifters into the Gulf Stream, Irminger Current, East Iceland Current, and Norwegian Atlantic Current is evident, as is the broad westward diffusion of drifters released in the southeast Subtropical Gyre. The stasis in the central Labrador Sea is apparent as well.
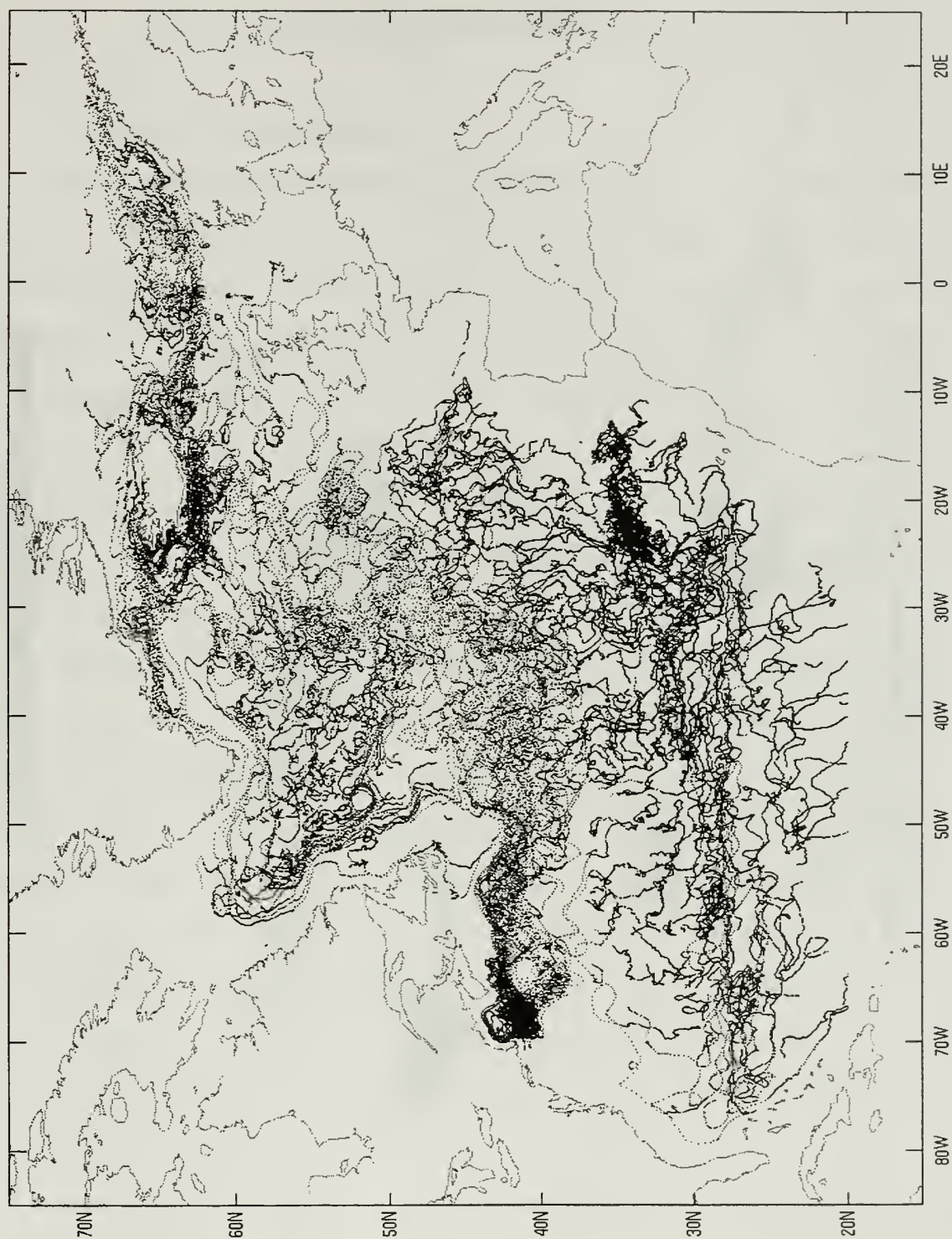
Figure 10. "Spaghetti" diagram of numerical drifter tracks from the "same start" simulation. January 1, 1993 to December 31, 1997. Sampling frequency is daily.
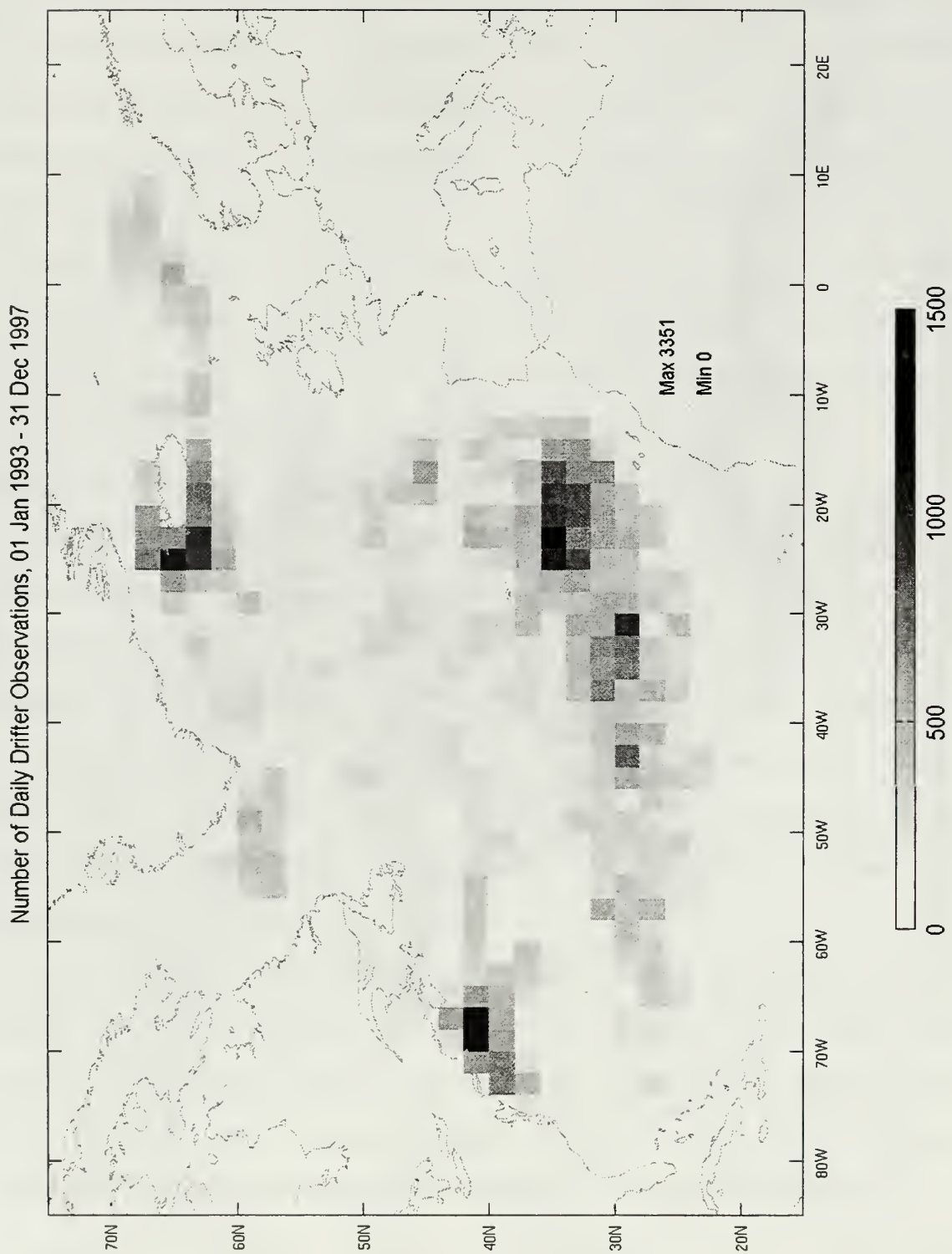
41

Figure 11. Number of daily observations of actual drifters
per 2°x2° bin, January 1, 1993 to December 31, 1997.

IV. EULERIAN ANALYSIS

A. FORMULAE AND METHODS

For the Eulerian analyses we partition our geographical domain (section III.B.5) into 50 zonal bins and 25 meridional bins. For each bin we extract velocities from the midnight drifter observations taken within its boundaries, and the model velocities at the corresponding time-location coordinates. We then compute the Eulerian statistics described below for both sets of velocity values. All observations from the actual drifters are corrected for drogue slippage as described in section III.B.4.

Separate comparisons are made for the 1/6-degree model run and the 1/10-degree run. Because five years of output were available from the former, whereas only two years of output were available from latter, we use two separate drifter data sets for consistency in the comparisons. The drifter data for the 1/6-degree comparison is the full data set spanning the period January 1, 1993 to December 31, 1997, while that for the 1/10-degree comparison is an abbreviated set running from January 1, 1993 to December 31, 1994.

For the 1/6-degree model comparisons, the data and model velocities are extracted over the time domain January 1, 1993 to December 31, 1997. For the 1/10-degree model comparisons the velocities are collected for the period January 1, 1993 to December 31, 1997.

If zonal velocity (cm/s) is denoted u, and meridional velocity (cm/s) as v, then we may define mean kinetic energy (MKE, cm^2/s^2), by

$$MKE \equiv \frac{1}{2}\left(\langle u \rangle_E^2 + \langle v \rangle_E^2\right) \tag{3}$$

where the operator $<>_E$ denotes a simple average taken over all the data falling into a given bin, and where the prime indicates the residual about the Eulerian mean. Eddy kinetic energy (EKE, cm^2/s^2) is defined by

$$EKE \equiv \frac{1}{2}\left(\lambda_1 + \lambda_2\right) \tag{4}$$

where λ_1 and λ_2 ($\lambda_1 \geq \lambda_2$) are the principal components of variance, computed (Freeland et al., 1975) as the roots of

$$\left(\langle u'^2 \rangle_E - \lambda\right)\left(\langle v'^2 \rangle_E - \lambda\right) - \langle u'v' \rangle_E^2 = 0. \tag{5}$$

The roots λ_1 and λ_2 are therefore the eigenvalues of the Eulerian sample covariance matrix. The two eigenvalues and their corresponding eigenvectors define an ellipse describing the distribution of velocity variance for the given bin; equivalently, a standard deviation ellipse is

defined. The rotation angle θ for the ellipse is calculated
(Freeland et al., 1975) via

$$\left(\frac{1}{2}\right)\tan(2\theta)=\frac{\langle u'v'\rangle_E}{\langle v'^2\rangle_E-\langle u'^2\rangle_E}. \tag{6}$$

The choice of bin size is made to ensure adequate
feature resolution and number of observations per bin. It
should be noted that the chosen resolution has an effect on
the measured proportion of EKE and MKE. Figure 12, a plot
of EKE and MKE vs. resolution, illustrates this effect. The
points on the curves are generated by averaging the drifter
EKE and MKE values for all bins, for each given bin size.
Binning schemes are optimal with respect to robustness at
resolutions where the two curves run nearly horizontally;
results are then equally valid for any resolution in their
plateaus. This is unfortunately not the case for high
resolutions, due to the increasingly steep ramping of MKE as
bin size decreases below about six degrees. Our chosen bin
size (2°x2°) lies between these two extremes, enabling good
feature resolution while avoiding the region where
sensitivity increases quite sharply.

Plots of mean vectors, principal standard deviation
ellipses, and eddy and mean kinetic energies for both model
and drifter data are provided in the subsequent section.
Additionally, we test for significant departures of the

45

model from the "true" mean drifter velocities. This is done, bin by bin, using both a "graphical" method, and Hotelling's T^2 statistic for bivariate normal populations.
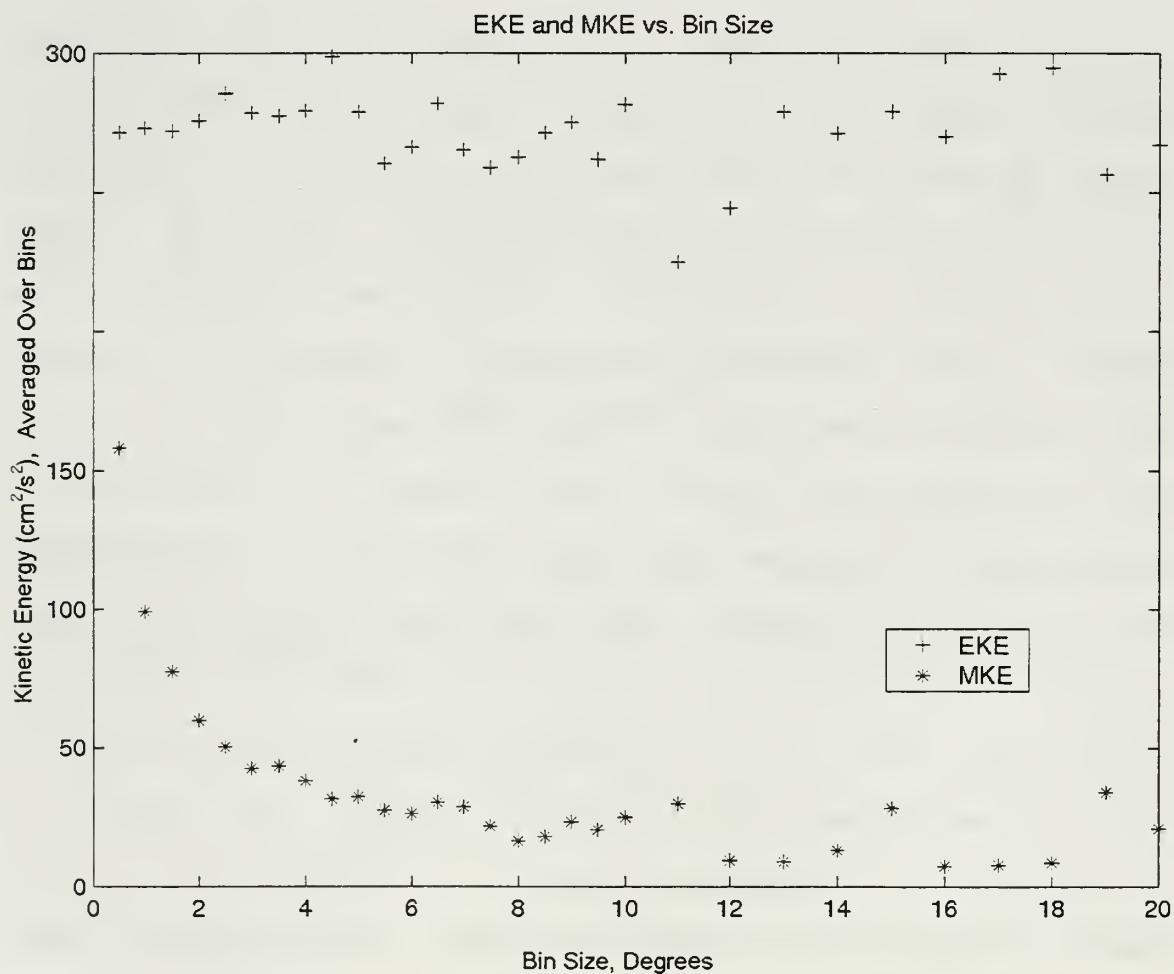

Figure 12. Variation of eddy kinetic energy (EKE) (cm^2/s^2) and mean kinetic energy (MKE)(cm^2/s^2) with bin size (degrees). The points on the curves are obtained by binning the actual daily drifter data into bins of the given size. The present study uses 2°x2° bins for the Eulerian analysis.

For both methods we extract subsets of the model and data velocities that are considered temporally and spatially independent. These we denote by

$$\mathbf{V}_m \equiv [\mathbf{v}_{m_1}, \mathbf{v}_{m_2}, ..., \mathbf{v}_{m_{n_m}}] \ , \ \text{and} \ \mathbf{V}_d \equiv [\mathbf{v}_{d_1}, \mathbf{v}_{d_2}, ..., \mathbf{v}_{d_{n_d}}],$$

where the subscripts m and d refer to the model and data, respectively, n_m and n_d are the number of independent observations from the model and data, respectively, and where the boldface indicates the vector quantity of both zonal and meridional components. To obtain the above subsets, we first subsample the daily velocity records at a time interval greater than a representative average Lagrangian integral time scale for the North Atlantic Ocean, taken as two days (see section V.B.1). For the observations corresponding to each independent time step, a heuristic network algorithm is applied to select a spatially independent sample. The algorithm first identifies all observations that are within a representative mesoscale eddy radius for the North Atlantic. This is taken to be 100 km, based on a midlatitude average of the first internal Rossby radius of deformation. It then randomly chooses a point to reject, reevaluates the remaining network for distances between points, and repeats until no point is within the threshold distance of any of its neighbors. The resulting points form a candidate set; if the algorithm is applied

47

multiple times, the largest set among the candidates is taken as the sample for that time step. The union of all such sets over all time steps then forms a temporally and spatially independent sample for that bin. We apply the network algorithm 10 times for each independent time step, over each bin.

In the graphical test for equality of means, we first form 95% standard error ellipses for the model and data by scaling the principal component eigenvalues of $\mathbf{V}_m$ and $\mathbf{V}_d$, respectively, by

$$t_{1-\frac{\alpha}{2},n_m-1}\sqrt{\frac{1}{n_m}} \quad \text{and} \quad t_{1-\frac{\alpha}{2},n_d-1}\sqrt{\frac{1}{n_d}},$$

where $t_{\alpha,n}$ is the 1-α quantile of Student's t distribution with n degrees of freedom. For each bin we connect the tails of the model velocity vector and the drifter velocity vector. The standard error ellipses are then placed with their centers at the tips of their respective vectors. If the ellipses fail to intersect, the velocities are assumed to be significantly different for that bin.

Hotelling's T^2 test (Seber, 1984) involves calculating, for $\mathbf{V}_m$ and $\mathbf{V}_d$, the test statistic

48

$$T_0^2 = \frac{n_n n_d}{n_m + n_d}(\overline{\mathbf{v}}_m - \overline{\mathbf{v}}_d)'\mathbf{S}_p^{-1}(\overline{\mathbf{v}}_m - \overline{\mathbf{v}}_d), \qquad where$$

$$\overline{\mathbf{v}}_m \equiv \frac{1}{n_m}\sum_{i=1}^{n_m}\mathbf{v}_{m_i}, \quad \overline{\mathbf{v}}_d \equiv \frac{1}{n_d}\sum_{j=1}^{n_d}\mathbf{v}_{d_j},$$

$$\mathbf{S}_p \equiv \frac{1}{(n_m + n_d - 2)}\big[(n_m - 1)\mathbf{S}_m + (n_d - 1)\mathbf{S}_d\big],$$

and where $\mathbf{S}_m$ and $\mathbf{S}_d$ are the model and data covariance matrices, respectively, for the bin. The null hypothesis that the model velocity does not depart significantly from the drifter velocity is rejected at level α (.05 for 95% confidence) if

$$T_0^2 \geq \frac{2(n_m + n_d - 2)}{n_m + n_d - 3}F_{2, n_m + n_d - 3}^{\alpha} = T_{2, n_m + n_d - 2, \alpha}^2.$$

The test is fairly insensitive to departures from normality and unequal covariance matrices when the two sample sizes are equal (Seber, 1984). We do not meet this condition in general, due to edge effects in binning model velocities (the data domain is continuous, while the model domain is discrete), but the sizes are close enough that the test should work reasonably well.

Finally, we look for the dependence of the model's performance on energy level (both EKE and MKE) by plotting the ratios of model kinetic energy to drifter kinetic energy against drifter kinetic energy (see following section).

49

Plots for the Eulerian results are provided in the following section; plot output is presented only for bins with at least 40 observations for the 1/6-degree comparisons, and 10 observations for the 1/10-degree comparisons.

B.   EULERIAN RESULTS: 1/6-DEGREE MODEL

1.   Mean Flow and Eddy Kinetic Energy Indicated by the Drifters

Figure 13 shows the mean circulation derived from the drifter data, over the 2°x2° grid, for 1993 - 1997. The major circulation patterns discussed in chapter I are evident. The Gulf Stream, East and West Greenland Currents, Labrador Current, Irminger Current, East Iceland Current, and Norwegian Atlantic Current are particularly well-defined, as is the North Atlantic Current west of 25°W. The Northwest Corner is quite prominent. The eastern limb of the Subtropical Gyre is also evident, the Canary Current and North Equatorial Current clearly visible, though not nearly as strong as the above currents. A division of circulation in the southern Nordic Seas into two sub-gyres is also evident, with an apparent boundary along the prime meridian.

Maximum drifter speed seen in the Gulf Stream (226 cm/s) agrees well with the 200 cm/s measured by Johns et al (1995). The drifters reach 85 cm/s in the Norwegian Atlantic Current (119 cm/s in the 6-hourly observations), roughly in agreement with the 110 cm/s noted by Poulain et al. (1996).

Mean Velocity Vectors, Drifter Data
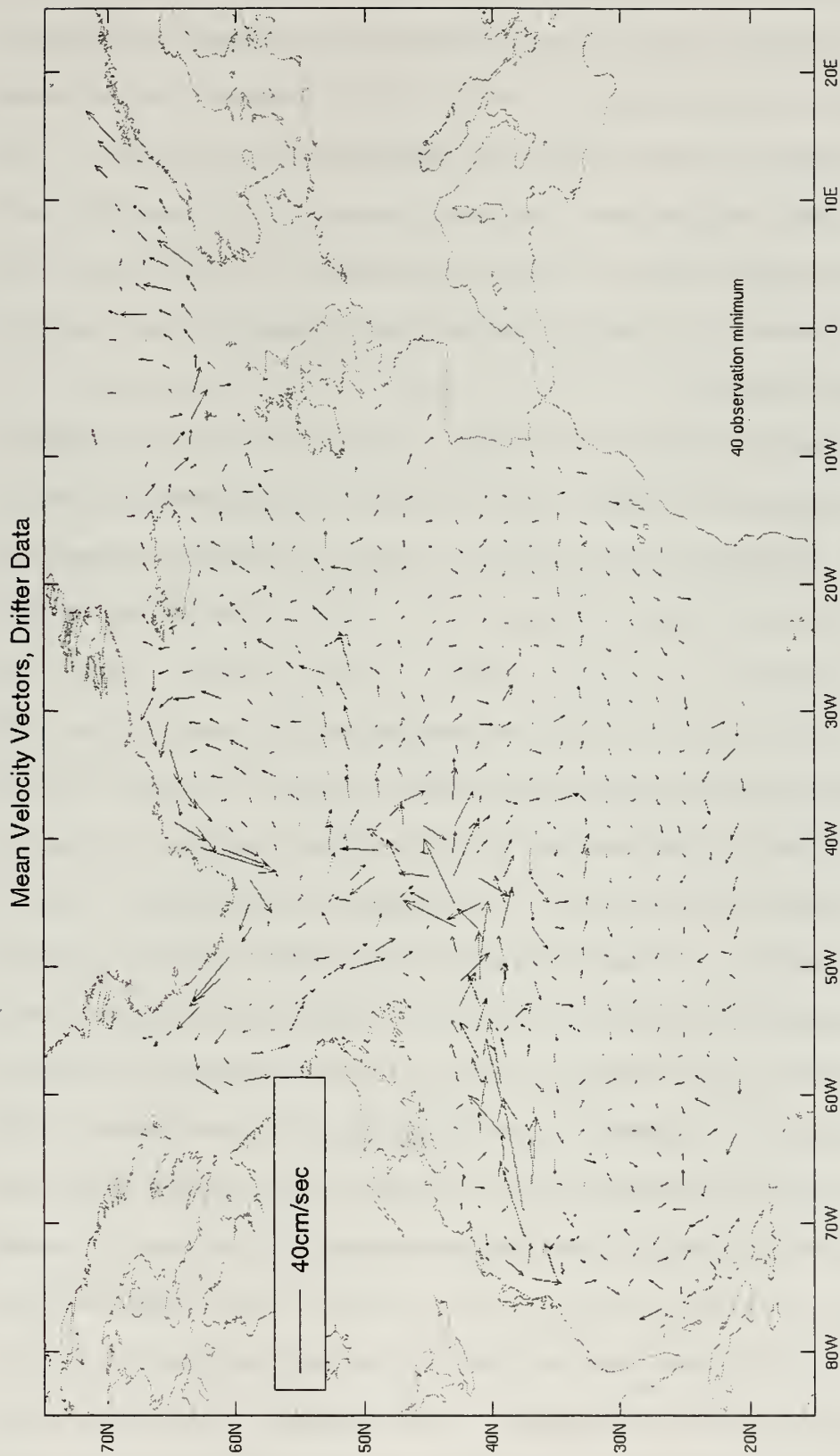
40 observation minimum

40cm/sec

Figure 13. Mean velocity vectors (cm/s) for the actual drifter data over the 5-year time domain, January 1, 1993 to December 31, 1997. Tails of vectors are anchored at the centroids of the observation points. Vectors for bins with fewer than 40 daily observations not shown.

51

Peak speeds observed in the East and West Greenland Currents (123 cm/s, 142 cm/s) are notably higher than the 70 cm/s reported by Krauss (1995), due perhaps to a more extensive data set and sampling closer to the cores of the currents. Mean values for the region south of Iceland and west of Scotland, most of which are from 0.5 to 5 cm/s, are on the same order as the 0.7 cm/s to 4.7 cm/s cited by Otto and Van Aken (1996).

A plot of EKE for the drifter data (not shown) reveals the three tongues of high EKE noted by Richardson (1983); these are evident as well in the principal standard deviation ellipse plots (Figure 18). Eddy kinetic energy in the Gulf Stream at 37°N, 67°W is 2140 cm^2/s^2 from the drifters, two-thirds of the value calculated by Richardson (1983). Our maximum observed EKE of 2957 cm^2/s^2, nearly identical with Richardson's, occurred further to the east, in the bin defined by 38°N-40°N, 62°W-64°W. Values downstream south of Newfoundland agree with the 1500 cm^2/s^2 found by Krauss and Käse (1984); our drifters indicate over twice the 600 cm^2/s^2 they cite for the Northwest Corner, however. East of the Mid Atlantic Ridge our estimates (300 cm^2/s^2) are again in agreement. It should be noted that the most of the drifters of Krauss and Käse (1984) were drogued significantly deeper (100 m) than ours, which may explain the large difference in Northwest Corner estimates. Along the Subarctic Front southwest of Iceland, EKE from the drifters is in agreement with the 100 cm^2/s^2 to 200 cm^2/s^2

found by Otto and Van Aken (1996). We find the same low values of EKE (< 100 cm^2/s^2) noted by Richardson (1983) and Krauss and Käse (1984) in the eastern basin, only bisected by the third of Richardson's "tongues" extending eastward to the African shelf. Our values of EKE in the North Equatorial Current match Richardson's 100 cm^2/s^2 only over the east basin; to the west they are about twice this value. Finally, for the Nordic Seas region south of 70°N, we observe the same low (< 100 cm^2/s^2) energies over the southern Iceland Plateau and higher values (200 – 400 cm^2/s^2) along the course of the Norwegian Atlantic Current, in agreement with Poulain et al. (1996).

2.   Mean Flow Comparison

Figure 14 shows the mean circulation from the masked output. There are both pronounced similarities and differences when compared to Figure 13. The unrealistic large anticyclone noted by Maltrud et al. (1998), where the Gulf Stream separates from the continental shelf at 37°N, is present in the output. The eastward displacement of the Northwest Corner to mid-basin, noted by Fu and Smith (1996), appears in Figure 14, though the northward turn of the Gulf Stream around the Newfoundland Grand Banks is also indicated.

The model reproduces the northeastern drift through the gap between Iceland and Scotland. Though it slightly exaggerates its magnitude, it captures the lack of
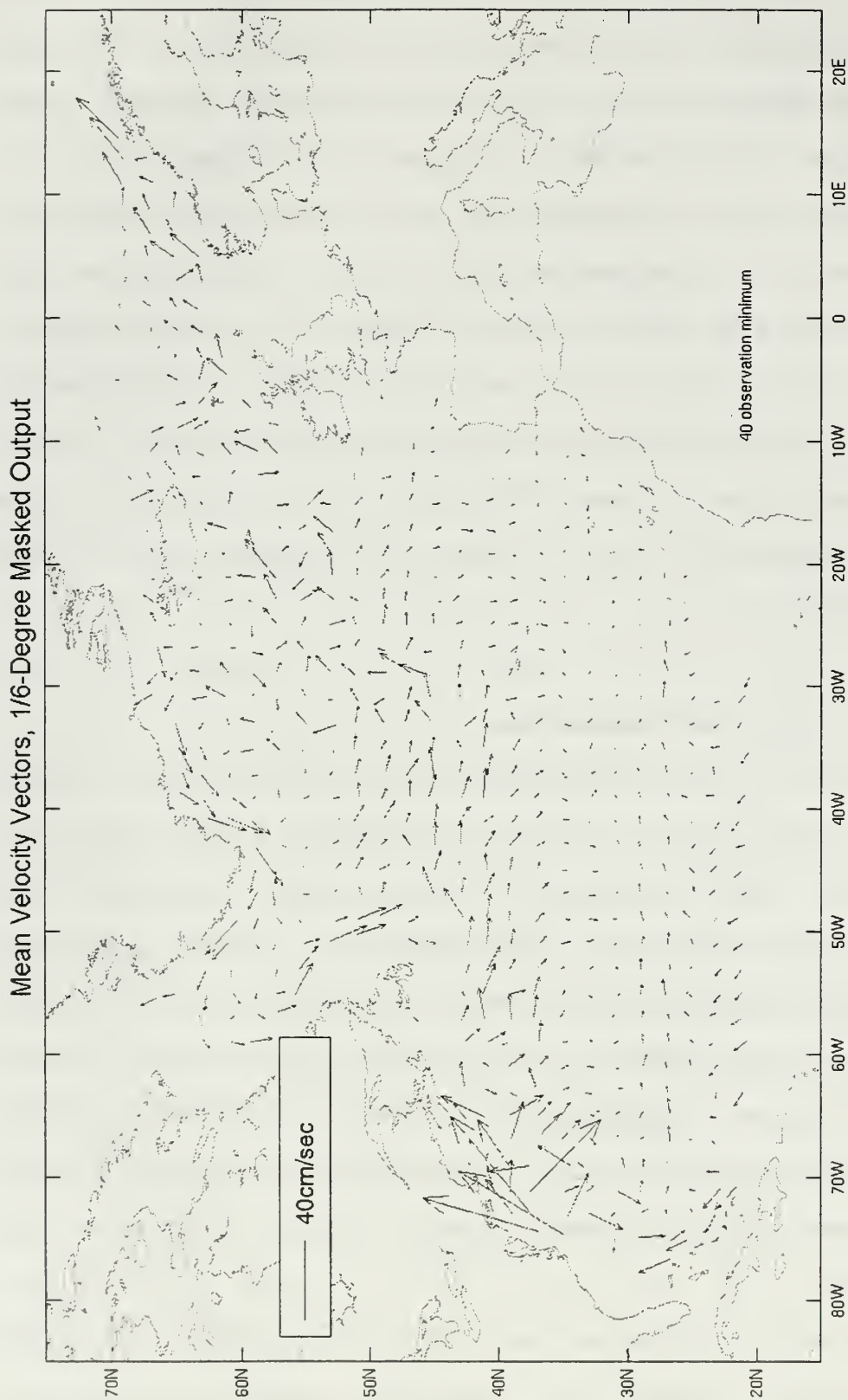
Figure 14. Mean velocity vectors (cm/s) for the masked 1/6-degree model output over the 5-year time domain, January 1, 1993 to December 31, 1997. Tails of vectors are anchored at the centroids of the observation points. Vectors for bins with fewer than 40 observations not shown.

uniformity in this flow. Equally chaotic is the flow on the westward side of the model's Northwest Corner; here the feature interferes with the eastern boundary of the Irminger Current. The northeast quarter of the Subtropical Gyre is well represented by the model, but there is very little evidence of the Canary Current to the south. The Azores Front is absent as well in the model mean vector plot, but is evident between 32°N and 34°N in the drifter plot.

The model shows more gyre recirculation from the North Equatorial Current than do the drifters. This may be a sampling effect, however, due to relatively low drifter concentration south of 24°N. In the model, recirculations from both the North Equatorial Current and the Gulf Stream veer eastward to form a basin-wide flow between 26°N and 30°N. Smith et al. (1999) note the presence of this effect in the 1/6° simulations of Maltrud et al (1998). According to Milliff et al. (1996), this flow is the effect of a front in the model's Sverdrup stream function created by strong wind stress curls off the coast of Africa around 30°N. Neither this feature nor the strong parallel patterns of the model's recirculation is revealed by the drifters.

In a general sense, there is more uniform structure to the current patterns in the model than is evidenced by the drifters. The complexity of flow in the Gulf Stream is particularly under-represented; the model shows a wide, excessively uniform eastward flow between 40°N and 52°N, extending to the Mid-Atlantic Ridge. Over this course the

boundary between the Gulf Stream and the North Atlantic Current is ill-defined in the model, whereas the drifter data show the eastward mean flow of the Gulf Stream dissipating west of approximately 38°W.

Mean flow patterns and magnitudes are well reproduced above 60°N. There is a large degree of similarity between model output and drifter data along the Norwegian Atlantic, East Iceland, and East and West Greenland Currents. The Labrador Current is also accurately represented down to 45°N. The model also captures the separation of Nordic Seas circulation into sub-gyres gyres along the ridge between the Norwegian and Lofoten Basins.

3.   Mean Kinetic Energy Comparison

A comparison of model and drifter MKEs via Figures 15 and 16 shows differences in energy distribution along the course of the Gulf Stream and effects connected with the model's artifacts. There is excessive energy in the Antilles Current, and along the mid-Atlantic shelf between 34°N and 40°N, corresponding to the model's spurious anticyclone. Along the mid-course of the Gulf Stream, from its seaward turning at Cape Hatteras to the Northwest Corner, MKEs are underestimated. The model's displacement of the Northwest Corner creates artificially low MKEs in the feature's actual location. In contrast, the model's delayed northward turn of the Gulf Stream and its shifted Northwest corner cause MKE
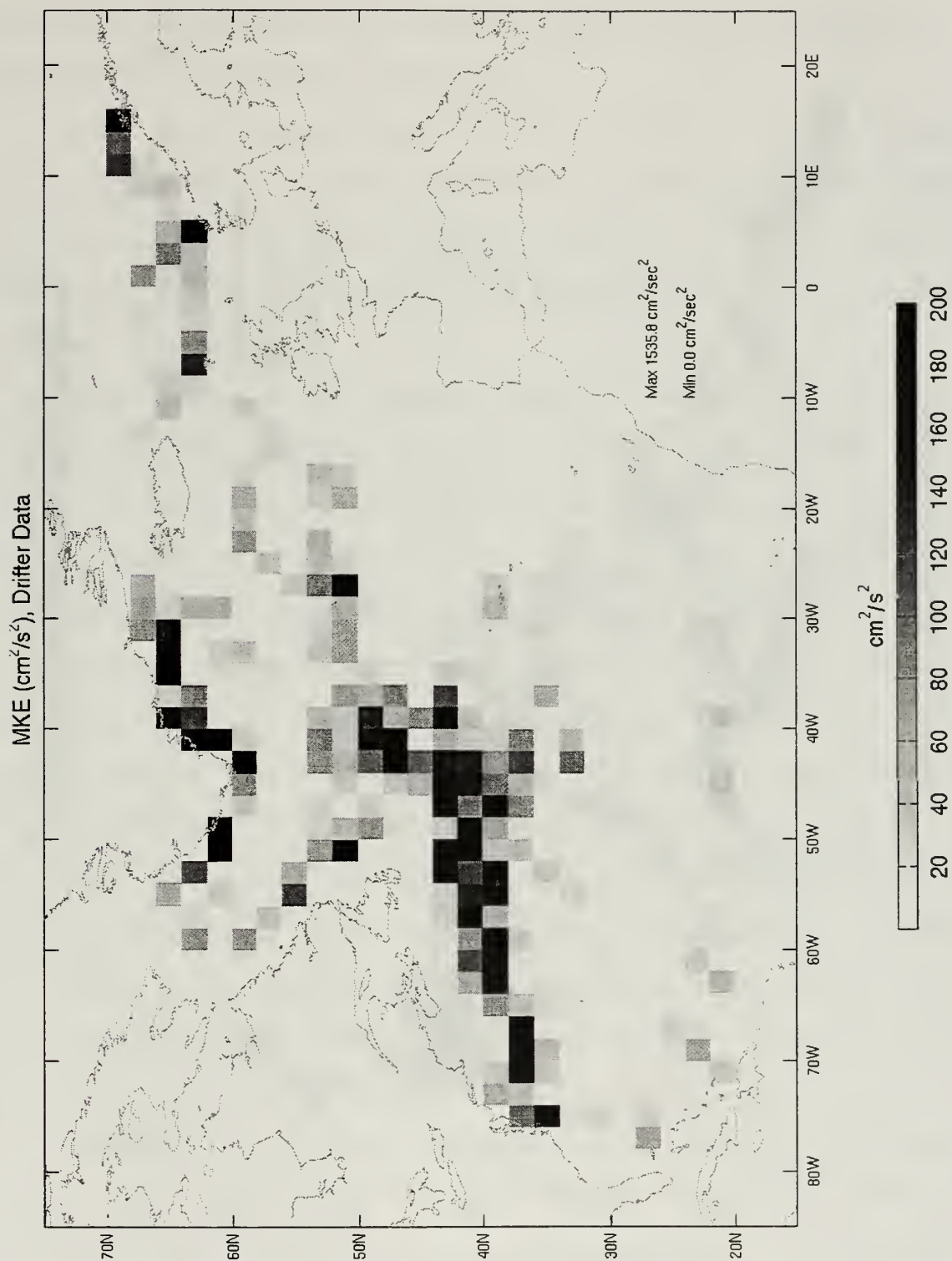
Figure 15. Mean kinetic energy (MKE)(cm^2/s^2) for the actual drifter data over the 5-year time domain, January 1, 1993 to December 31, 1997. Bins with fewer than 40 daily observations contain no information and are in white.

57

Figure 16. Mean kinetic energy (MKE)(cm^2/s^2) for the masked
1/6-degree model output over the 5-year time domain, January
1, 1993 to December 31, 1997. Bins with fewer than 40 daily
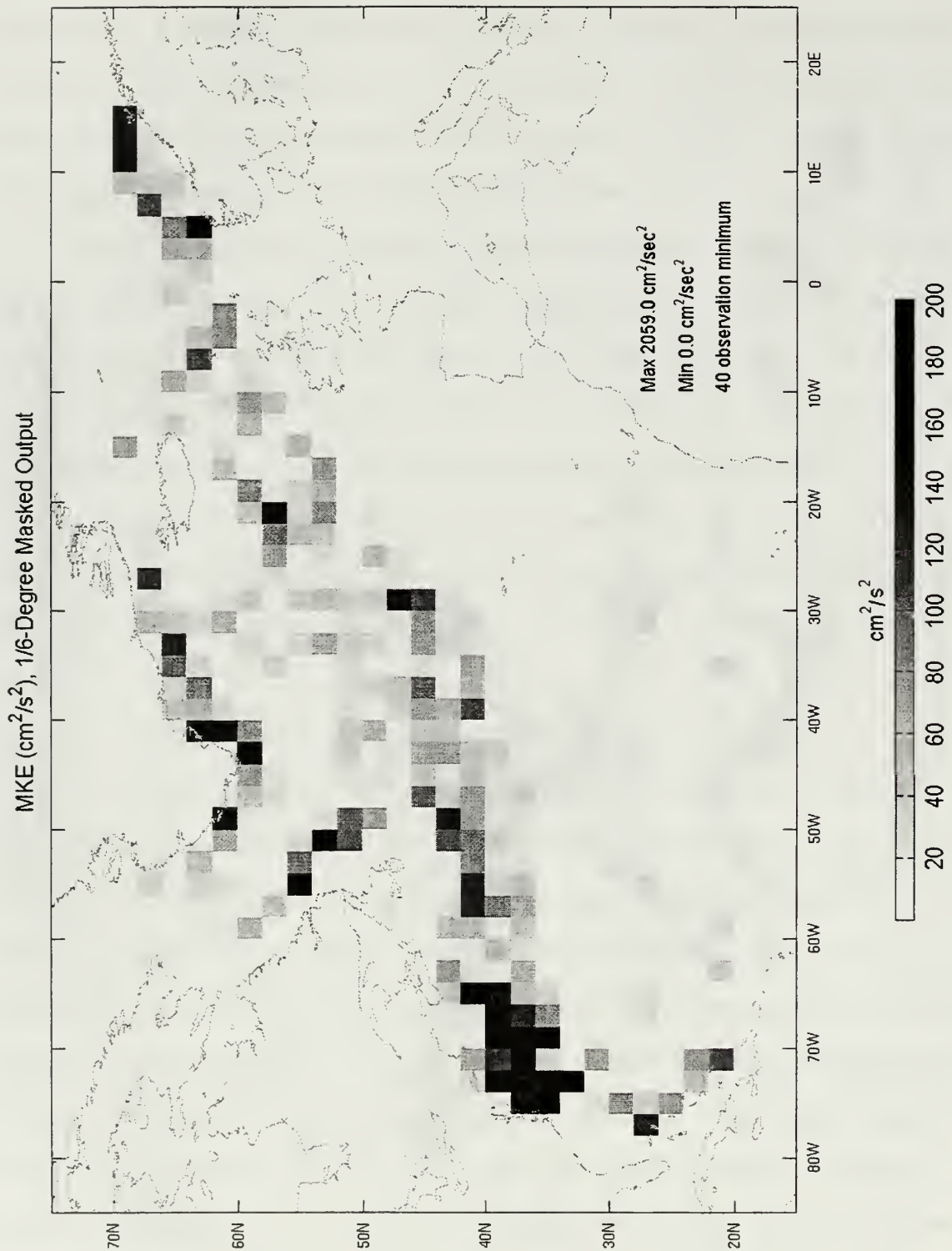observations contain no information and are in white.

58

to be exaggerated in the regions 28°W-38°W, 38°N-46°N and 26°W-36°W, 54°N-60N°, respectively.

The energy associated with the North Atlantic Current is too high west of 24°W and north of 52°N. Together, these effects indicate that though there is obvious spatial mismatch in MKE, the total over the path of the Gulf Stream may be reasonable.

The ratio plot of model MKE/drifter MKE (not shown) indicates the model exaggerates MKE in the latitude band 26°N to 30°N, and underestimates MKE at latitudes 30°N to 34°N. These effects correspond to the model's artificial front at the former latitudes, and the Azores Front represented by the drifters at the latter. The Eastern Labrador Sea is a region where MKEs are exaggerated to a large degree, in the ratio sense. The actual magnitude of the difference is quite small, however.

The MKE plots and MKE ratio plots both indicate good agreement between model and data along continental boundary currents, with the exceptions noted above. There is fairly good agreement along the North Equatorial Current in the eastern basin.

Figure 17 displays histograms of drifter MKE and model MKE. The histograms reveal nearly identical energy distributions, indicating that the differences between model and drifter MKEs are mainly in the spatial patterns.

The bottom plot of Figure 17 shows the distribution of model MKE/drifter MKE with respect to drifter MKE. A
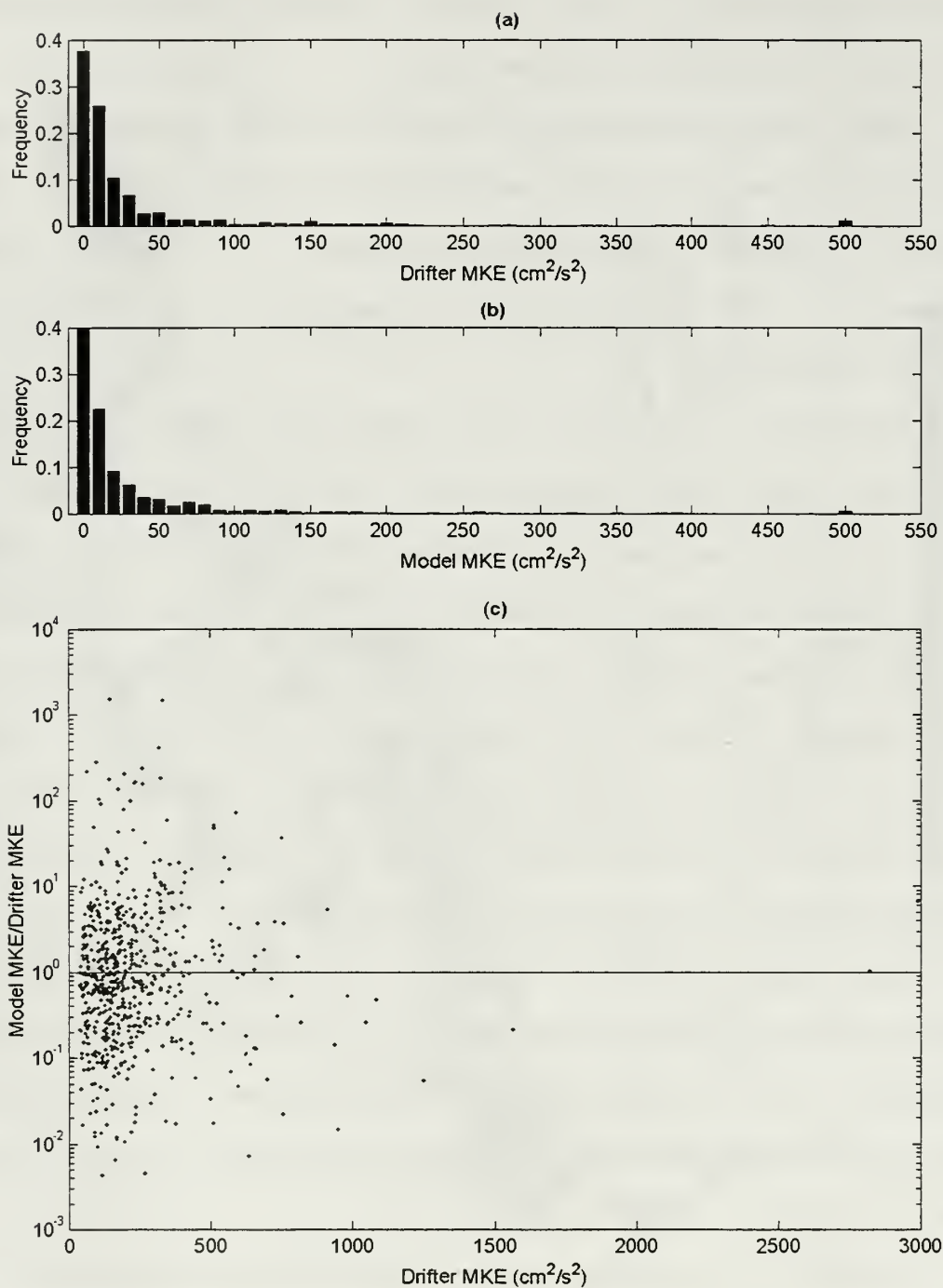
59

Figure 17. Plots (a),(b): Normalized frequency histograms of MKE (cm^2/s^2) for drifter data and masked 1/6-degree model output. Plot (c): Variation of the ratio model MKE/drifter MKE with drifter MKE (cm^2/s^2). Vertical scale is on a log (base 10) axis. For all three plots, bins with fewer than 40 daily observations for either drifter data or model output are not represented.

significant vertical trend in the graph would indicate that the model's pattern of departure (overestimation, underestimation) from the actual data had some dependence on the energy level. As indicated by the plot, there is some evidence, though not strong, that the model tends toward underestimation with increasing MKE.

4. Comparison of Principal Variance Components and Eddy Kinetic Energy

Figures 18 and 19 give the principal standard deviation ellipses for the drifter and masked data. A salient feature is the model's underestimation of variance magnitudes over most of the data domain. Agreement is fairly close, however, south and southeast of Greenland, north of Iceland, east of the Mid Atlantic Ridge along the course of the North Atlantic Current, and along the Norwegian Atlantic Current. As with MKE, an artificial contrast in variational energy is driven by the displaced Northwest Corner and delayed northward turn of the Gulf Stream. Model EKEs are slightly higher than drifter values in the region 26°W-34°W, 42°N-56°N; in the actual Northwest Corner they are underestimated. Model EKEs are exaggerated in the region 70°W-76°W, 34°N-40°N, due at least in part to the spurious anticyclone.

A plot of drifter EKE (not shown) clearly shows the Azores Front extending across the eastern basin, from 46°W to the North African coast, in a roughly 4 degree band. This
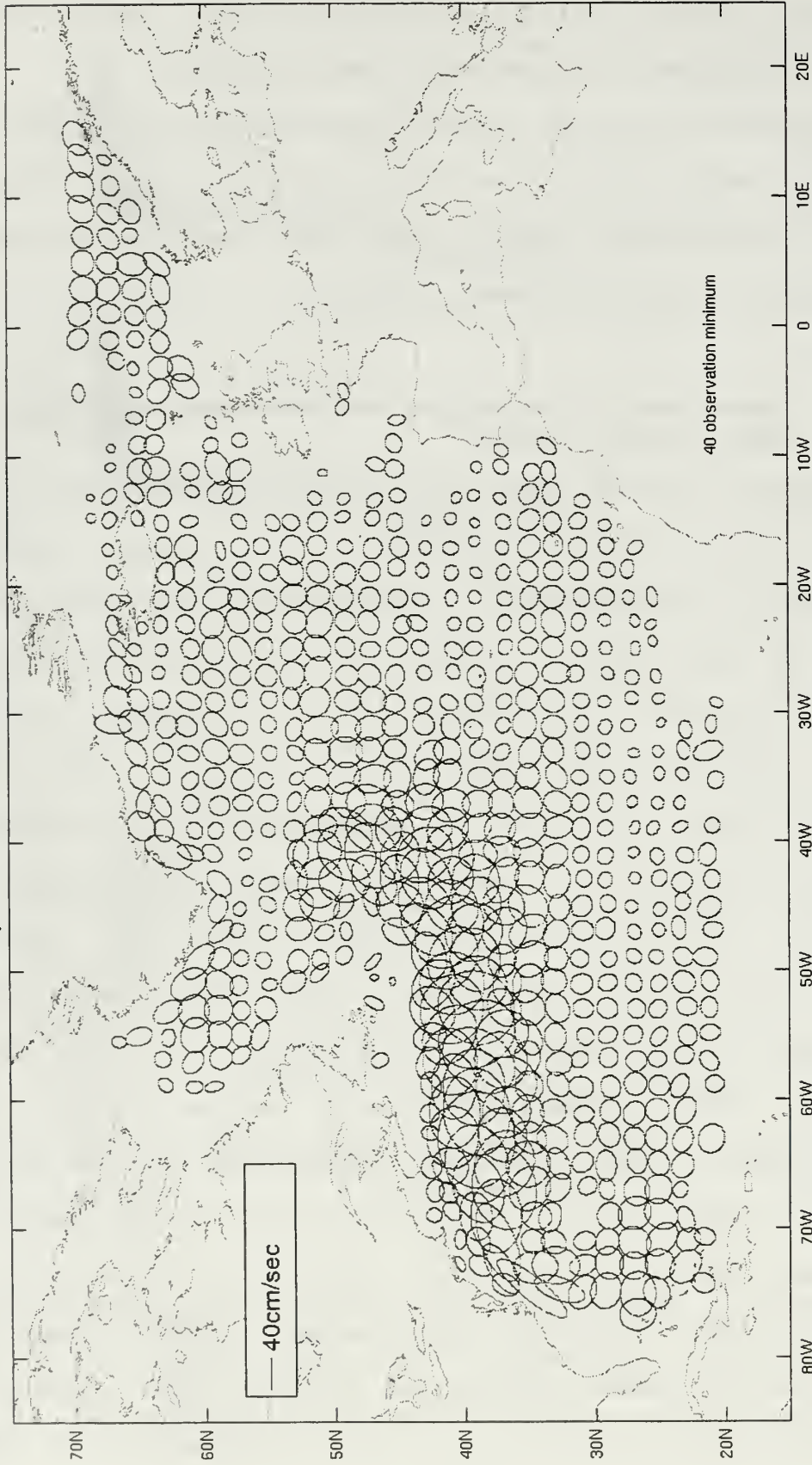
Figure 18. Standard deviation ellipses of velocity (cm/s) oriented along principal variance axes. Drifter data, January 1, 1993 to December 31, 1997. Lengths of half-axes correspond to the square roots of the principal variance eigenvalues. Ellipses for bins with fewer than 40 daily observations not shown.

62

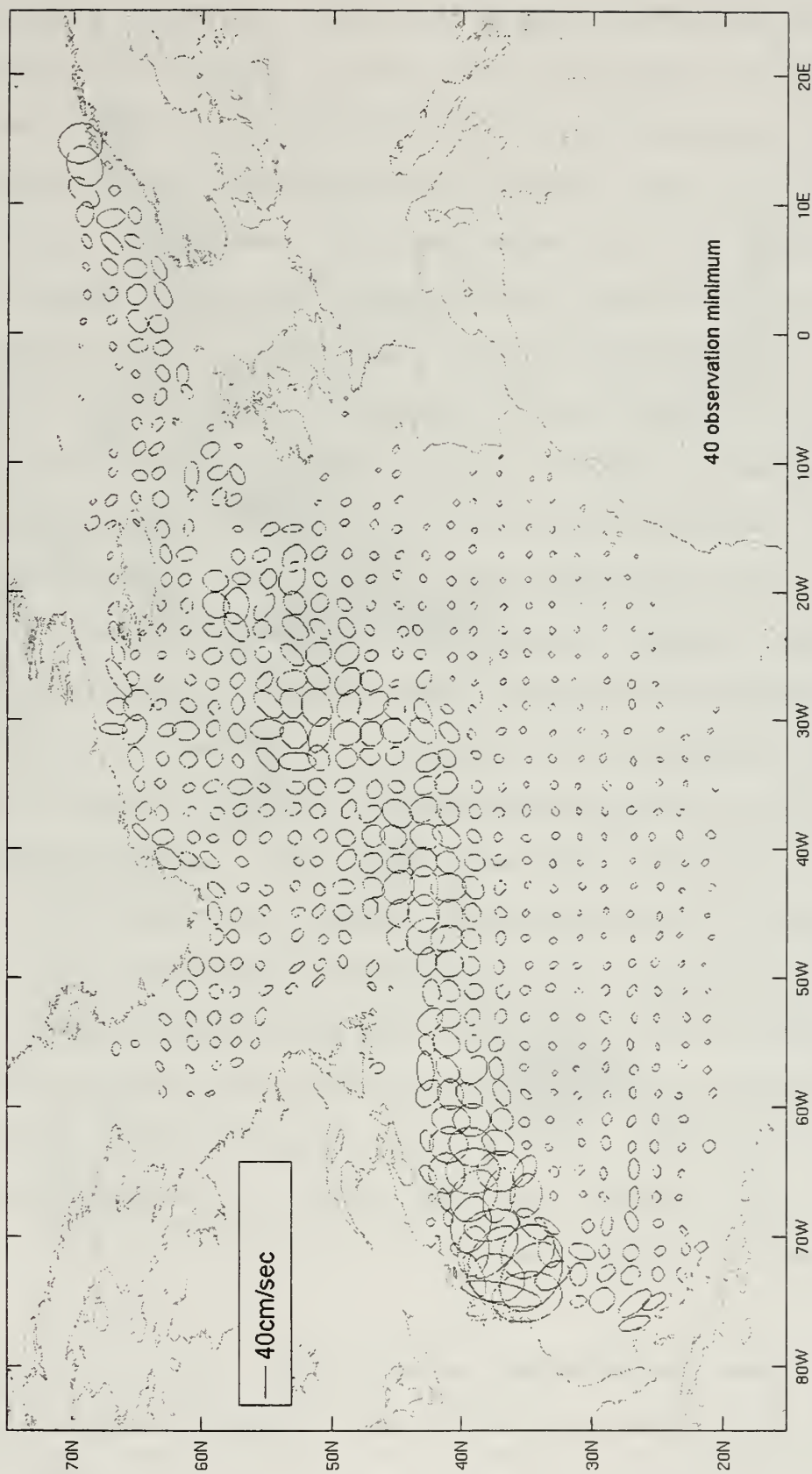Principal Standard Deviation Ellipses, 1/6-Degree Masked Output

Figure 19. Standard deviation ellipses of velocity (cm/s) oriented along principal variance axes. Masked 1/6-degree model output, January 1, 1993 to December 31, 1997. Lengths of half-axes correspond to the square roots of the principal variance eigenvalues. Ellipses for bins with fewer than 40 daily observations not shown.

63

feature is evident in the ellipse plot as well. A similar zonal band of relatively high EKE is indicated from 24°N, apparently associated with the North Equatorial Current's contribution to the Sargasso Sea recirculation. The absence of this band in the masked data is consistent with the model's more uniform recirculation pattern. Though not evident in the ellipse plots, the model's spurious front shows up in the ratio plot of model EKE/drifter EKE (Figure 20). Energies are still underestimated, but the artificial contrast is evident in the latitude band 26°N-30°N. With the exceptions of the preceding features, the differences in variational energy between model and data appear to be mainly in scale, the spatial trends being otherwise similar.

The histograms of Figure 21 reveal a unimodal distribution to the drifter EKE, with a most frequent value of about 100 cm^2/s^2. The model EKE has a nearly monotonic distribution, with almost all values occurring below 250 cm^2/s^2. A histogram of the ratio model EKE/drifter EKE (not shown) indicates the model under-represents EKE in well over three-quarters of the bins. Most values fall within a range of 0.15 to 0.5. The bottom plot of Figure 21 shows that the quantity model EKE/drifter EKE shows no pronounced trend with respect to energy level.

5. **Test for equality of mean flow**

The two tests for equality of means described in section A are done ten times for each bin having at least 40
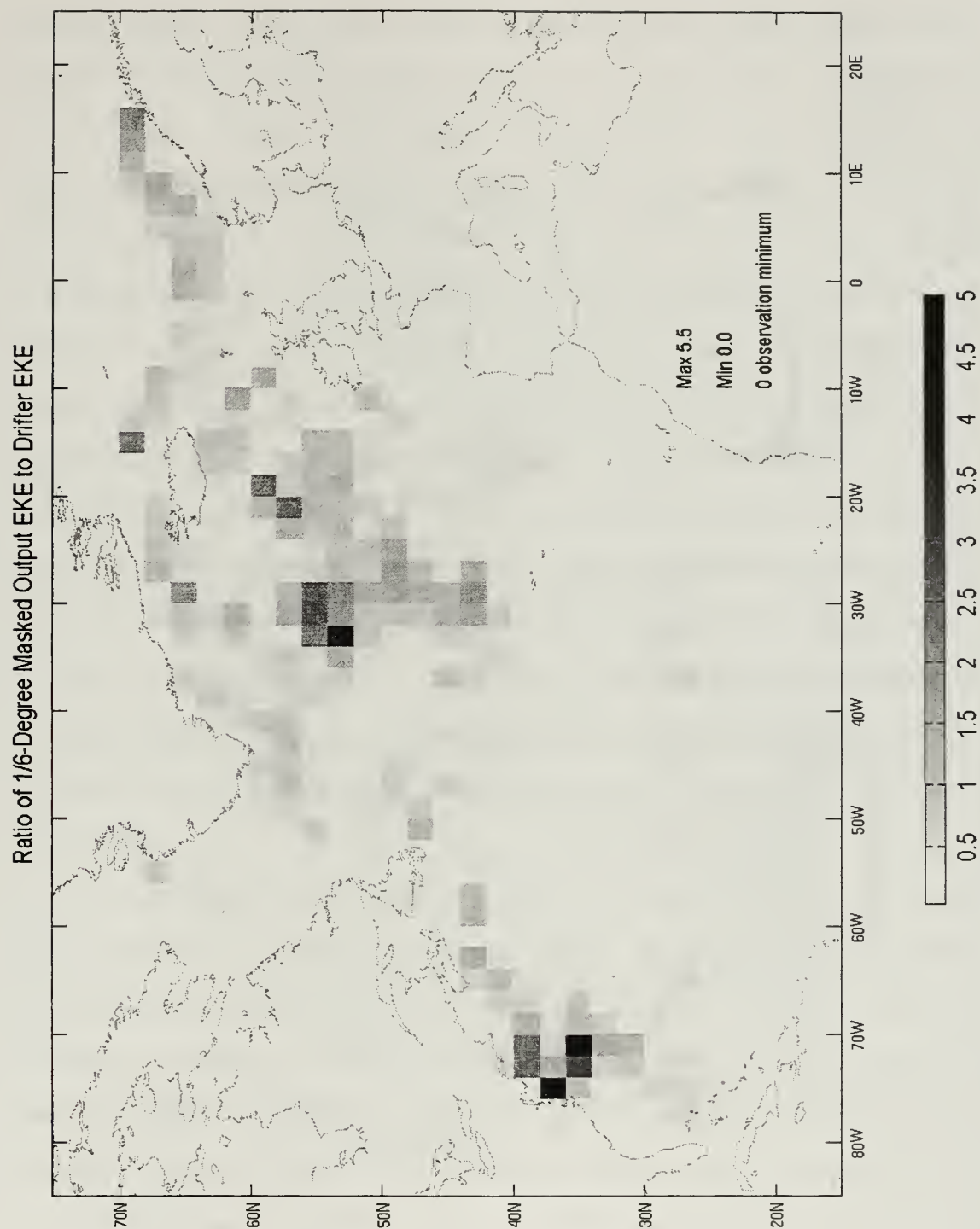
Figure 20. Ratio of 1/6-degree model EKE to drifter EKE for the 5-year time domain, January 1, 1993 to December 31, 1997. Bins with fewer than 40 daily observations for either drifter data or model output contain no information and are in white.
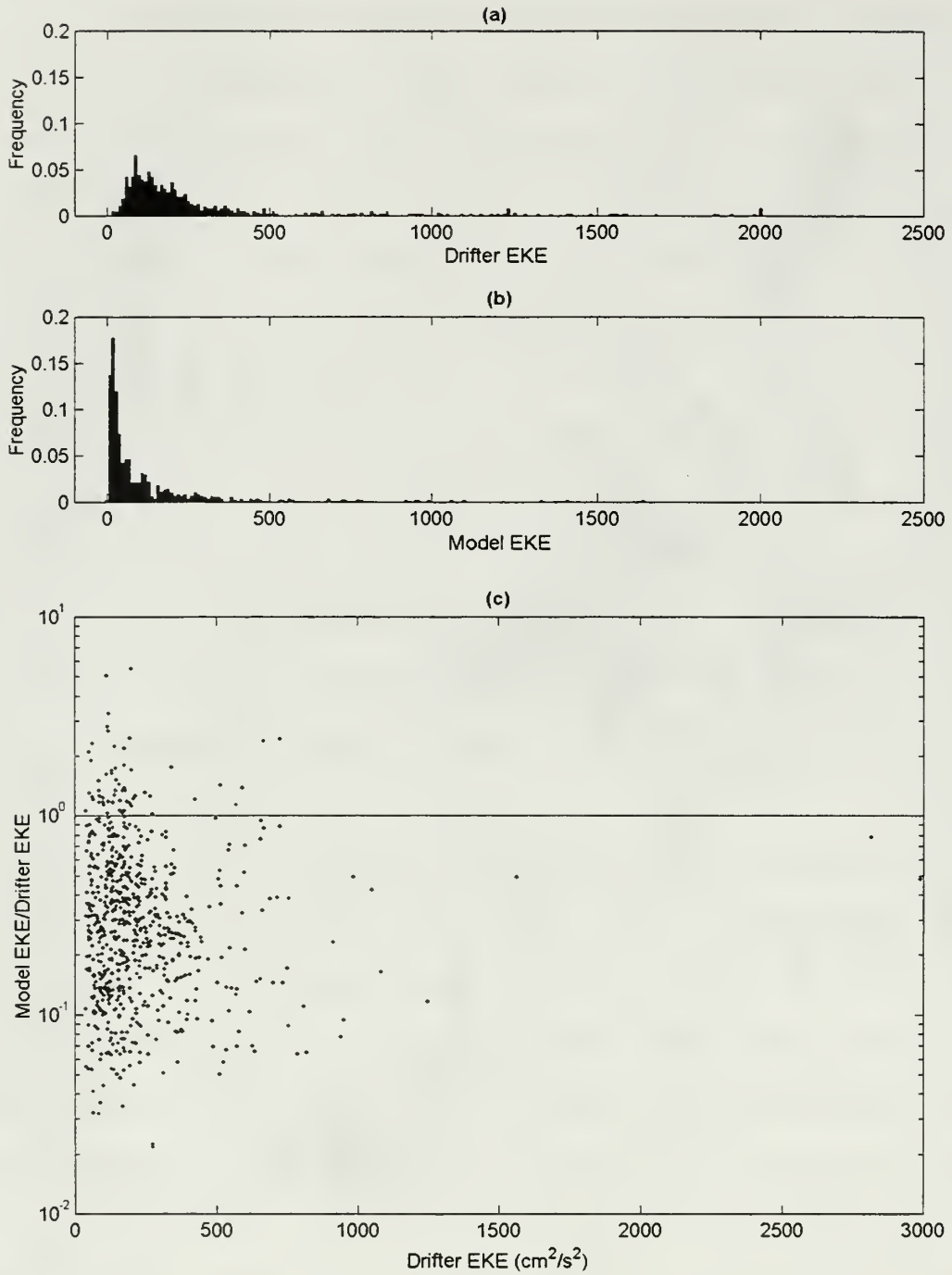
65

Figure 21. Plots (a),(b): Normalized frequency histograms of EKE (cm^2/s^2) for drifter data and masked 1/6-degree model output. Plot (c): Variation of the ratio model EKE/drifter EKE with drifter MKE (cm^2/s^2). Vertical scale is on a log (base 10) axis. For all three plots, bins with fewer than 40 daily observations for either drifter data or model output are not represented.

observations. As described above, the tests take into account the variance structures of the model output and drifter data. Figure 22 shows the results of the tests. The gray shades indicate the number of times out of ten the given bin failed the given test for equality of means. There is a high degree of similarity in the results of both tests, and the salient characteristics are the same. Both indicate nearly binary results; generally, either significant disagreement is found in almost all ten tests, or else few rejections occurred at 5% level of significance. The spatial patterns are equally distinct, and reflect the earlier findings of agreement (more properly, lack of disagreement) in the northern marginal currents. The northern extremes of the Gulf Stream south of Newfoundland, and the northeast and southwest boundaries of the Subtropical Gyre also see few rejections.

Significant rejection occurs, however, where the Gulf Stream separates from the continental shelf, and where flow continues around the Newfoundland Grand Banks into the Northwest Corner. These areas have already been noted as showing MKE mismatch; there is significant direction mismatch west of the Grand Banks as well, as a result of the model's delayed northern turn. To the south and southwest of Iceland many rejections occur due to the Northwest Corner's artificial presence. The eastern boundary of the Subtropical Gyre shows a large number of rejections. This is consistent with the lack of resolution of the Canary Current and Azores
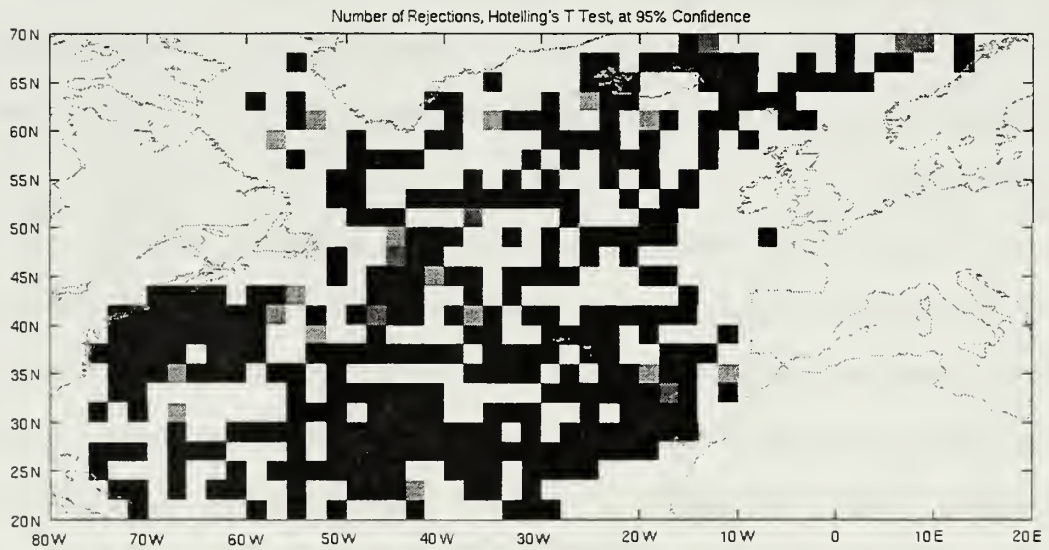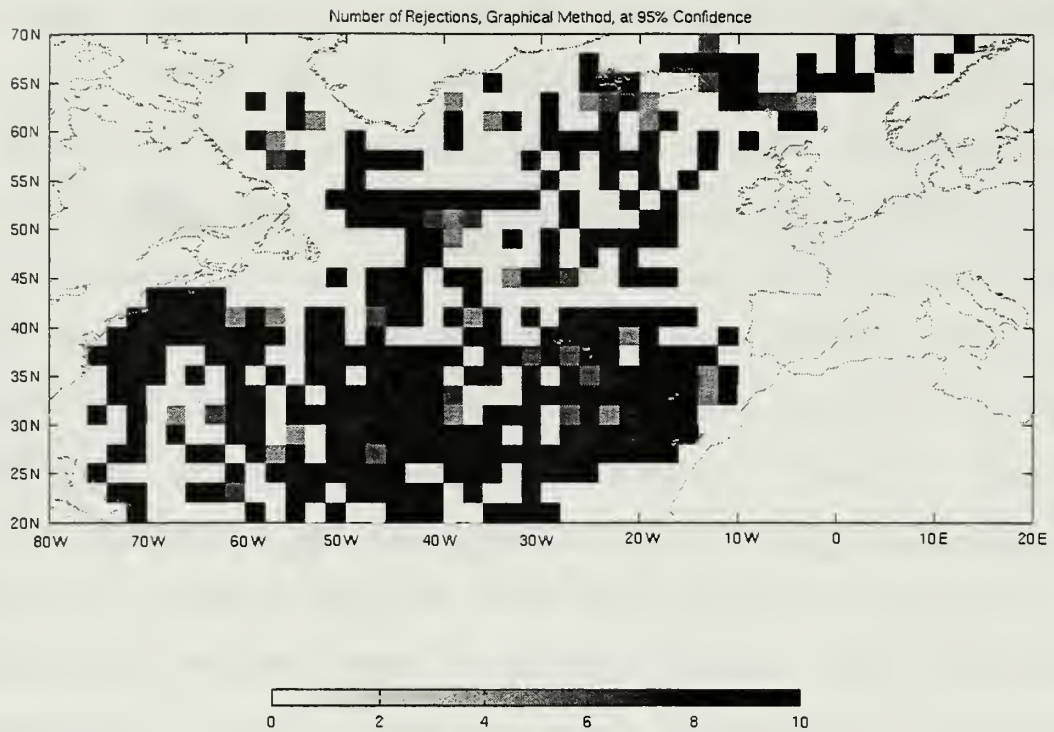
Figure 22. Results of tests (section IV.B.5) for equality of
mean velocities between drifter data and 1/6-degree model
output. Ten tests per bin were conducted to detect
significant departures from equality at confidence level 95%
($\alpha = 0.05$). Each used unique independent subsets of data
and output. The color scale indicates the number of failed
tests.

Front in the model, while the features are clearly indicated by the drifters. The large block of rejections over the central Subtropical Gyre south of roughly 36°N seems to be largely due to direction mismatch. Here, the model's surface transport has a moderate meridional component due to recirculation from the Gulf Stream and North Equatorial Current, while the effect is not as pronounced in the data.

C.   EULERIAN RESULTS: 1/10-DEGREE MODEL

The following results derived from 1/6- and 1/10-degree model output over the period January 1, 1993 to December 31, 1994, and the corresponding drifter data spanning this time domain. As the data and model output are fewer in number than for the 1993 - 1997 comparisons, these results should be considered preliminary.

1.   Mean Flow Comparison

Figure 23 shows the mean circulation indicated by the drifter data for years 1993 - 1994. Figures 24 and 25 give the corresponding two-year plots for the 1/6-degree and 1/10-degree models, respectively. The patterns evident in the 1993 - 1997 drifter plot are still present in the 1993 - 1994 subset, though much resolution of the Canary Current is lost. A comparison of Figure 25 with Figure 24 shows striking differences. The strong, coherent recirculation patterns in the middle Subtropical Gyre and the wide, laminar eastward flow between 40°N and 52°N are no longer
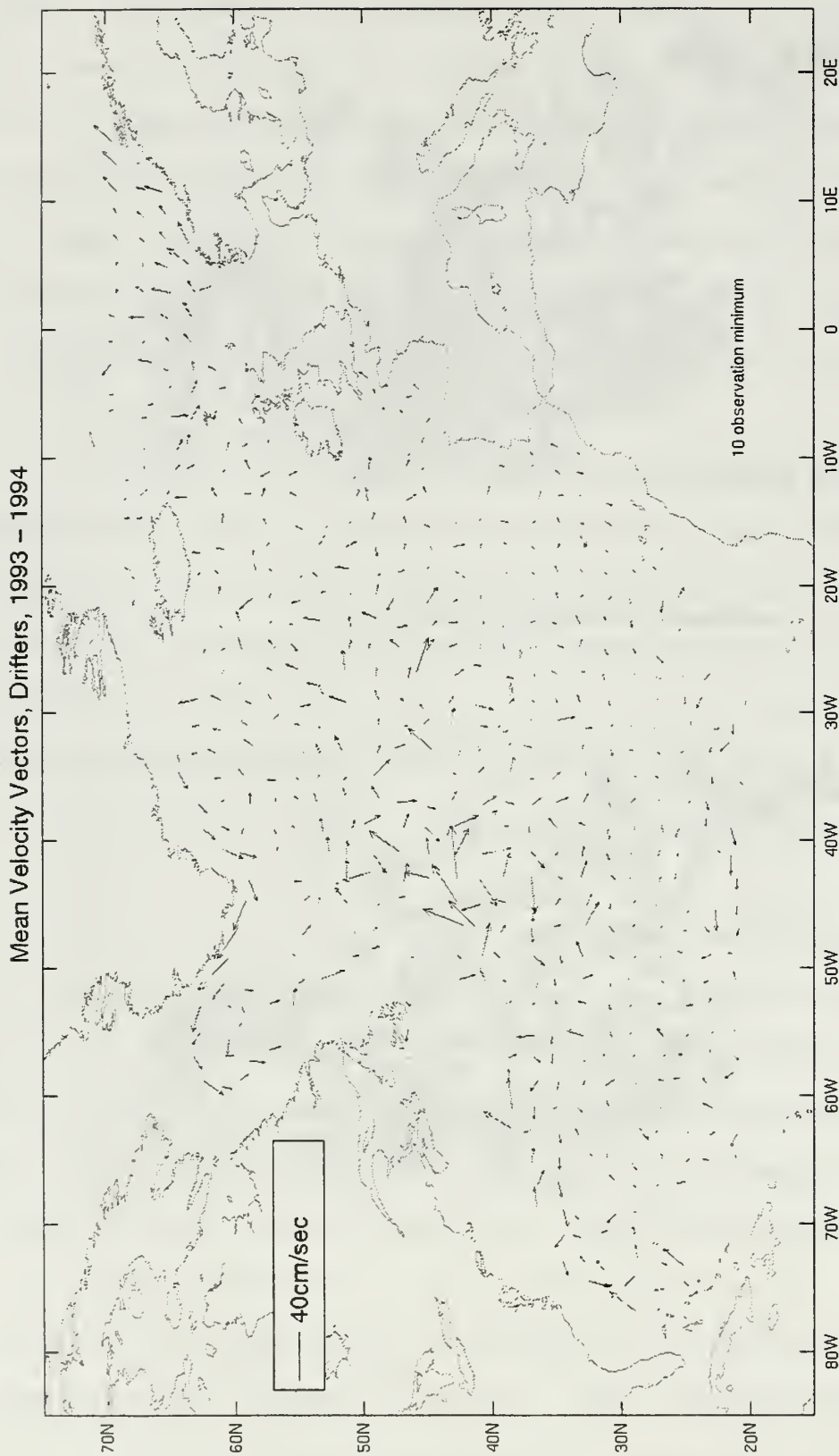
69

Figure 23. Mean velocity vectors (cm/s) for the actual drifter data over the 2-year time domain, January 1, 1993 to December 31, 1994. Tails of vectors are anchored at the centroids of the observation points. Vectors for bins with fewer than 10 daily observations not shown.

Figure 24. Mean velocity vectors (cm/s) for the masked 1/6-degree model output over the 2-year time domain, January 1, 1993 to December 31, 1994. Tails of vectors are anchored at the centroids of the observation points. Vectors for bins with fewer than 10 observations not shown.
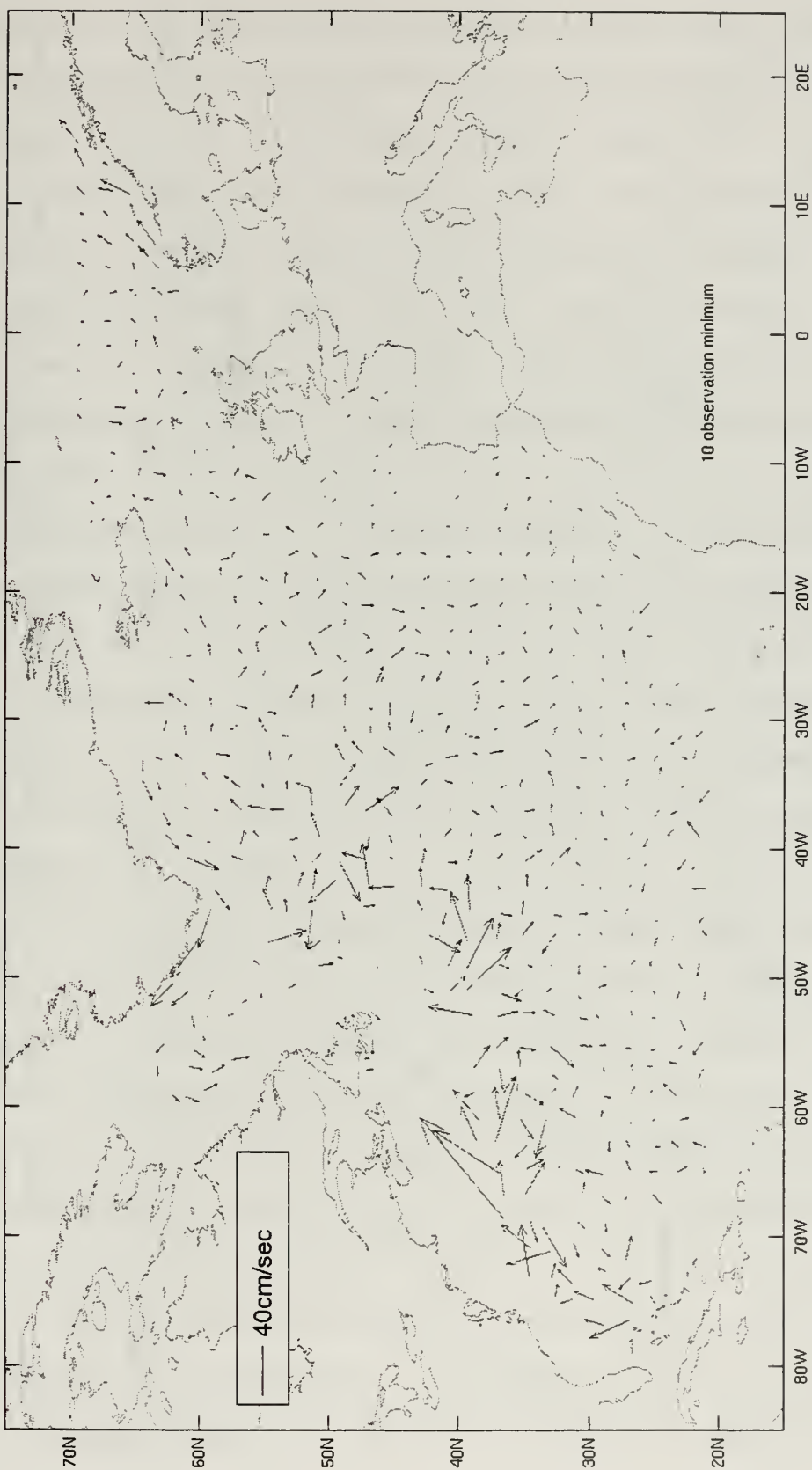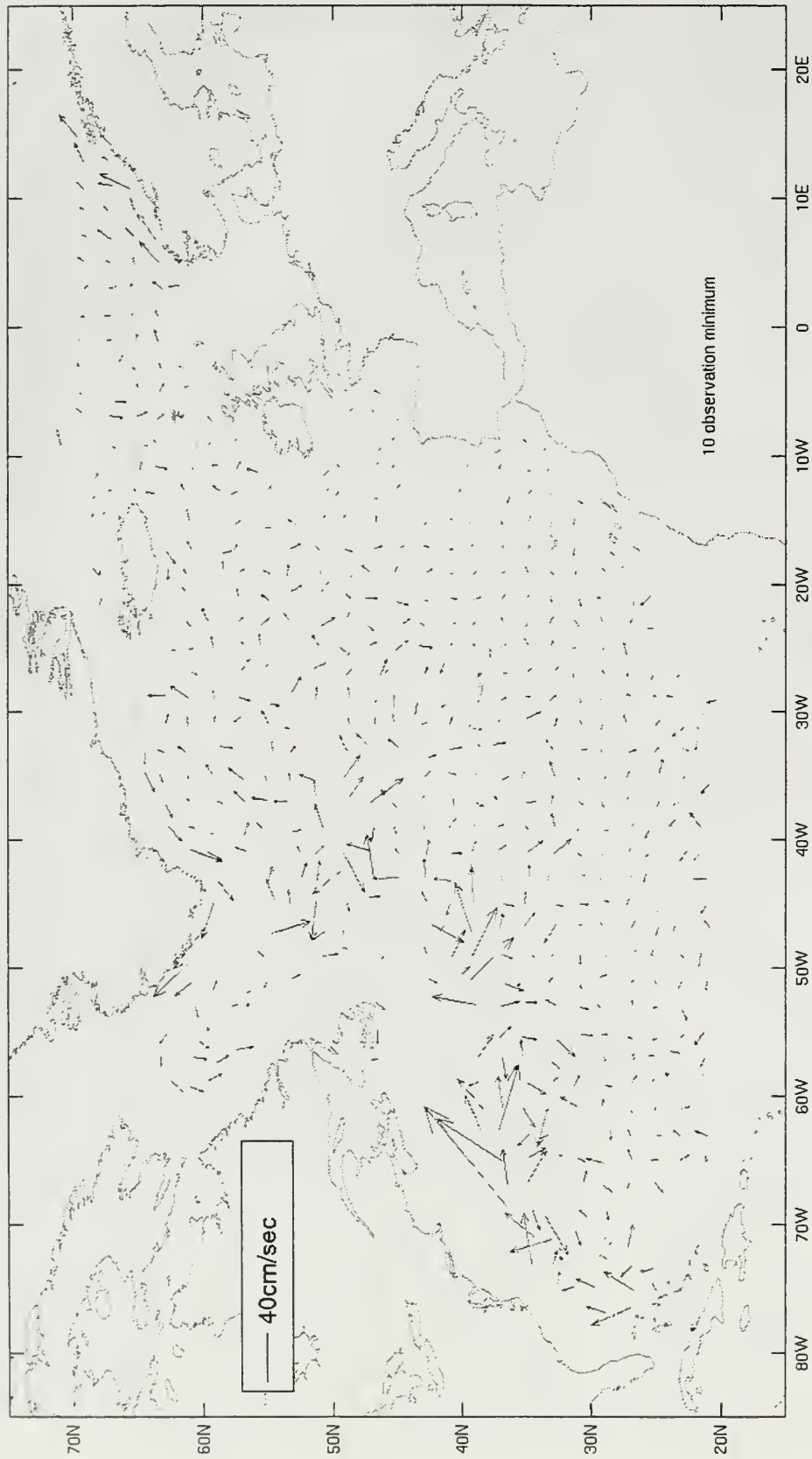
Figure 25. Mean velocity vectors (cm/s) for the masked 1/10-degree model output over the 2-year time domain, January 1, 1993 to December 31, 1994. Tails of vectors are anchored at the centroids of the observation points. Vectors for bins with fewer than 10 observations not shown.

present. The spurious front between 26°N and 30°N is still indicated, but is much attenuated and of lesser latitudinal extent in the 1/10-degree model. There is little direct evidence that the 1/6-degree model's artificial anticyclone has been removed, due to the sparsity of data over the shelf region between Cape Cod and Cape Hatteras. However, ancillary analyses of mean sea level height show no anticyclone at this location (personal communication, Julie McClean). The Northwest Corner now occurs in the correct longitude band. It no longer appears to interfere with the Irminger Current, and the exaggerated flow energy it created to the east of the Mid Atlantic Ridge is gone. The weak northeast drift south of Iceland is closer in magnitude to the drifters' values. The Azores Front now clearly appears in the model between 32°N and 34°N, a result also noted by Smith et al. (1999).

The model's velocity field is too strong over most of the Gulf Stream and in the Northwest Corner, however. Elevated velocities associated with the feature extend too far to the north and west as well. In contrast, the Canary Current still appears absent, though this result must be weighted with the sparsity of data and the weakness of the actual feature.

Noting these exceptions, we see that the 1/10-degree formulation eliminates significant shortcomings in the 1/6-degree model. The spurious effects seen in the latter are either eliminated or greatly attenuated. The 1/10-degree

model appears to capture much more of the turbulent nature of the North Atlantic Ocean, while resolving most of the features indicated by the drifters.

2.   Mean Kinetic Energy Comparison

Plots of MKE (Figures 26 and 27) reflect the improvements noted above; additionally MKEs in the North Equatorial Current appear to be better matched by the 1/10-degree model. Though the model's amplification of MKE along the Gulf Stream is clear, the high values associated with the northward turn do not extend as far to the southeast as the drifters indicate. The 1/10-degree model appears to underestimate MKE in the eastern reaches of the Gulf Stream, 20°W-34°W, 44°N-52°N.

A ratio plot of model MKE/drifter MKE (not shown) reveals the large improvement in spatial distribution of MKE over the central Subtropical Gyre. The strong zonal banding produced by the model's spurious front and its apparent lack of an Azores Front is no longer present.

The histograms of Figure 28 have nearly the same shapes as those for the 1/6-degree comparisons, again showing differences to be mainly spatial. The one exception is that MKEs above 500 cm^2/s^2 are roughly five times more frequent in the model than in the drifter data, whereas the 1/6-degree model bins had about two times fewer MKE measurements in this band than the drifters. It appears the 1/10-degree
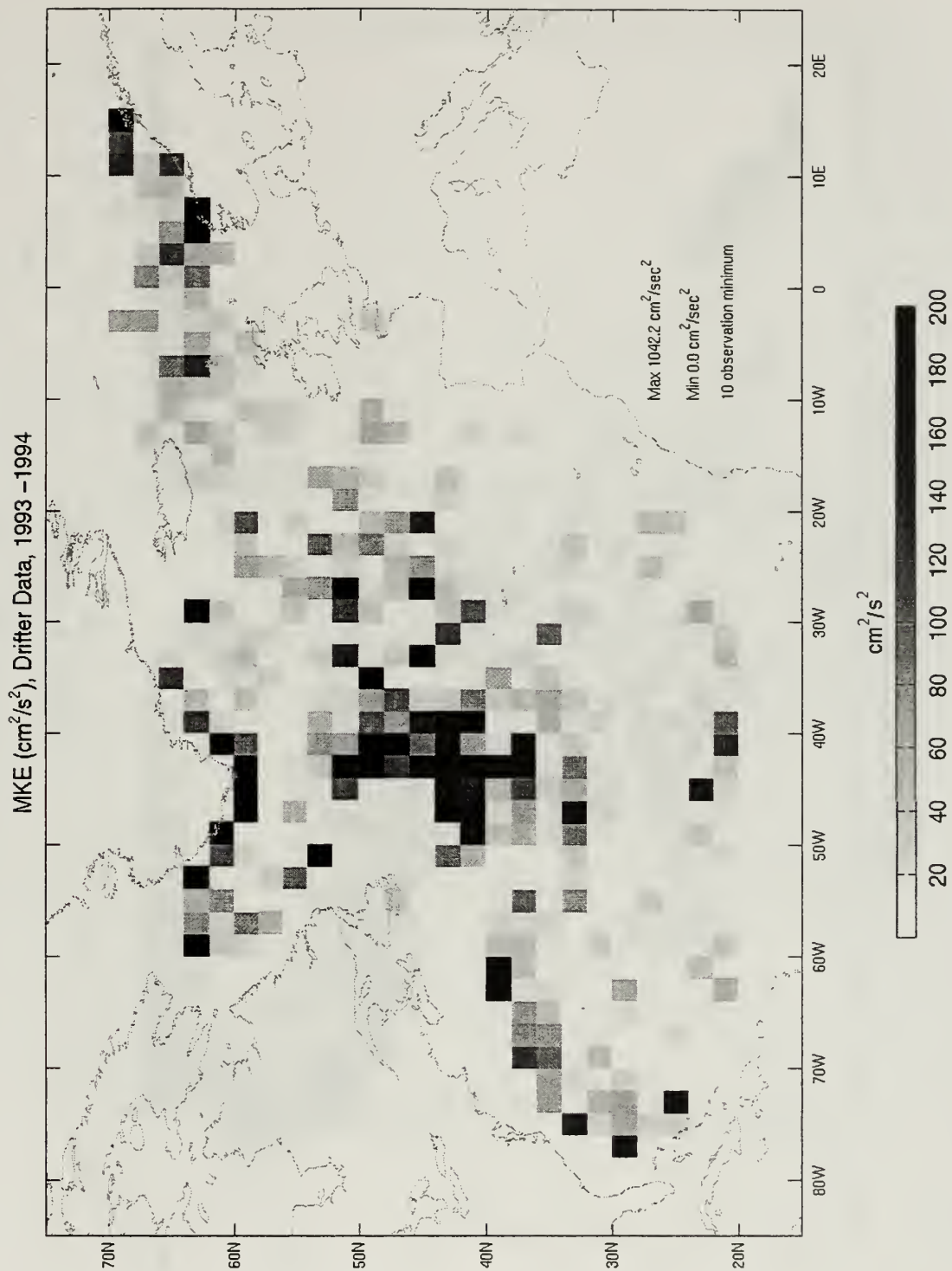
Figure 26. Mean kinetic energy (MKE)(cm^2/s^2) for the actual drifter data over the 2-year time domain, January 1, 1993 to December 31, 1994. Bins with fewer than 10 daily observations contain no information and are in white.

Figure 27. Mean kinetic energy (MKE)(cm²/s²) for the masked
1/10-degree model output over the 2-year time domain,
January 1, 1993 to December 31, 1994. Bins with fewer than
10 daily observations contain no information and are in
white.

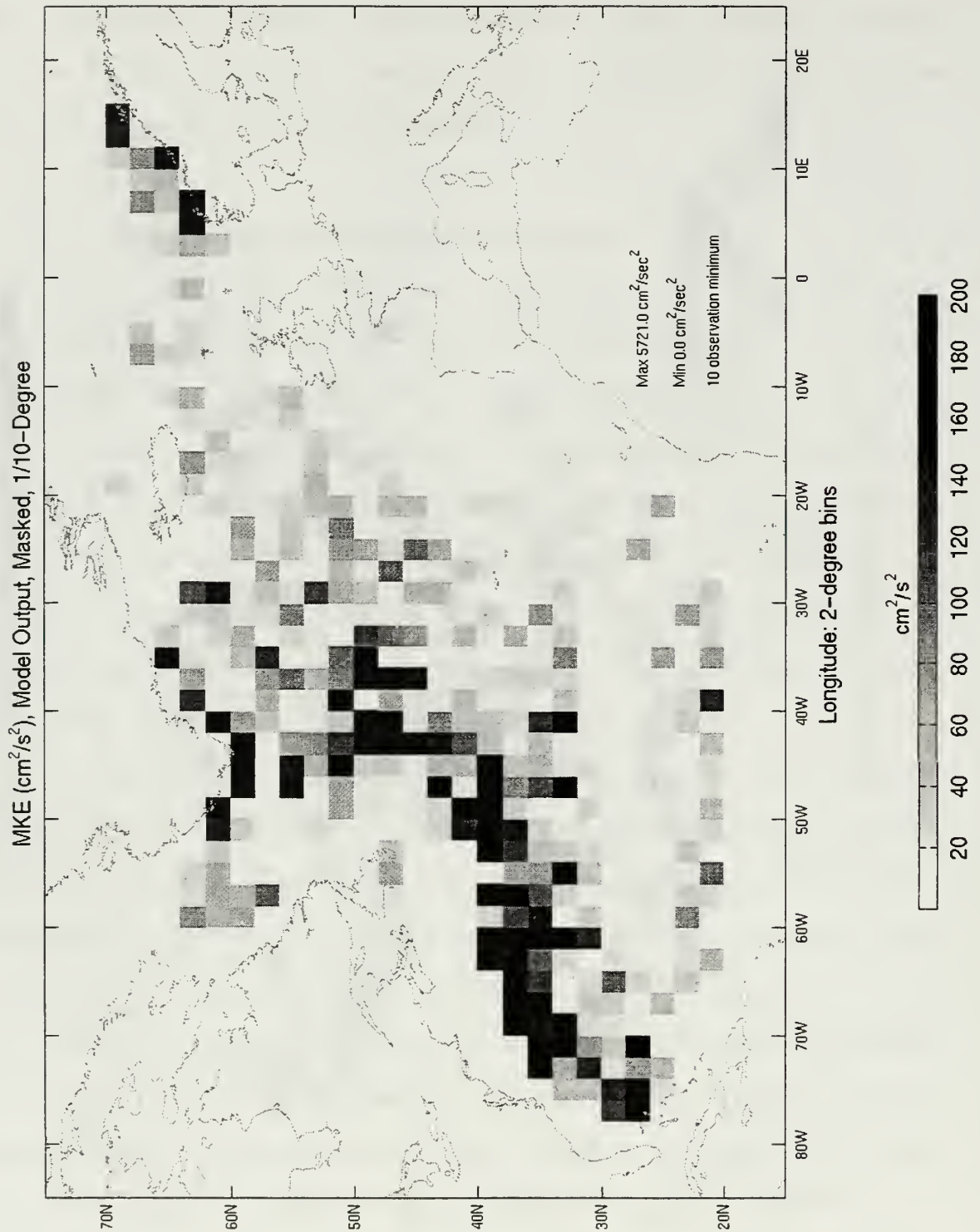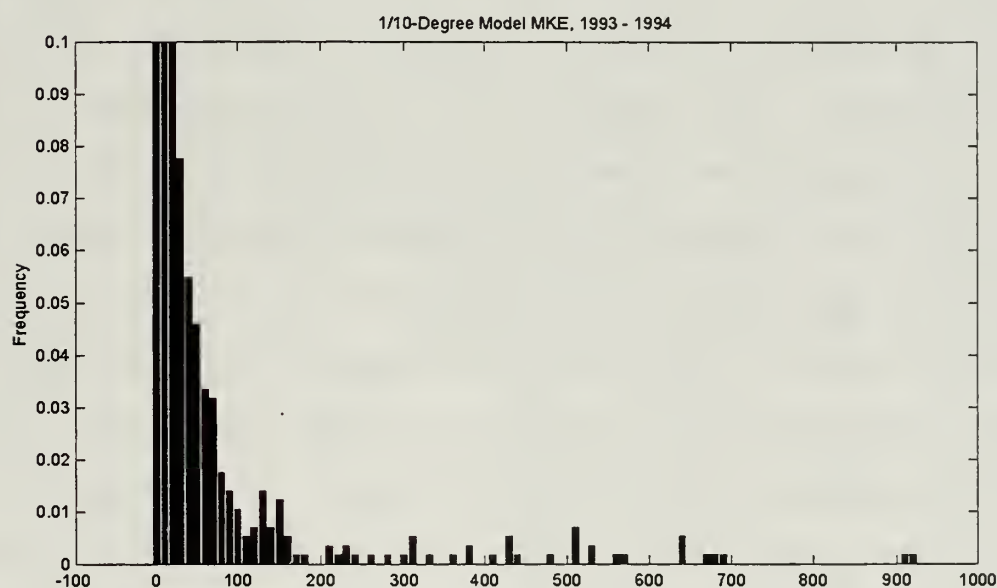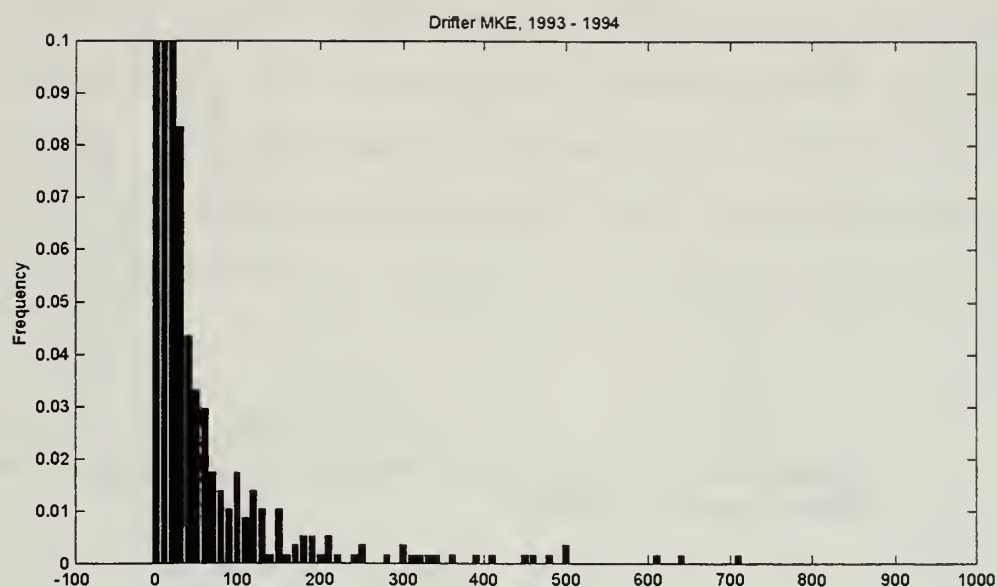Figure 28. Normalized frequency histograms of MKE (cm^2/s^2) for drifter data and masked 1/10-degree model output. The time domain is January 1, 1993 to December 31, 1994. Bins with fewer than ten daily observations for either drifter data or model output are not represented.

model tends to slightly overestimate MKE on the average, whereas no strong pattern was shown by the 1/6-degree model. This observation is reflected by the histogram (not shown) of model MKE/drifter MKE, which gives a shape similar to the corresponding histogram of Figure 17, but shifted to the right.

3. Comparison of Principal Variance Components and Eddy Kinetic Energy

Figure 29 shows the principal standard deviation ellipses for the drifter data over the period 1993 – 1994. Figures 30 and 31 give the corresponding plots for the 1/6-degree model and 1/10-degree model, respectively, over that time interval. The increase in variance magnitude achieved by the 1/10-degree model is evidently quite significant. Resolution of variability over most of the Subtropical Gyre is highly improved. The Azores Front is now clearly visible, where it was not indicated in the plots for the 1/6-degree model. Variability over most of the latitudes north 50°N is well represented. The model continues to underestimate in the Nordic seas north of 66°N, though to a smaller degree. The variability over the Labrador Basin is now quite close to that indicated by the drifters. Over the Rockall Plateau and west to roughly 26°W, variability is underestimated, though only slightly. This information is significant because the 1/6-degree model variances for this region were masked by the effects of the displaced Northwest Corner.

Figure 29. Standard deviation ellipses of velocity (cm/s) oriented along principal variance axes. Drifter data, January 1, 1993 to December 31, 1994. Lengths of half-axes correspond to the square roots of the principal variance eigenvalues. Ellipses for bins with fewer than 10 daily observations not shown.

79

Figure 30. Standard deviation ellipses of velocity (cm/s) oriented along principal variance axes. Masked 1/6-degree model output, January 1, 1993 to December 31, 1994. Lengths of half-axes correspond to the square roots of the principal variance eigenvalues. Ellipses for bins with fewer than 10 daily observations not shown.
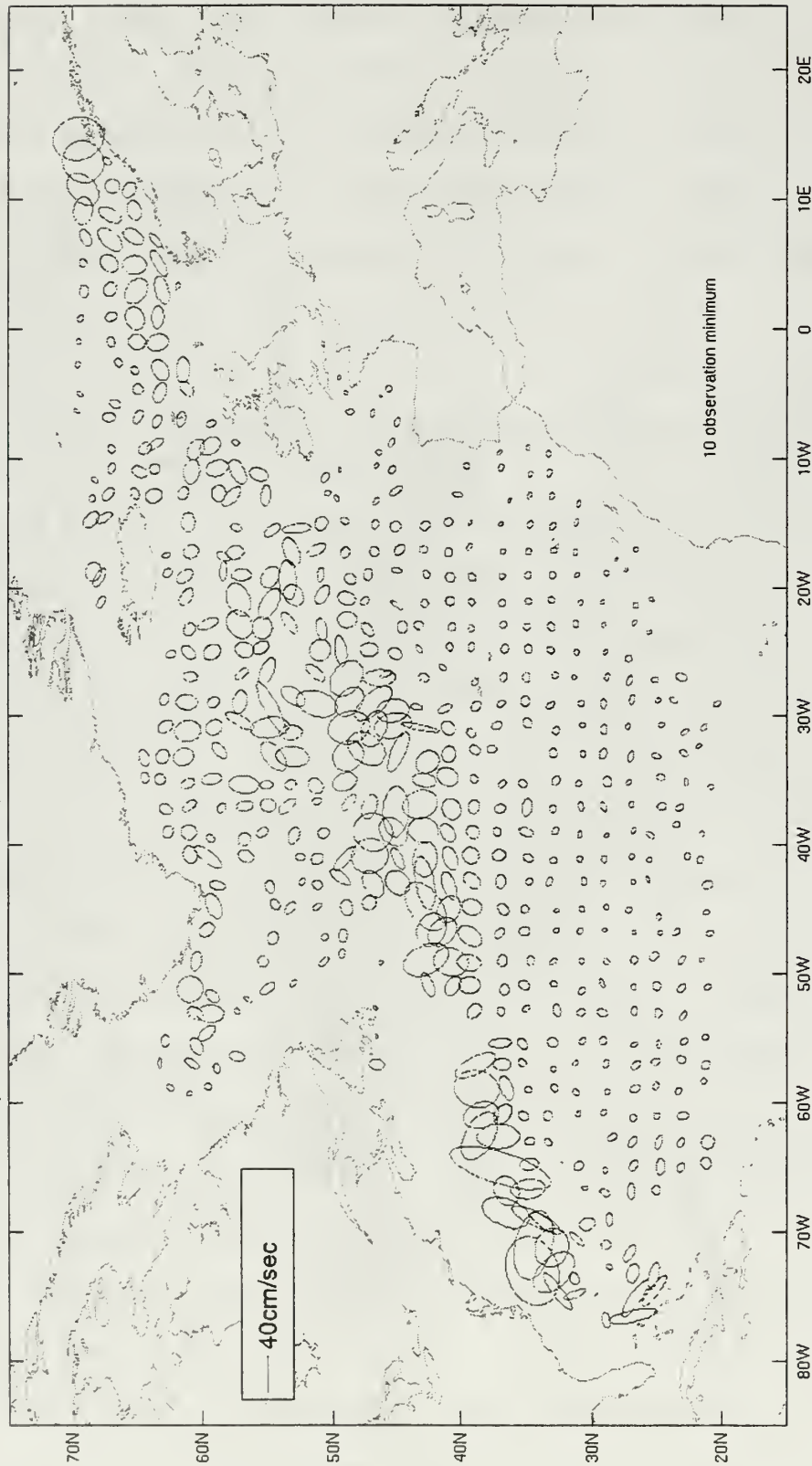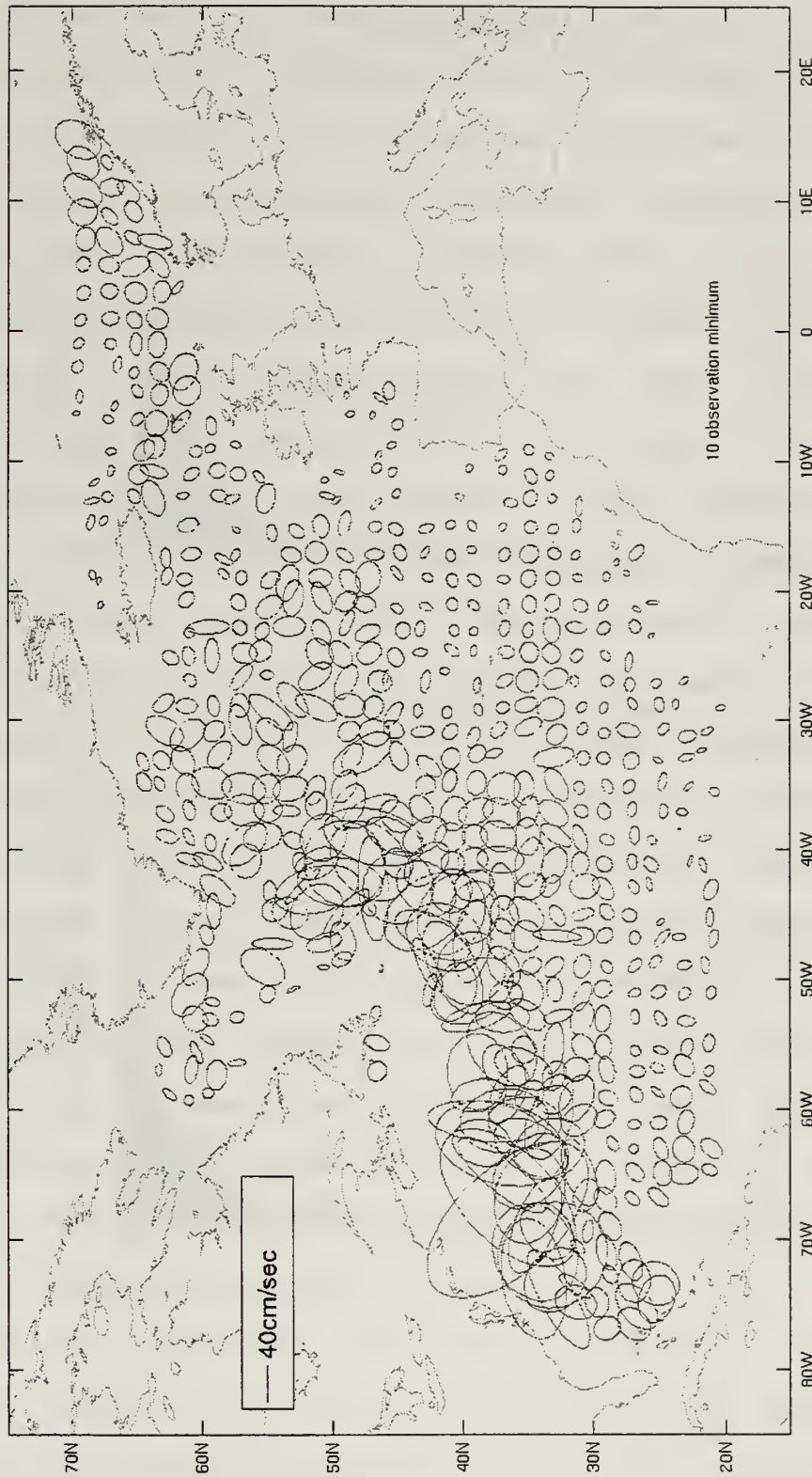
Figure 31. Standard deviation ellipses of velocity (cm/s) oriented along principal variance axes. Masked 1/10-degree model output, January 1, 1993 to December 31, 1994. Lengths of half-axes correspond to the square roots of the principal variance eigenvalues. Ellipses for bins with fewer than 10 daily observations not shown.

The decrease in variance magnitudes away from the center of the Northwest Corner is more prolonged in the 1/10-degree model than in the data. The result is that variances are exaggerated around its periphery, as evident in Figures 29 and 31. Variance is exaggerated as well in the lower Gulf Stream, where it separates from the continental shelf. This was the case as well for the 1/6-degree model, but the overestimation is greater in magnitude and eastward extent in the 1/10-degree model. Elevated EKEs (the mean of the principal variance components) extend too far south in this region as well, a result noted by Smith et al. (1999).

Figure 32 shows histograms of model EKE and drifter EKE for the 1/10-degree model. A comparison with the 1/6-degree model histogram of Figure 21 shows the 1/10-degree model distributes much less energy in the $0 - 50$ cm^2/s^2 band. The 1/10-degree model shows a notable amount of energy in excess of 2000 cm^2/s^2, whereas the maximum EKE seen in the 1/6-degree model was 1641.3 cm^2/s^2. The energy distribution of the 1/10-degree model corresponds more closely to that of the drifters in the $0 - 1000$ cm^2/s^2 band. Energies beyond 1000 cm^2/s^2 are more prevalent in the 1/10-degree model output than in the drifter data, whereas the opposite is true for the 1/6-degree model. In particular, the high energies beyond 2000 cm^2/s^2 are not seen in the drifter data subset. Apparently much of the change in EKE between the 1/6-degree and 1/10-degree formulation takes place at the higher and lower energy levels. A histogram of the ratio
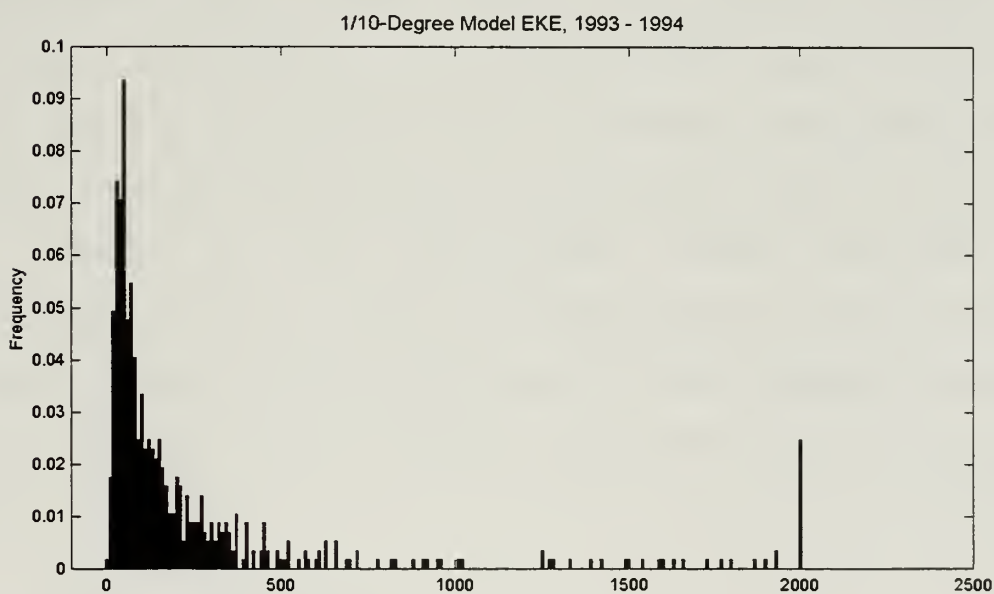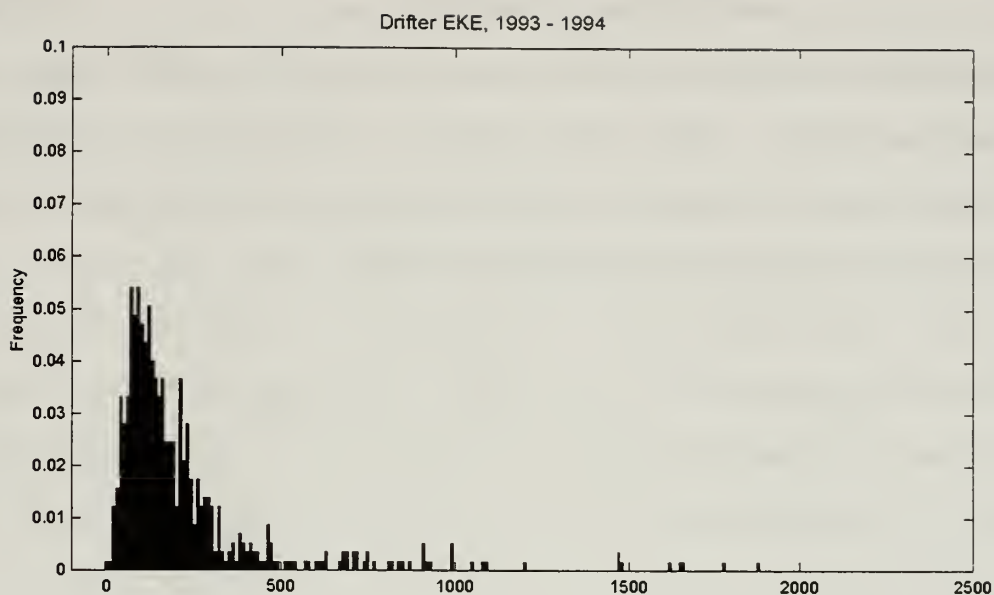
Figure 32. Normalized frequency histograms of EKE (cm^2/s^2) for drifter data and masked 1/10-degree model output. The time domain is January 1, 1993 to December 31, 1994. Bins with fewer than ten daily observations for either drifter data or model output are not represented.

model EKE/drifter EKE (not shown) reveals the 1/10-degree model under-represents EKE significantly less than does the 1/6-degree model. The 1/10-degree histogram's center of gravity is much closer to unity, whereas the center for the 1/6-degree histogram was slightly less than -1/3.

V.   LAGRANGIAN ANALYSIS

For the Lagrangian analysis we divide the geographical domain (section III.B.5) into 5°x5° bins, giving 20 and 10 bins, respectively, in the zonal and meridional directions. For each bin, we obtain drifter velocities as in the Eulerian analysis, and generate velocities for both "same start" and "random start" regimes by the method described in Appendix B. The time domain for the Lagrangian analysis is the five year period January 01 1993 to December 31, 1997.

A Lagrangian description of motion is based upon the trajectories of individual particles. Consequently, statistics based on this approach are defined over a time series of observations. The kernel of all such statistics is the Lagrangian autocovariance function. Through Taylor's (1921) theory of homogeneous turbulence, this function can be related to the steady-state single particle eddy diffusivity and in turn to the Lagrangian integral time and length scales. Formal definitions of these quantities follow below. The notation is adapted from Davis (1991) and Poulain et al. (1996).

A.   FORMULAE AND METHODS

The Lagrangian description requires a geo-temporal reference, or location-time "tag". Let the Lagrangian velocity and displacement at time t of a particle passing through location $\mathbf{x}$ at time t_0 be denoted by $\mathbf{v}(t|\mathbf{x}, t_0)$ and

85

$r(t|\mathbf{x}, t_0)$, respectively. Let the Lagrangian operator $<\bullet>_L$ signify an average taken over an ensemble of particles released randomly from $\mathbf{x}$. Then we can define the Lagrangian mean velocity and Lagrangian mean displacement at time $t_0 + \tau$ of an ensemble of particles released from $\mathbf{x}$ at time t_0 by

$$\mathbf{V}(\tau, t_0, \mathbf{x}) = \left\langle \mathbf{v}(t_0 + \tau | \mathbf{x}, t_0) \right\rangle \tag{7}$$

$$\mathbf{R}(\tau, t_0, \mathbf{x}) = \left\langle \mathbf{r}(t_0 + \tau | \mathbf{x}, t_0) \right\rangle \tag{8}$$

Finally, we denote the residual velocity and displacement about these means as $\mathbf{v}'$ and $\mathbf{r}'$, respectively.

The Lagrangian autocovariance function is defined (Davis, 1991) as

$$P_{ij}(\mathbf{x}, \tau) = \left\langle v_i^{'}\left(t_0 \mid \mathbf{x}, t_0\right) v_j^{'}\left(t_0 + \tau \mid \mathbf{x}, t_0\right) \right\rangle_L . \tag{9}$$

where τ is the time lag of interest, and where the subscripts i and j may take the values 1 for the zonal direction or 2 for the meridional direction. Davis (1991) further defines the single particle eddy diffusivity as

$$\kappa_{ij}(\mathbf{x}, \tau) = -\left\langle v_i'(t_0 \mid \mathbf{x}, t_0) r_j'(t_0 - \tau \mid \mathbf{x}, t_0) \right\rangle_L = \int_{-\tau}^{0} P_{ij}(\mathbf{x}, \tau') d\tau'. \tag{10}$$

The four components are also frequently written in tensor notation:

$$\kappa(\mathbf{x}, \tau) \equiv \begin{bmatrix} \kappa_{11}(\mathbf{x}, \tau) & \kappa_{12}(\mathbf{x}, \tau) \\ \kappa_{21}(\mathbf{x}, \tau) & \kappa_{22}(\mathbf{x}, \tau) \end{bmatrix}. \tag{11}$$

Taylor (1921) showed that for homogeneous (location independent) and stationary (time independent) turbulence fields, the time lag dependence of $\kappa(\mathbf{x}, \tau)$ disappears eventually, as the diffusion becomes a random-walk (Colin de Verdiere, 1983), leaving

$$\kappa(\mathbf{x}, \tau) = \begin{bmatrix} \int_{-\tau}^{0} P_{11}(\mathbf{x}, \tau')d\tau' & \int_{-\tau}^{0} P_{12}(\mathbf{x}, \tau')d\tau' \\ \int_{-\tau}^{0} P_{21}(\mathbf{x}, \tau')d\tau' & \int_{-\tau}^{0} P_{22}(\mathbf{x}, \tau')d\tau' \end{bmatrix} = \begin{bmatrix} \kappa_{11}^{\infty} & \kappa_{12}^{\infty} \\ \kappa_{21}^{\infty} & \kappa_{22}^{\infty} \end{bmatrix} = \kappa^{\infty}, \tau \geq T, \tag{12}$$

where T represents the time at which the random walk begins. At time lags in excess of T, the diagonal elements of κ are simply the products of the respective velocity variances and integral time scales (Freeland et al., 1976). Equivalently,

$$T_i = \left[\left\langle v_i'(t_0 \mid \mathbf{x}, t_0)^2 \right\rangle_L \right]^{-1} \kappa_{ii}^{\infty}, \quad i = 1,2 \tag{13}$$

$$L_i = \left[\left\langle v_i'(t_0 \mid \mathbf{x}, t_0)^2 \right\rangle_L \right]^{-\frac{1}{2}} \kappa_{ii}^{\infty}, \quad i = 1,2 \tag{14}$$

give the Lagrangian time and length scales (Poulain et al., 1996) in terms of the steady-state diffusivity.

Our method for calculating the sample Lagrangian autocovariance function is presented in Appendix A, and is applied to each 5°x5° bin. We make the assumptions of homogeneity and stationarity in order to employ result (12) above. Homogeneity should clearly not be expected, however, in regions where the mean flow is significantly upset by dynamic or topographic effects. In our data, pronounced inhomogeneities occur mainly over the western basin, associated with the Gulf Stream and Northwest Corner. Lesser degrees of inhomogeneity are generally evident along the paths of the other continental boundary currents.

B. LAGRANGIAN RESULTS

Lagrangian time and length scales are calculated using equations 12 and 13, respectively, of section V.A. The required eddy diffusivities are computed by the method given in section V.B.4 below. Figures 33 through 36 show computed Lagrangian time scales (zonal and meridional) for the drifter data and "same starts" regimes. Results are shown for all bins having at least 250 observations. Figures 37 and 38 give the corresponding ratios of model time scale to drifter time scale, where results are shown for bins having at least 250 observations for both model and drifters. Figures 39 and 40 present frequency histograms of integral time scales for the drifters and both "same start" and

"random start" numerical trajectories. Figures 41 through 48 show the above plots for integral length scales.

1.   Integral Time Scales

A striking feature in all the time (and length) scale plots is the demarcation of the Gulf Stream. In the time scale plots, particularly those of the meridional component, it produces a swath of low values, with longer scales to the northwest and southeast. Beyond this effect, time scales tend generally to decrease with latitude, so that the highest are seen below the Gulf Stream. The model overestimates zonal time scales by factors up to 3.6 in the latitude band 20°N to 30°N and by up to 4.9 north of the Gulf Stream and its extension. Outside these regions, zonal time scales are in fairly good agreement, as shown by the ratio plot of Figure 37.

Meridional time scales are also exaggerated north of the Gulf Stream, (by up to 5.6 times). There is also overestimation in the 20°N to 30°N band, but only in the eastern basin, by up to a factor of 3.3. The meridional ratio plot reflects the broader extent of values near unity, particularly distinct over the North American Basin.

"Random start" (not shown) and "same start" time scales appear to match fairly closely in magnitude and spatial distribution. The histograms of Figures 39 and 40 show similar frequency distributions as well. For the zonal direction, both regimes show distributions with most time

scales between four to nine days and long, relatively uniform tails out to 15 days. Neither shows time scales below about two days. In contrast, the drifter histogram indicates a significant number of those low values, and none greater than eight days. For the meridional direction, most model time scales fall in the 2 - 6 day range while higher values occur out to ten and twelve days for the "same start" and "random start" schemes, respectively. The drifter histogram again shows a large number of occurrences below two days, none greater than about eight days, and most scales in the one to five day range. Clearly, the model inflates integral time scales on the whole, with the effect most pronounced in the zonal direction.

Figure 33. Lagrangian integral time scale (days), zonal component, drifters. The time domain is January 1, 1993 to December 31, 1997. Bins with fewer than 250 daily observations contain no information and are in white.

91

Figure 34. Lagrangian integral time scale (days), zonal
component, "same start" simulation. The time domain is
January 1, 1993 to December 31, 1997. Bins with fewer than
250 daily observations contain no information and are in
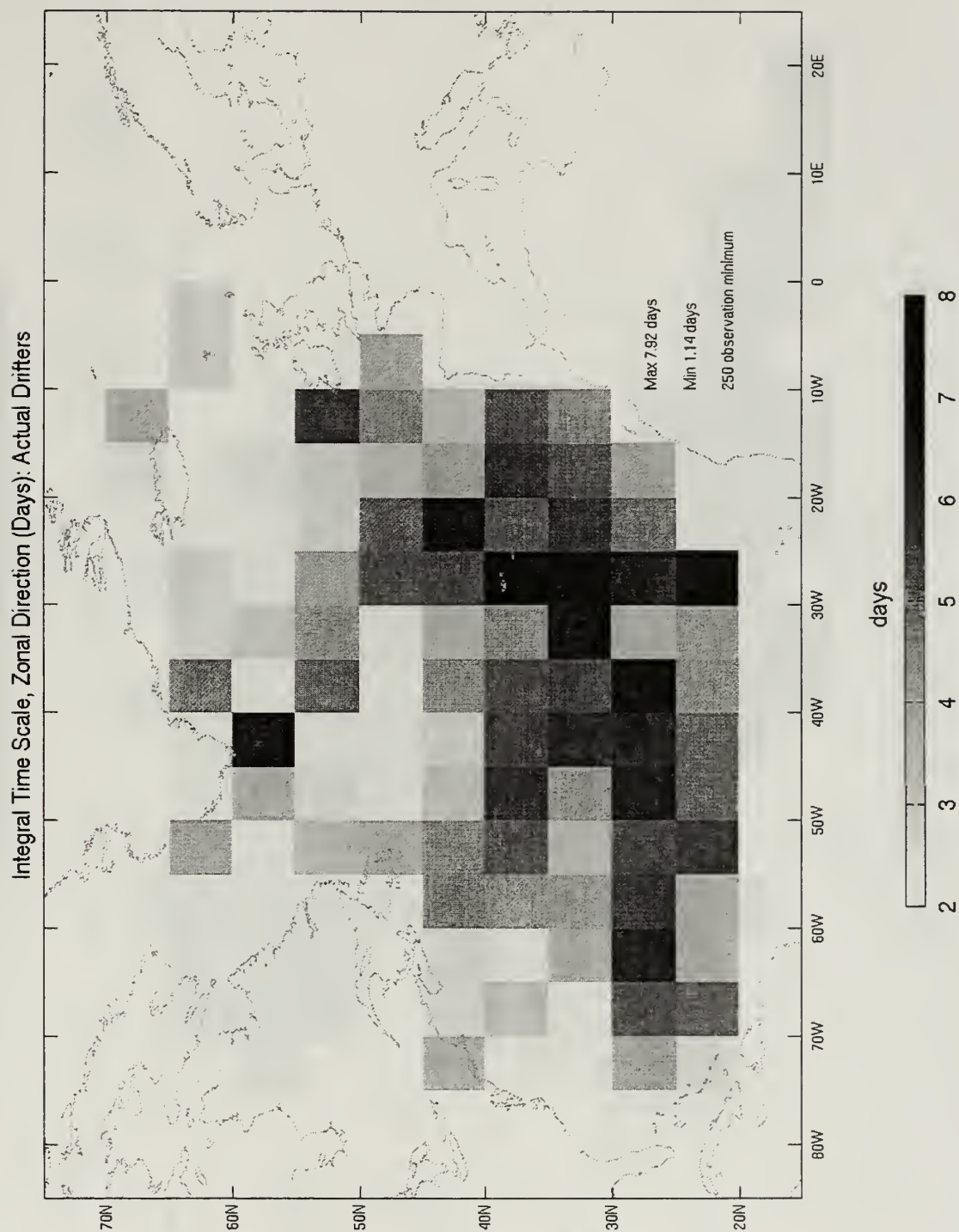white.

92

Figure 35. Lagrangian integral time scale (days), meridional
component, drifters. The time domain is January 1, 1993 to
December 31, 1997. Bins with fewer than 250 daily
observations contain no information and are in white.

93
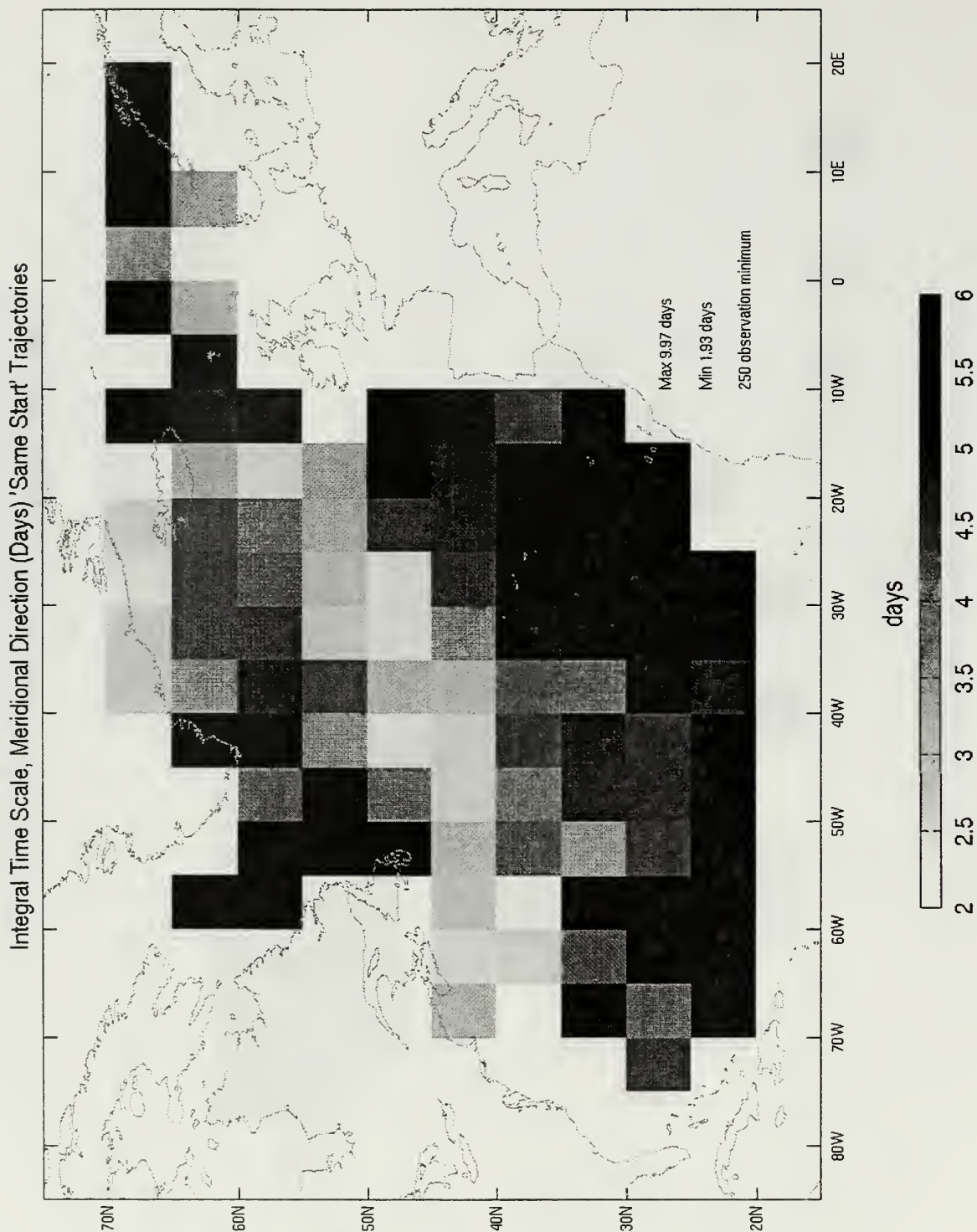
Figure 36. Lagrangian integral time scale (days), meridional component, "same start" simulation. The time domain is January 1, 1993 to December 31, 1997. Bins with fewer than 250 daily observations contain no information and are in white.
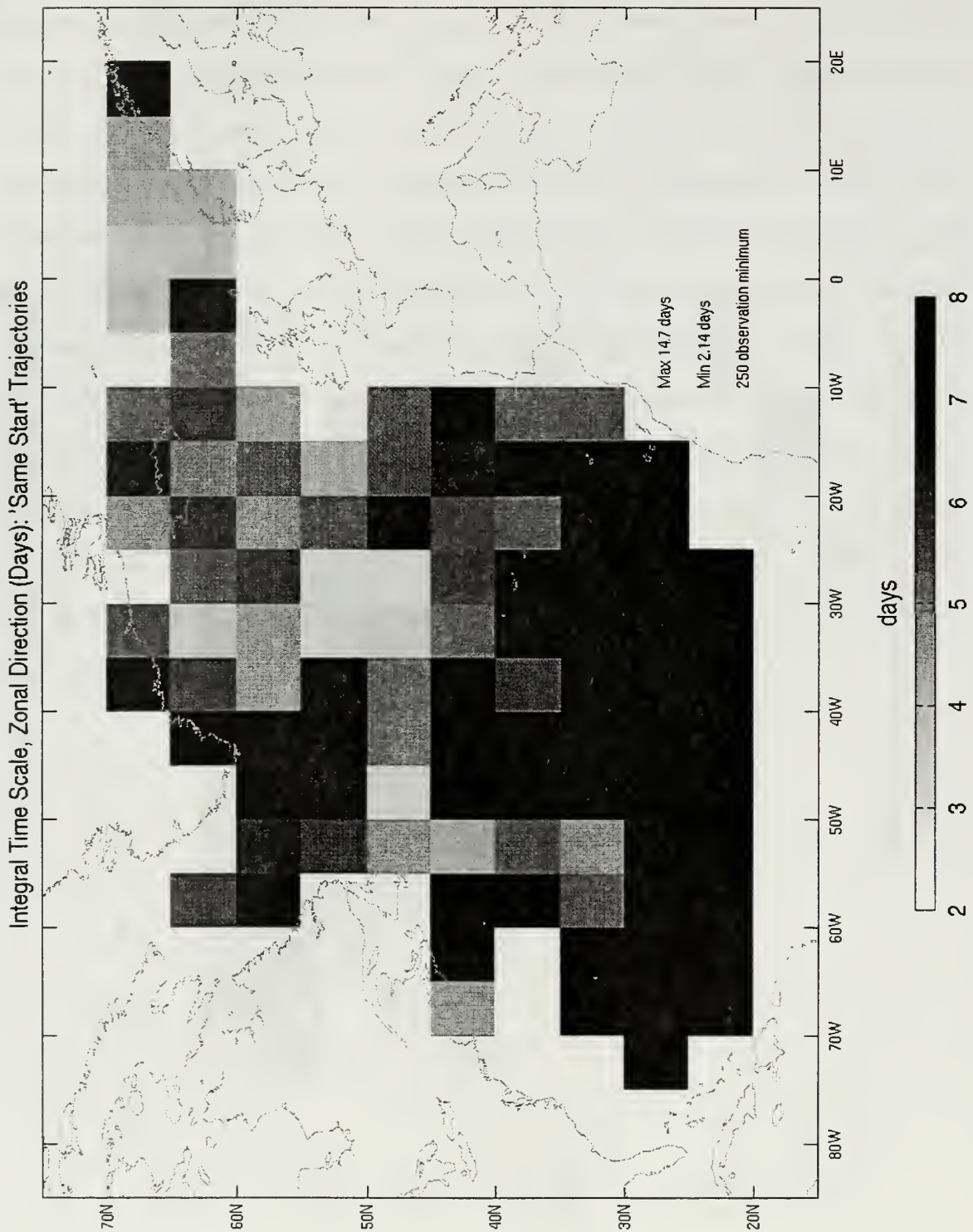
94
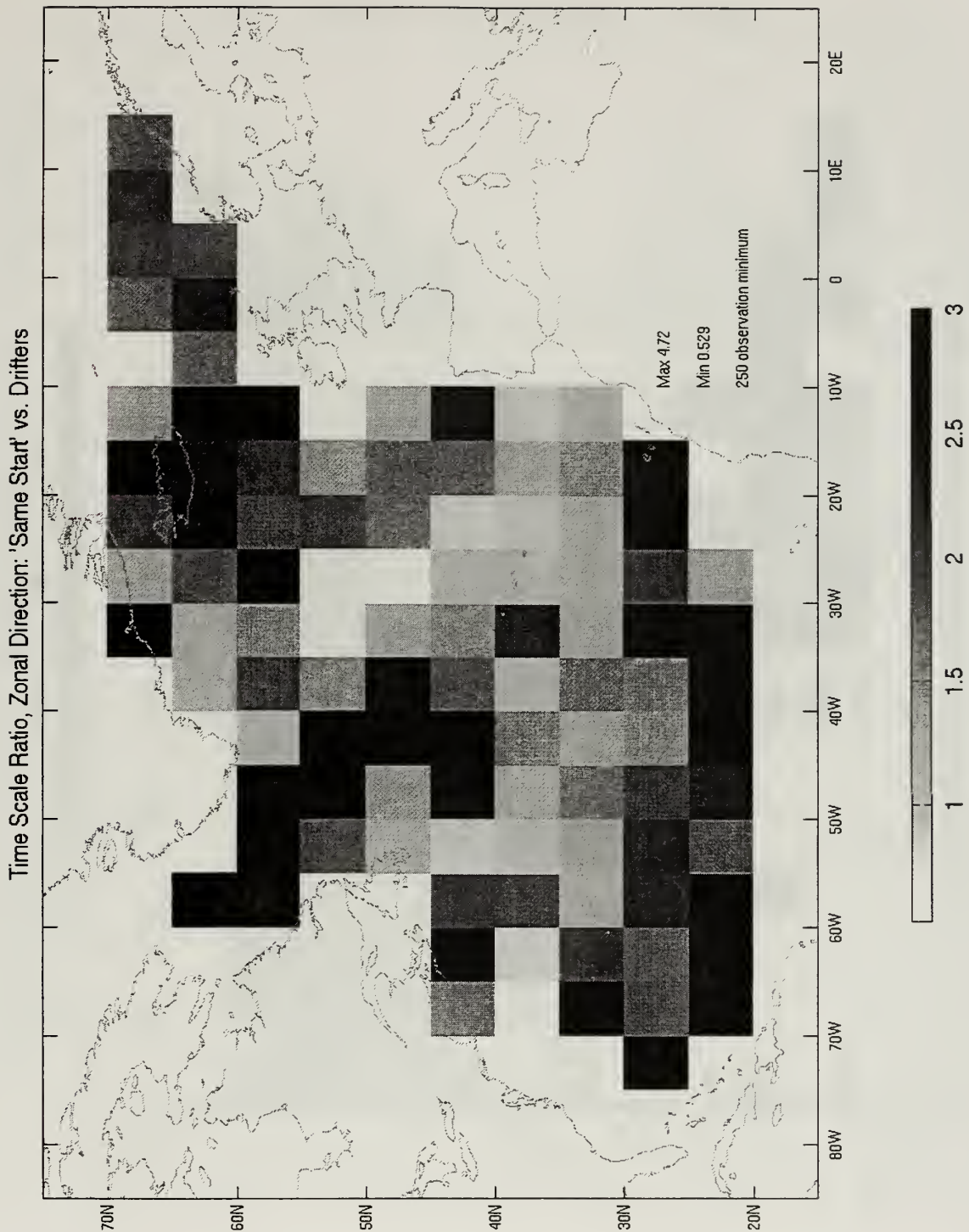
Figure 37. Ratio of "same start" Lagrangian integral time scale to drifter integral time scale, zonal direction. The time domain is January 1, 1993 to December 31, 1997. Bins with fewer than 250 daily observations for either real or simulated trajectories contain no information and are in white.
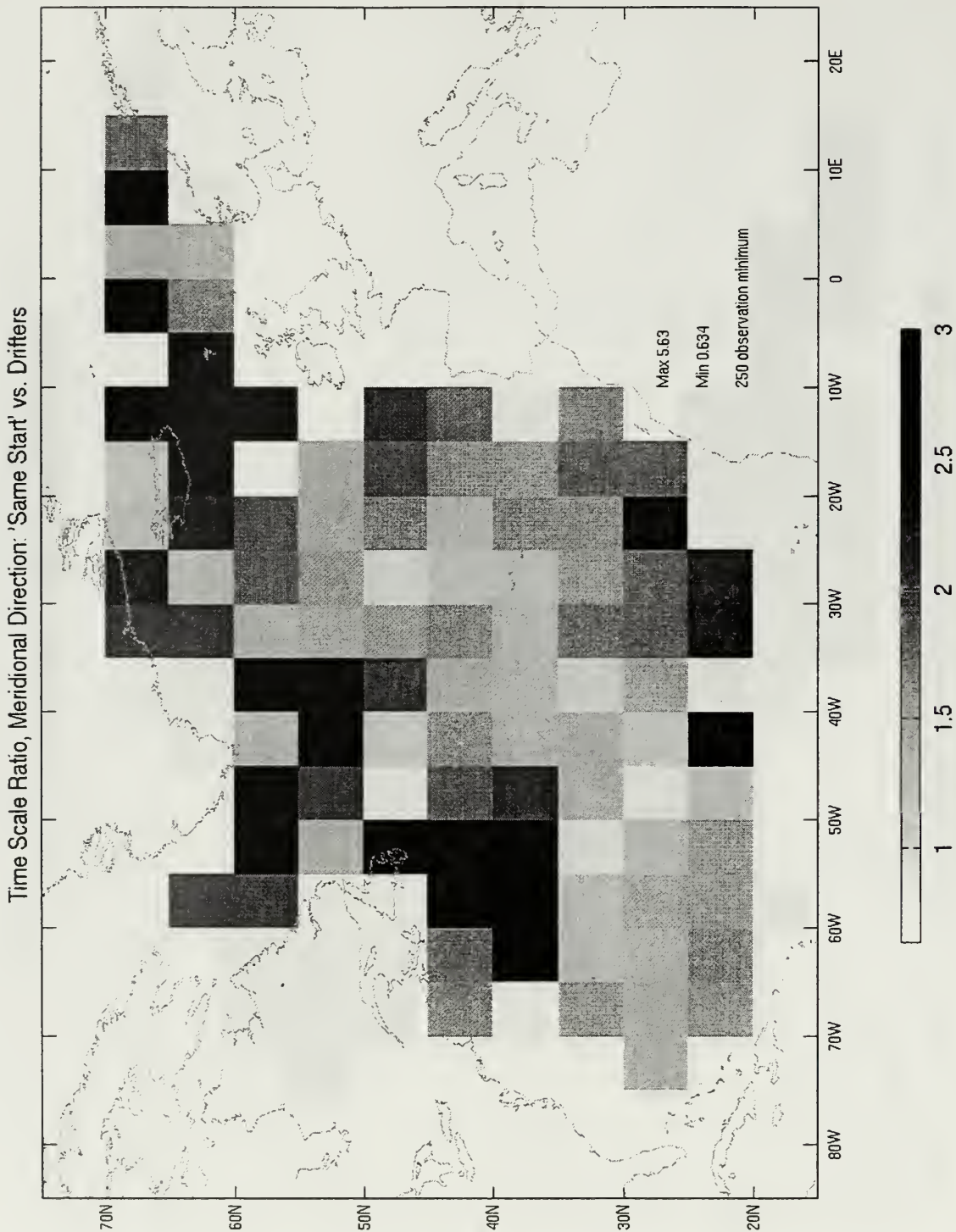
Figure 38. Ratio of "same start" Lagrangian integral time scale to drifter integral time scale, meridional direction. The time domain is January 1, 1993 to December 31,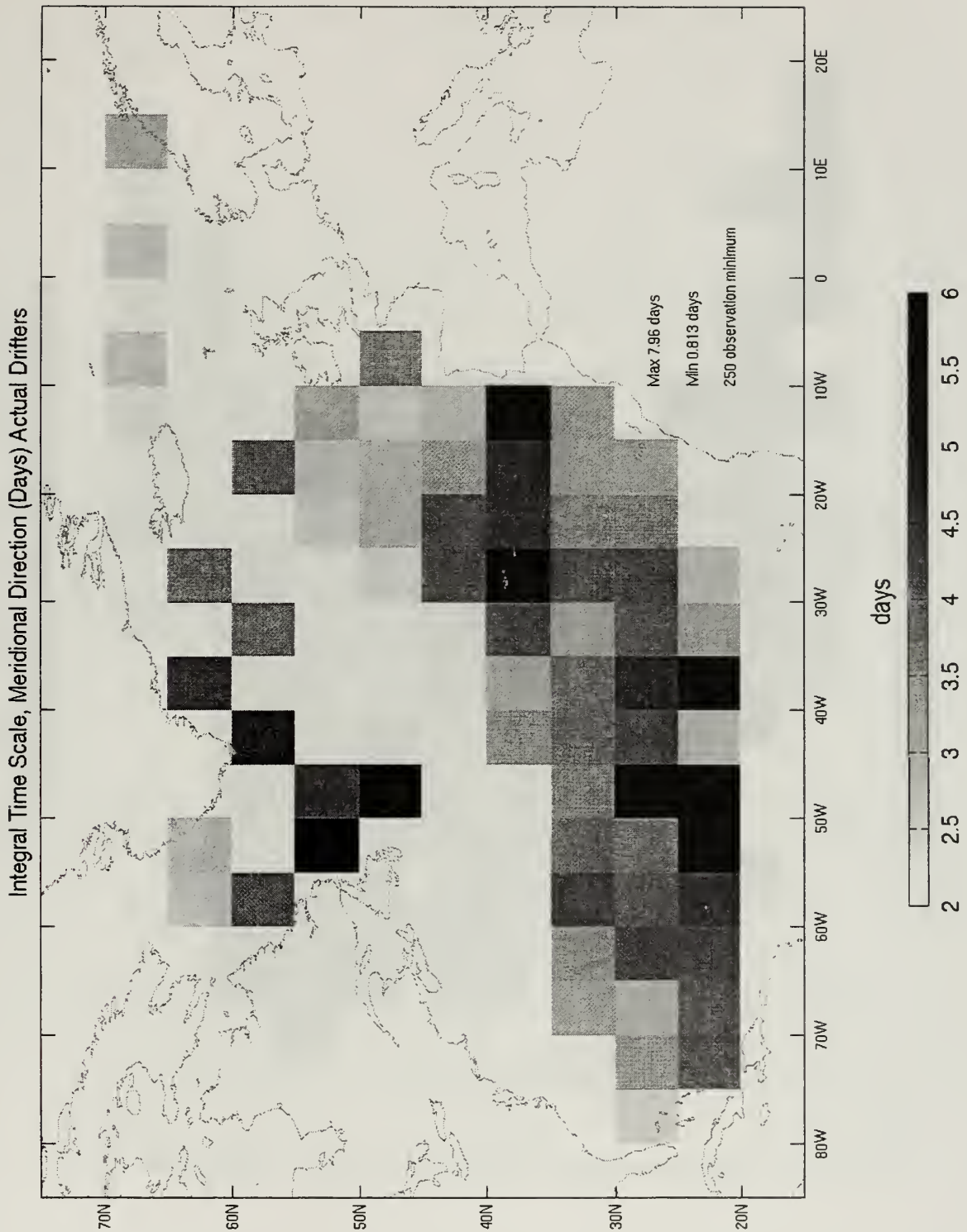 1997. Bins with fewer than 250 daily observations for either real or simulated trajectories contain no information and are in white.
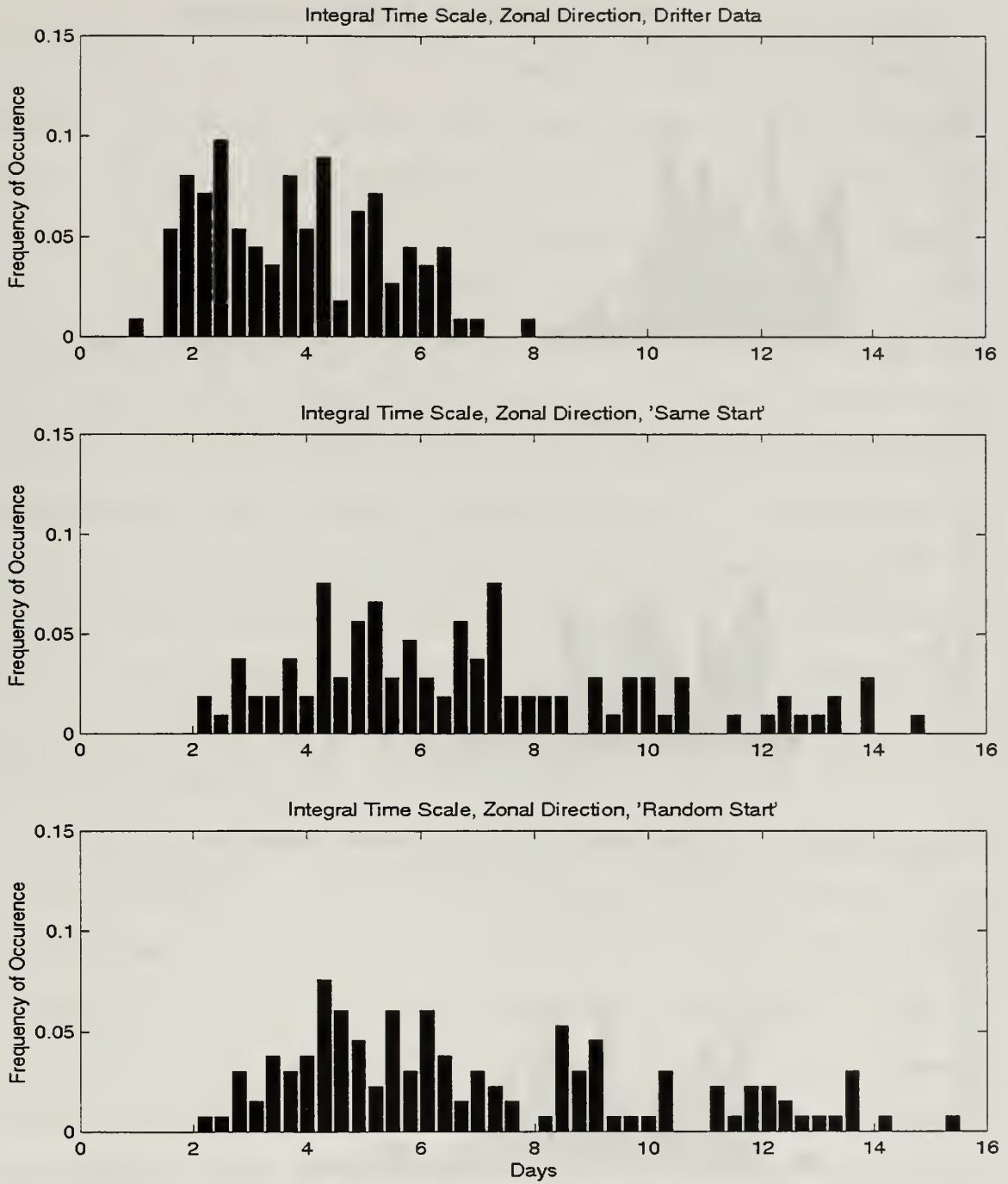
Figure 39. Histograms of Lagrangian integral time scales (days) for drifter, "same start", and "random start" trajectories, zonal component. The time domain is January 1, 1993 to December 31, 1997. Bins with fewer than 250 daily observations for either real or simulated trajectories are not represented.

Figure 40. Histograms of Lagrangian integral time scales (days) for drifter, "same start", and "random start" trajectories, meridional component. The time domain is January 1, 1993 to December 31, 1997. Bins with fewer than 250 daily observations for either real or simulated trajectories are not represented.
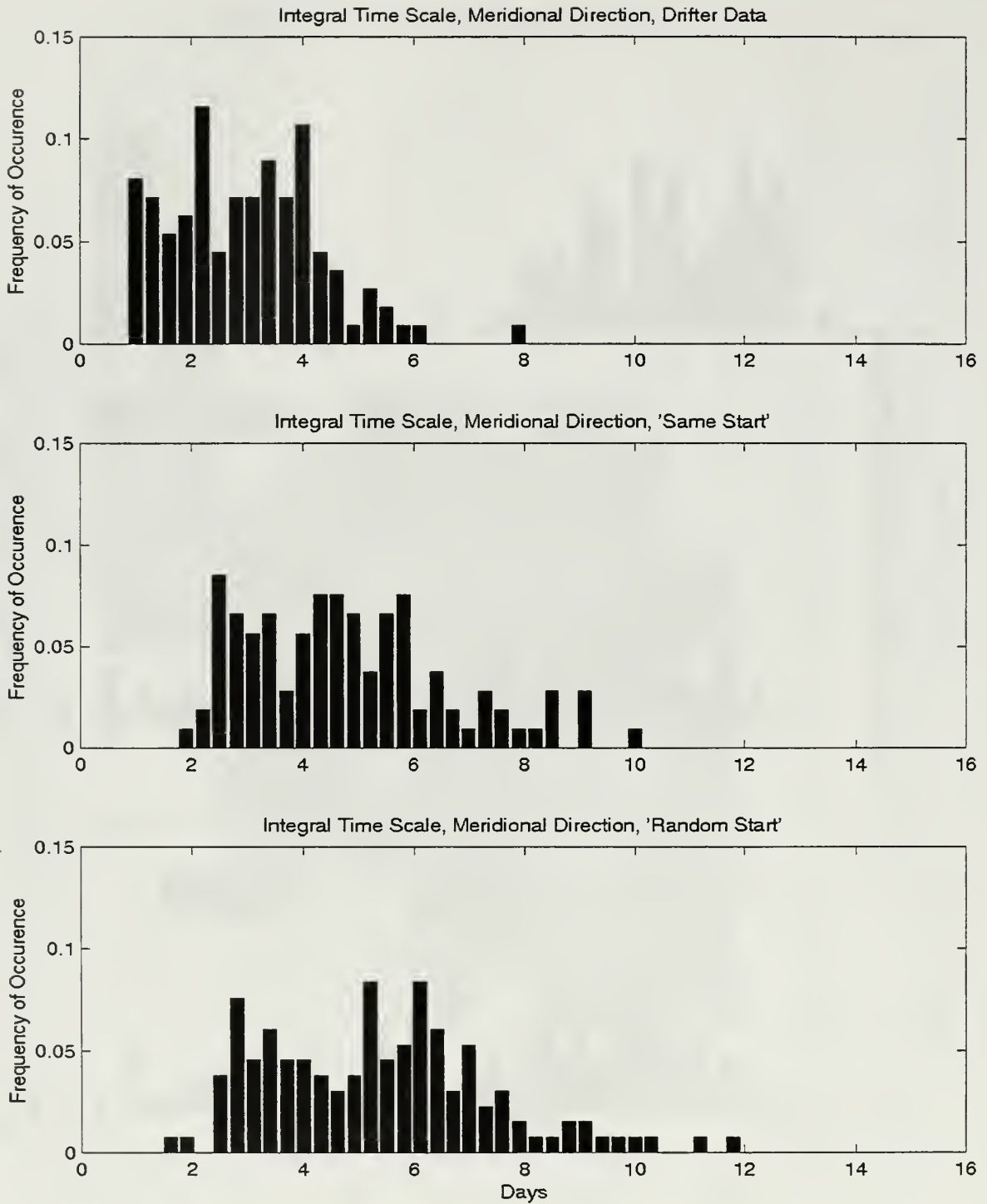
2. Integral Length Scales

There is much better agreement in magnitude between the model's integral length scales and those of the drifters. The ratio of model length scale to drifter length scale ranges from 0.3 to 2.9 in the zonal direction and from 0.3 to 5.4 in the meridional direction, but a far greater number of bins show values close to unity than for the time scales. The ratio plots show overestimation of zonal length scales occurring mainly south of 30°N and north of 50°N, with the intervening band showing underestimation. The pattern of ratios in the meridional direction is similar to that of the time scales, with elevated values north of the Gulf Stream and in the southeast Subtropical Gyre. The exaggeration is more pronounced in the northern zone, while underestimation is most evident in the lower western basin.

Again, "random start" (not shown) and "same start" length scales show similar spatial distributions and magnitudes. The histograms for the two trajectory schemes (figs. 47, 48) show a good degree of similarity, and are close in shape to those of the drifters. The zonal length scale histograms show longer tails for the drifters, extending to 165 km compared to 134 km for the "same start" simulation. The number of occurrences below 20 km is about four times higher for the drifters than for the "same start" regime. For all three histograms, most length scales are contained between 15 and 60 km. The degree of agreement for the meridional histograms is even better. In all three

nearly all length scales fall between 10 and 60 km; the tail behavior is almost identical, with extreme values reaching about 100 km. The only significant differences are skews in the model histograms not seen in the drifter plot, and distribution differences in the range 50 – 65 km.
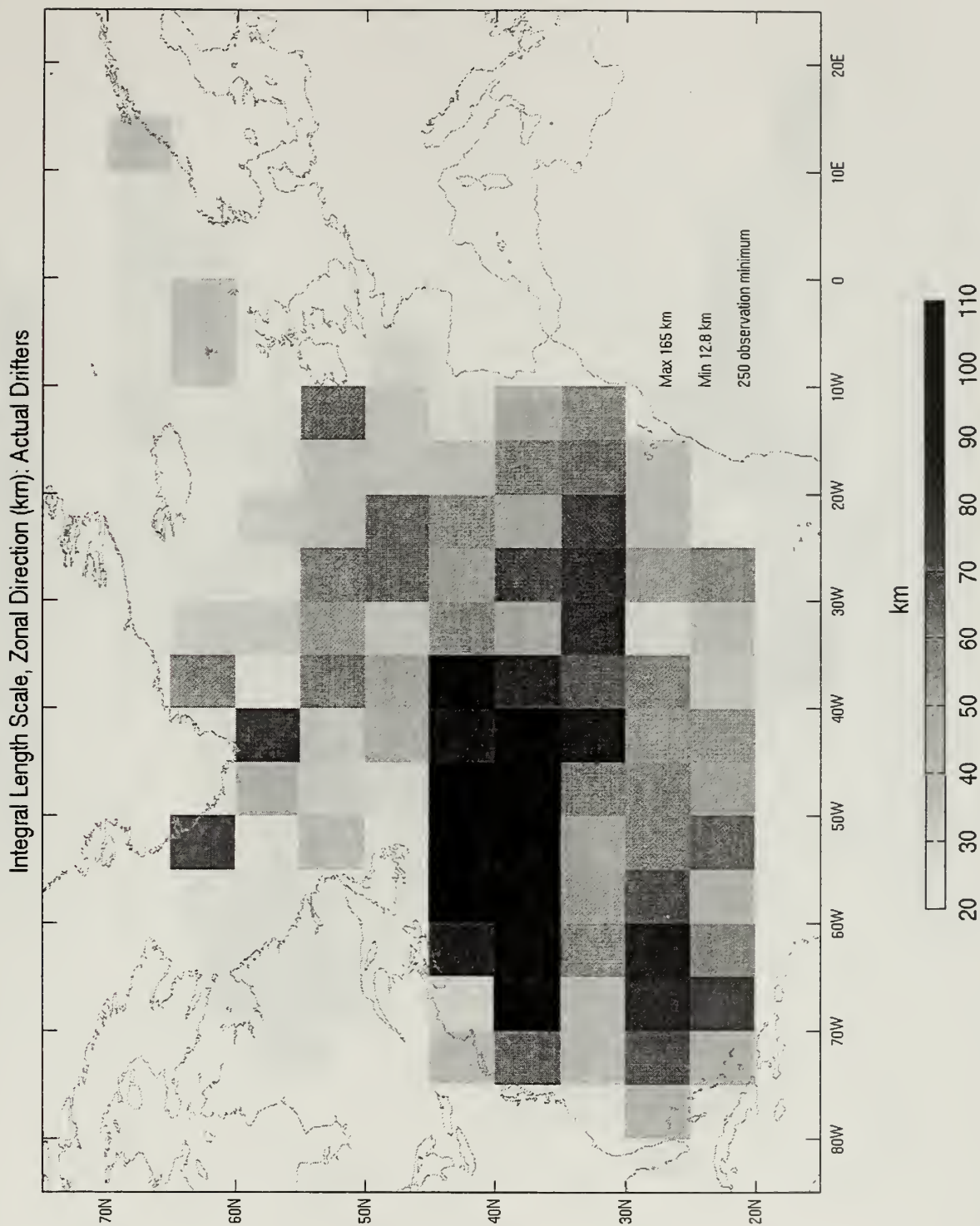
Figure 41. Lagrangian integral length scale (km), zonal component, drifters. The time domain is January 1, 1993 to December 31, 1997. Bins with fewer than 250 daily observations contain no information and are in white.
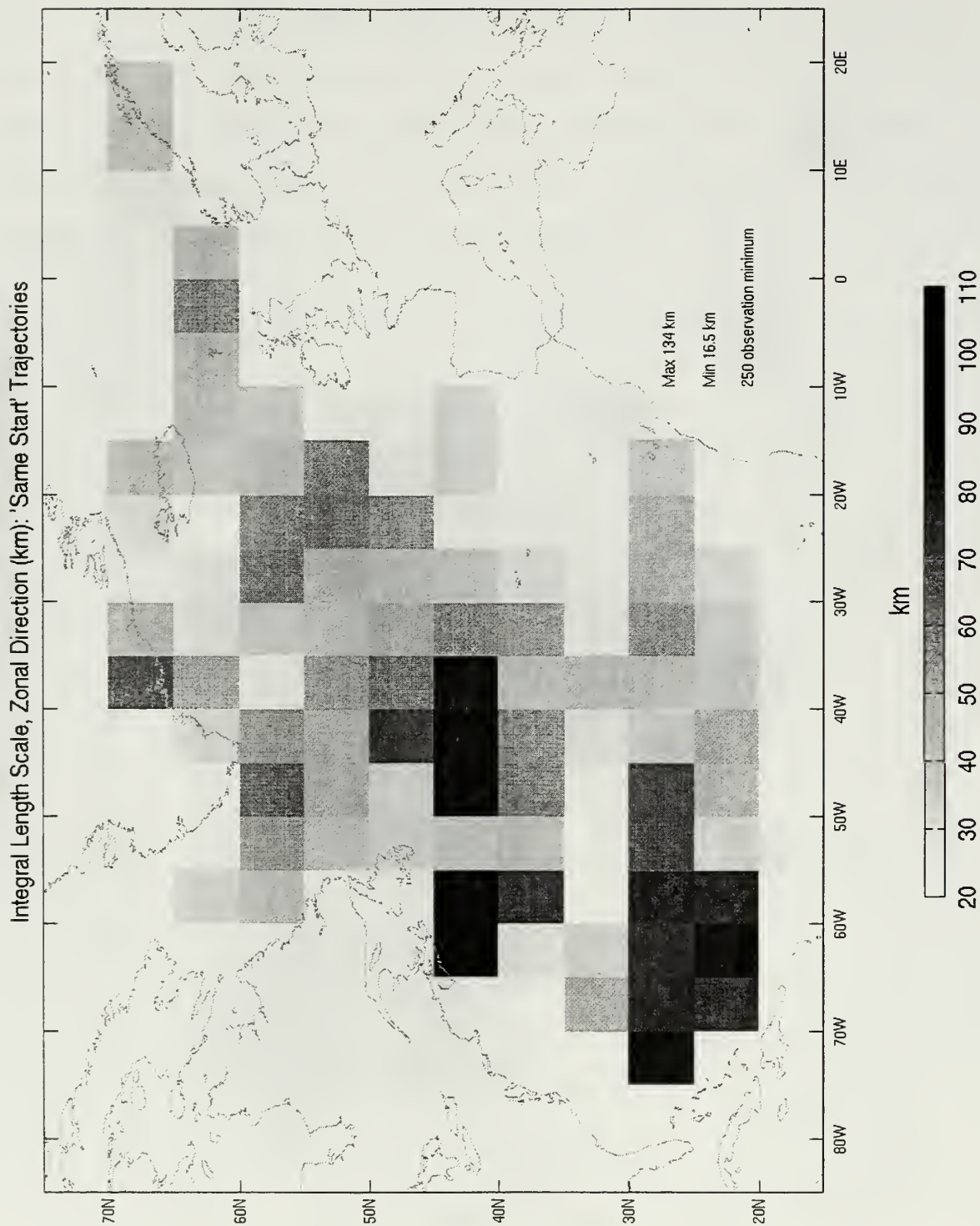
Figure 42. Lagrangian integral length scale (km), zonal
component, "same start" simulation. The time domain is
January 1, 1993 to December 31, 1997. Bins with fewer than
250 daily observations contain no information and are in
white.
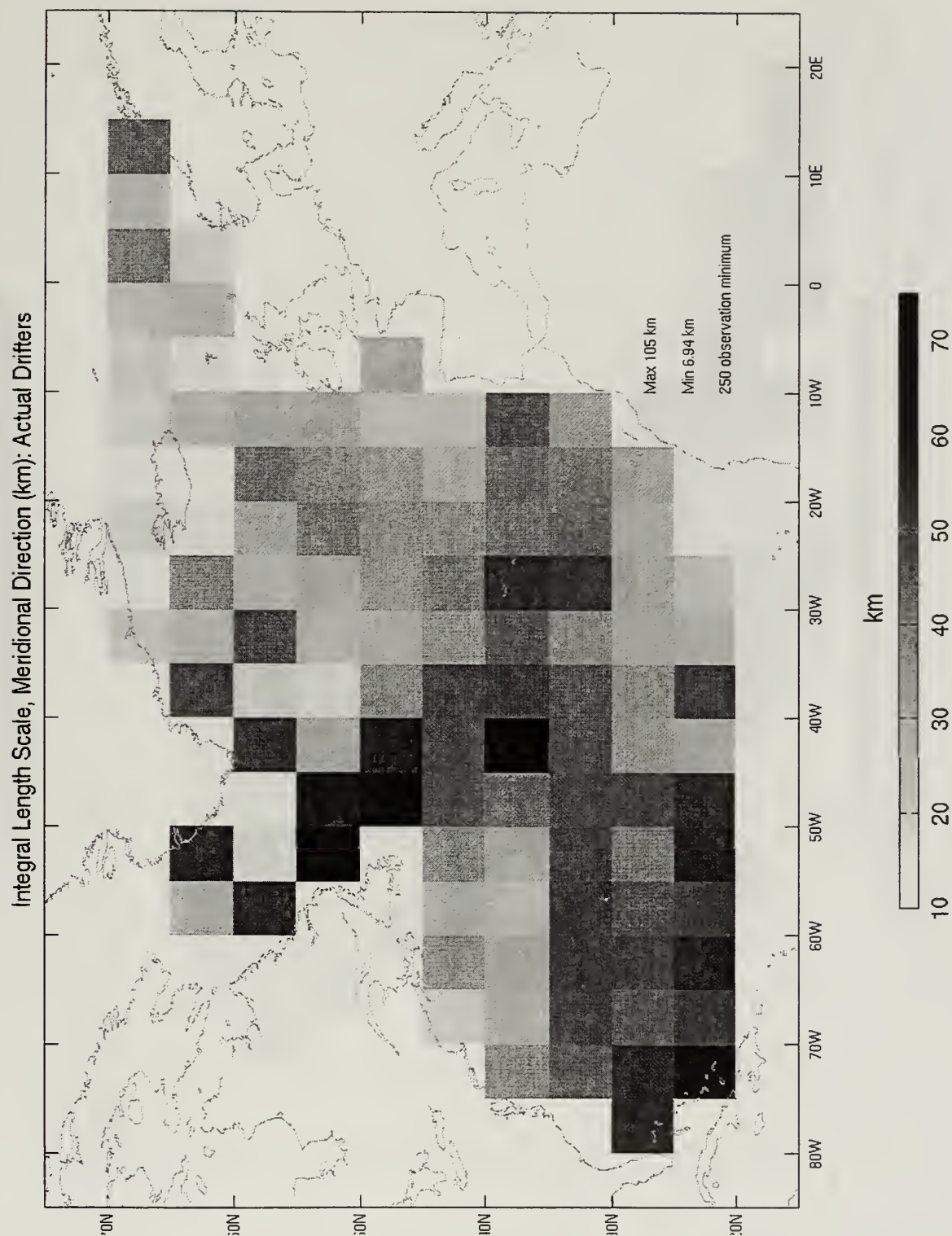
Figure 43. Lagrangian integral length scale (km), meridional component, drifters. The time domain is January 1, 1993 to December 31, 1997. Bins with fewer than 250 daily observations contain no information and are in white.

103
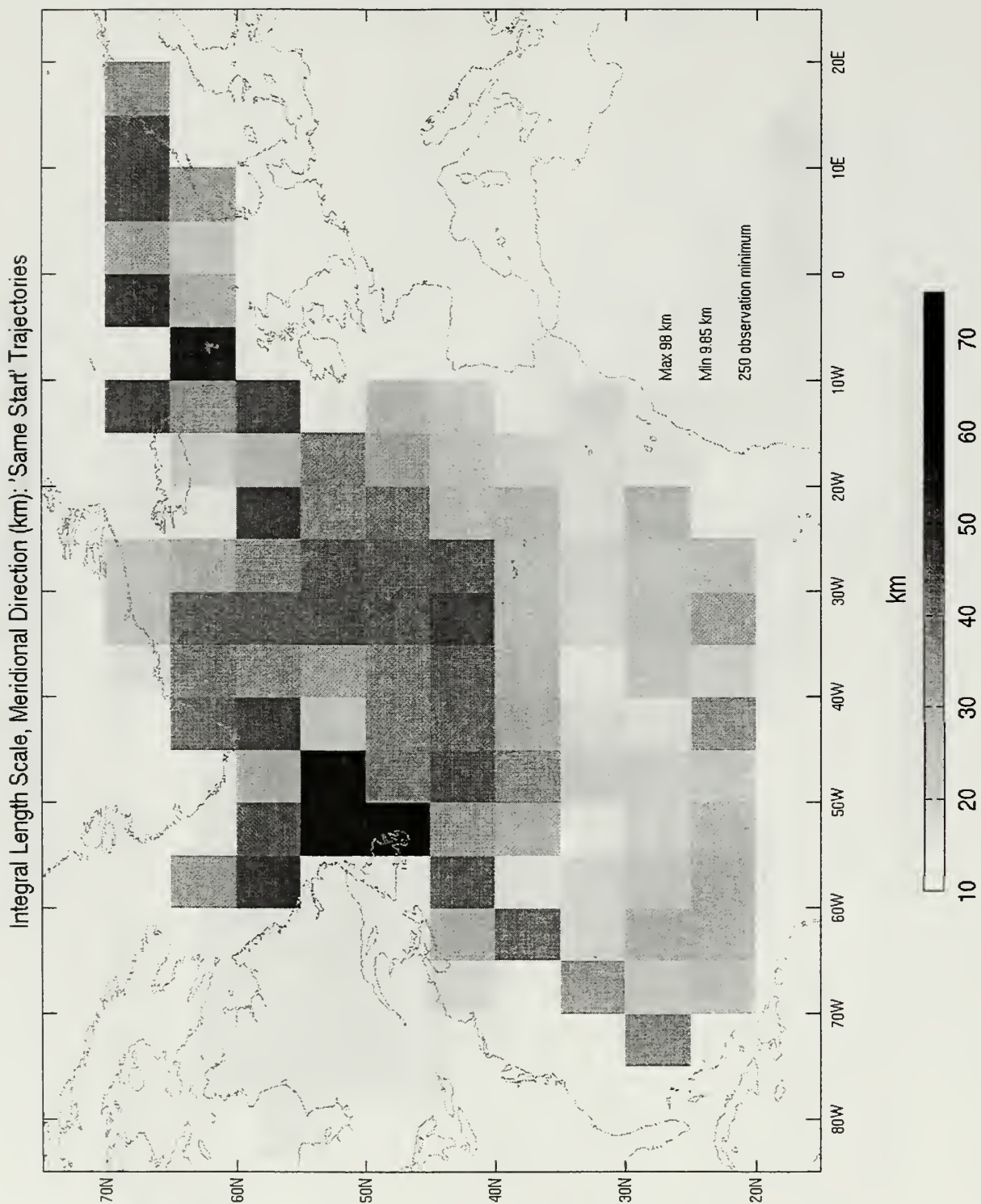
Figure 44. Lagrangian integral length scale (km), meridional component, "same start" simulation. The time domain is January 1, 1993 to December 31, 1997. Bins with fewer than 250 daily observations contain no information and are in white.
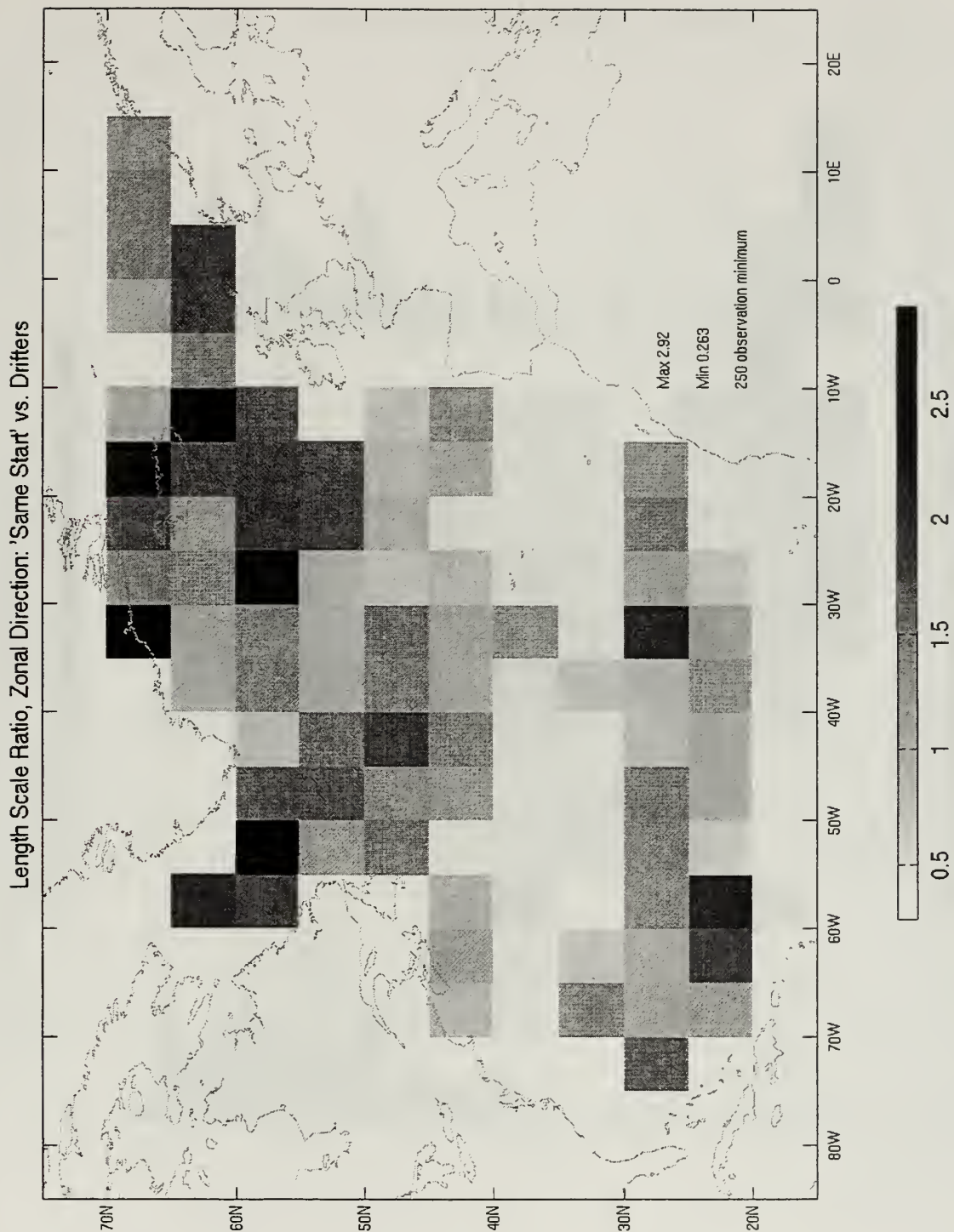
Figure 45. Ratio of "same start" Lagrangian integral length scale to drifter integral length scale, zonal direction. The time domain is January 1, 1993 to December 31, 1997. Bins with fewer than 250 daily observations for either real or simulated trajectories contain no information and are in white.
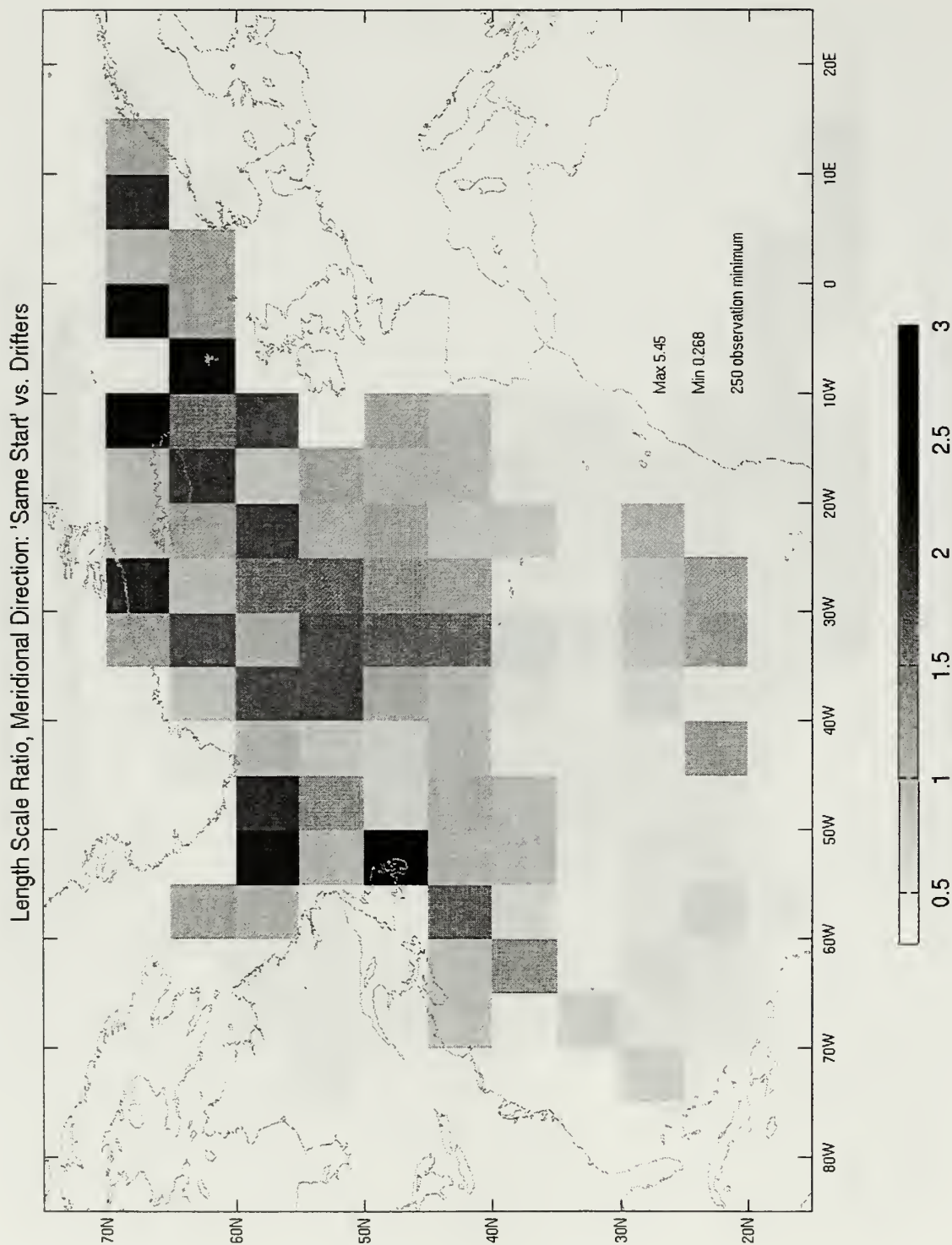
Figure 46. Ratio of "same start" Lagrangian integral length scale to drifter integral length scale, meridional direction. The time domain is January 1, 1993 to December 31, 1997. Bins with fewer than 250 daily observations for either real or simulated trajectories contain no information and are in white.
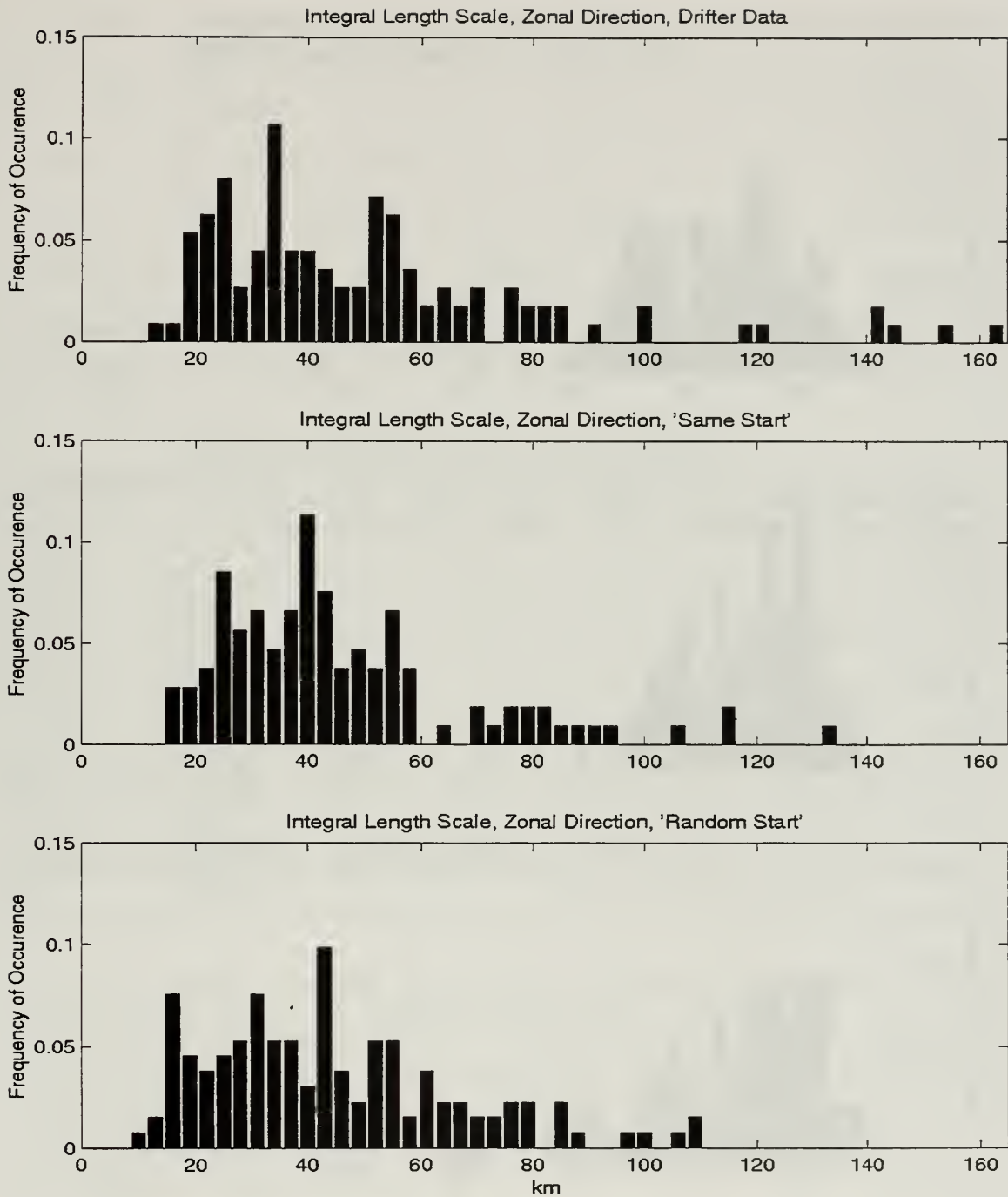
Figure 47. Histograms of Lagrangian integral length scales (km) for drifter, "same start", and "random start" trajectories, zonal component. The time domain is January 1, 1993 to December 31, 1997. Bins with fewer than 250 daily observations for either real or simulated trajectories are not represented.

107
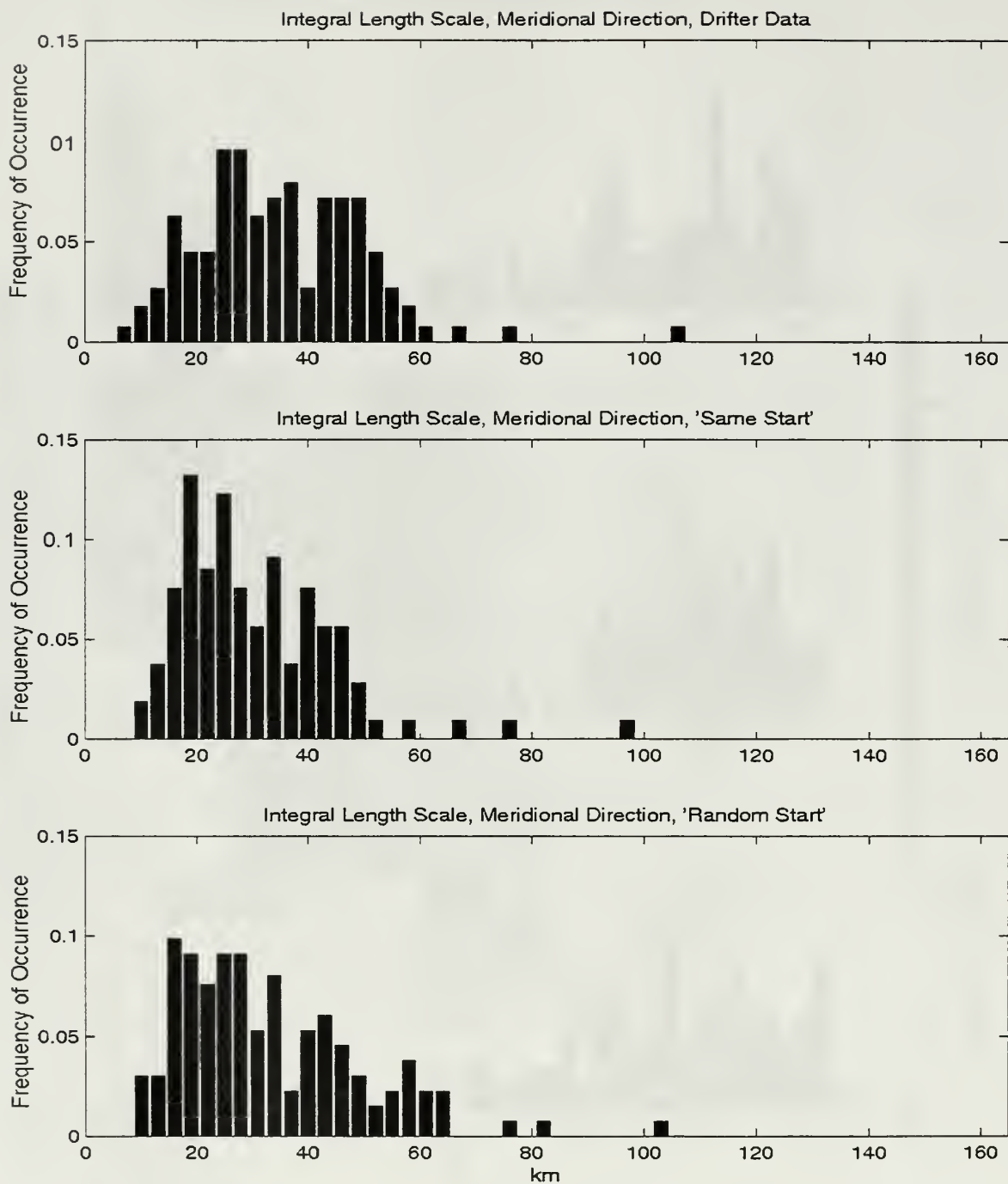
Figure 48. Histograms of Lagrangian integral length scales (km) for drifter, "same start", and "random start" trajectories, meridional component. The time domain is January 1, 1993 to December 31, 1997. Bins with fewer than 250 daily observations for either real or simulated trajectories are not represented.

108

3. Comparison of Integral Time and Length Scales with Previous Studies

The integral time scales computed from the drifter data compare well with a previous large-area study by Krauss and Böning (1987), those from corresponding areas agreeing generally within 1 day. Integral length scales show less agreement. The exact values are given in the table below:

LONGITUDE	LATITUDE	ITSZ K&B	ITSZ WOCE	ITSM K&B	ITSM WOCE	ILSZ K&B	ILSZ WOCE	ILSM K&B	ILSM WOCE
30°N-33°N	16°W-27°W	4.5	4.6	5.6	2.9	32	49	40	29
39°N-43°N	22.5°W-29°W	8.6	6.3	5.7	5.8	80	53	53	50
45°N-47.5°N	20°W-28.5°W	6.0	6.2	3.4	2.7	72	72	41	33
39°N-43.5°N	38.5°W-43.5°W	3.0	3.0	2.3	1.5	53	85	42	40
43°N-47°N	32.5°W-41.5°W	2.8	2.4	3.2	1.7	56	54	66	35
47°N-52.5°N	31.5°W-43.5°W	2.1	1.8	2.1	1.6	45	36	47	34
48.5°N-52.5°N	20°W-30.5°W	3.2	4.5	2.2	2.5	59	63	37	33
53°N-55°N	30°W-37.5°W	4.3	4.3	3.4	2.4	58	36	46	21

Table 1. Comparison of Lagrangian integral time and length scales with those of Krauss and Böning (1987). Abbreviations used are ITSZ (integral time scale, zonal), ITSM (integral time scale, meridional), ILSZ (integral length scale, zonal), ILSM (integral length scale, meridional), K&B (Krauss and Böning), WOCE (World Ocean Circulation Experiment (with which the drifter data collection is associated)).

Time and length scales are found by Colin de Verdière (1983) in the Bay of Biscay to be 2.5 days and 22.3 km for the zonal direction, and 2 days and 17.1 km for the meridional direction. For roughly the same region we obtain

4.3 days and 32.1 km for the zonal direction and 2.6 days and 21.5 km for the meridional direction. Again, the time scales show better agreement than the length scales.

4. Eddy Diffusivities

To estimate eddy diffusivities, we take the maximum values attained by the integrals of the Lagrangian autocovariance functions (see Appendix A) over the time domain 0 - 25 days. This is a reasonable simplification, and for an ensemble of particles released simultaneously from one point into a perfectly homogeneous, stationary turbulence field, yields a value similar to the theoretical result, given that the integral time scale is generally much smaller than 25 days.

The limitations of the method should be made clear, however. The assumption of homogeneity is unrealistic in some locations, as stated previously. Strong inter-annual and intra-annual effects in the velocity field violate the stationarity assumption. Such departures from the ideal state lead to autocovariance functions that do not asymtote smoothly to zero; the resulting eddy diffusivities may have significant oscillations that complicate specifying a representative value.

Difficulties in quantifying eddy diffusivity are exacerbated by large time lags. Even if a particle begins its path in a locally homogeneous and stationary field, its track, on which the diffusivity calculation is based, may

lead into a region of significantly different properties over the time lag of interest. Further, actual computations of eddy diffusivity based on field data cannot meet the requirement of simultaneous particle release from one point. The point of release must be approximated by a two-dimensional region; the tracks falling into that area are then used to compute an average Lagrangian autocovariance function, which is then integrated to obtain the diffusivity. This highlights another difficulty with large time lags. Because drifter tracks are finite, the number of contributions to the average autocovariance function decreases with increasing time lag as more track terminations occur.

In regions where velocities have high temporal autocorrelation, the integrals will continue to increase up to large time lags. This forces a compromise: one must either cite a diffusivity that clearly underestimates the steady-state value, or else incur the errors discussed above in pursuing higher time lags. Examples of such behavior in the drifter data include the Gulf Stream, for which there is strong zonal-zonal autocorrelation out to 25 days, and north of 50°N and west of 45°W, where both diagonal components $(\kappa_{11}(\tau), \kappa_{22}(\tau))$ of diffusivity indicate persistent autocorrelation. The model shows the same tendencies in these areas; additionally, for most of the band 20°N to

30N°, $\kappa_{11}(\tau)$ shows no sign of reaching a plateau over 25 days. The effect is most pronounced in the west basin.

The above discussion illustrates the difficulty in choosing a practical rule for determining eddy diffusivity values. While our taking a simple maximum value over a fixed time domain may seem naïve, it should give accurate results in "well-behaved" regions. Where the diffusivities fail to plateau, the estimates must be interpreted as lower bounds. In more ill-behaved areas the use of more complex methods based on asymptotic diffusion theory seems questionable, given the departure from either homogeneity, stationarity, or both.

Figures 49 and 50 display the integrals of the sample Lagrangian velocity autocovariance functions from four distinctive regions of the North Atlantic, for the drifter data and "same start" trajectories. Only zonal-zonal and meridional-meridional components are shown. The characteristics of the regions are as follows:

Region 1 (55°N-60°N, 35°W-40°W): This region is located southeast of the cusp of Greenland. It is representative of latitudes north of 55°N, where diffusivity magnitudes are generally within 5×10^7 cm^2/sec, plateaus are reached within 25 days in most cases, inhomogeneities are not pronounced, and where there is generally good agreement between diffusivity curves from the drifters and from the "same starts" trajectories.

Figure 49. Integrals of zonal and meridional components of
the sample Lagrangian velocity autocovariance functions
(calculated per Appendix A) for regions 1 and 2. The
diagonal components of eddy diffusivity, on which the
Lagrangian integral time and length scales are based
(equations 13,14), are taken as the maxima of the
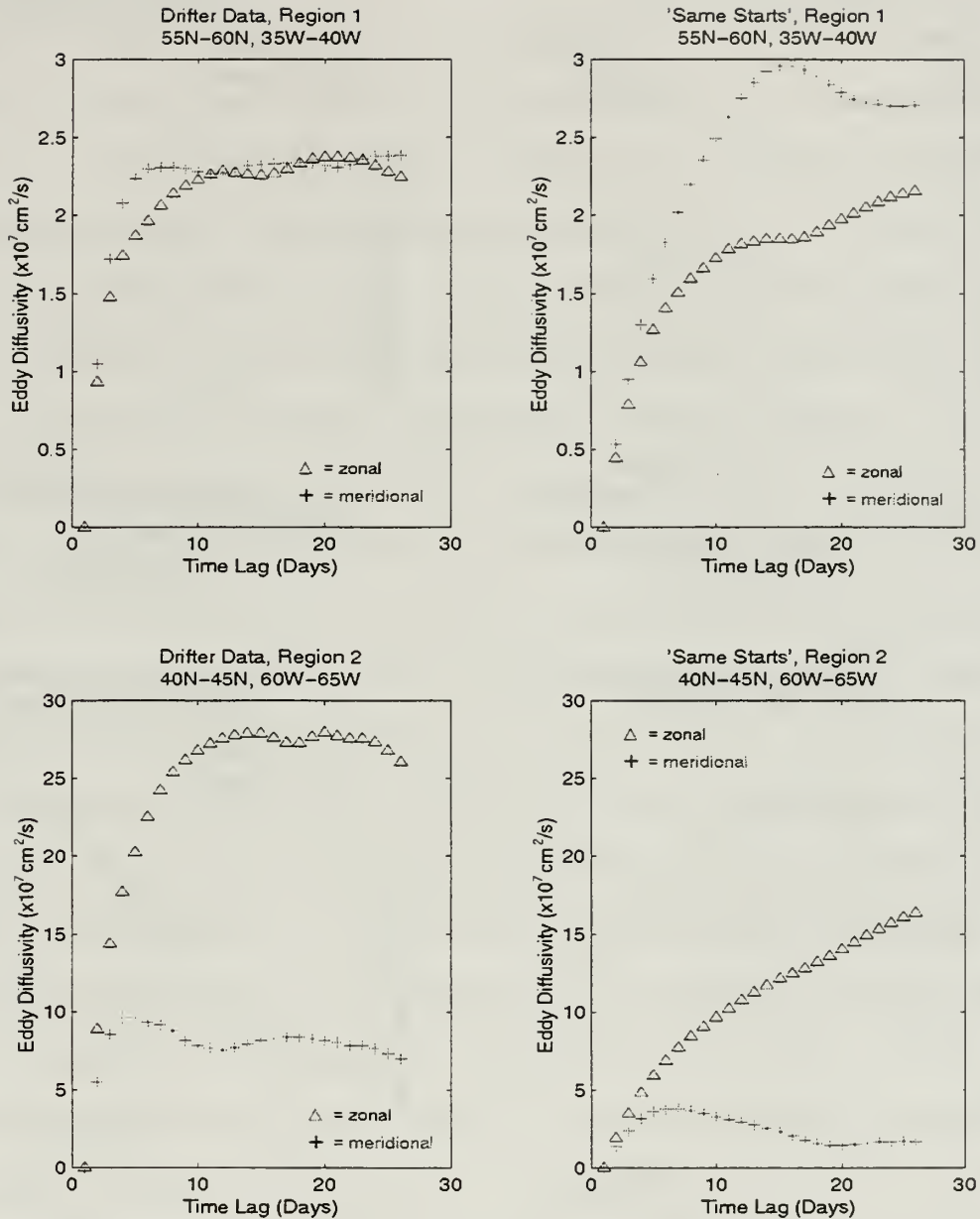corresponding integrals over 25 days.
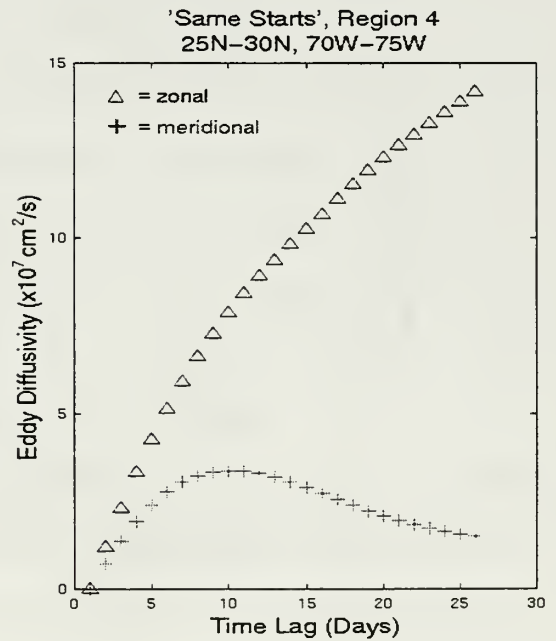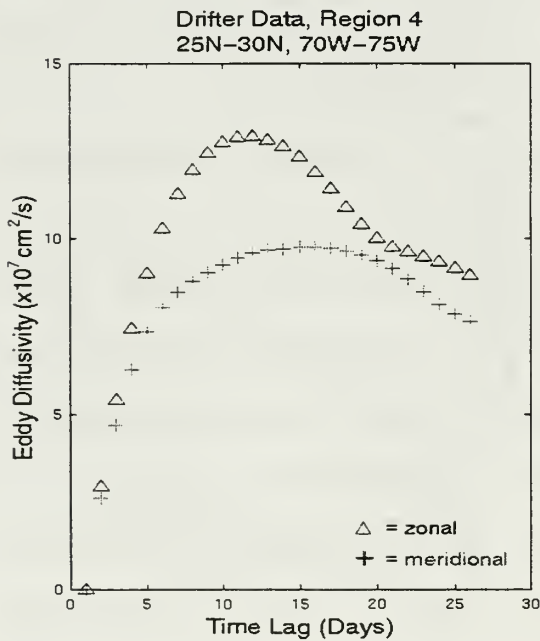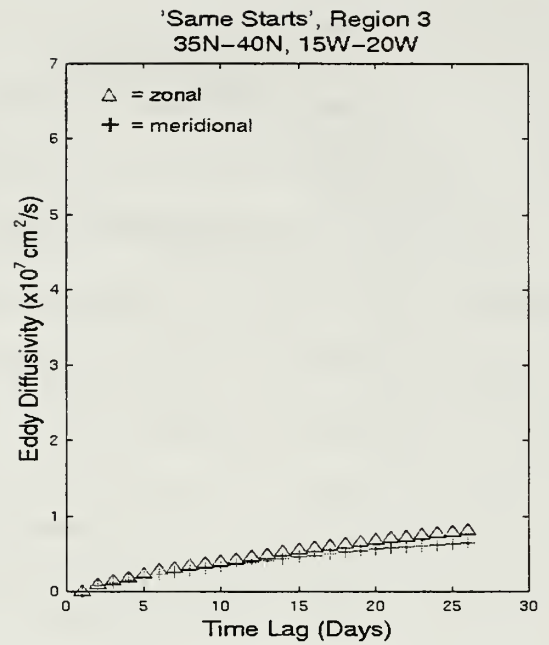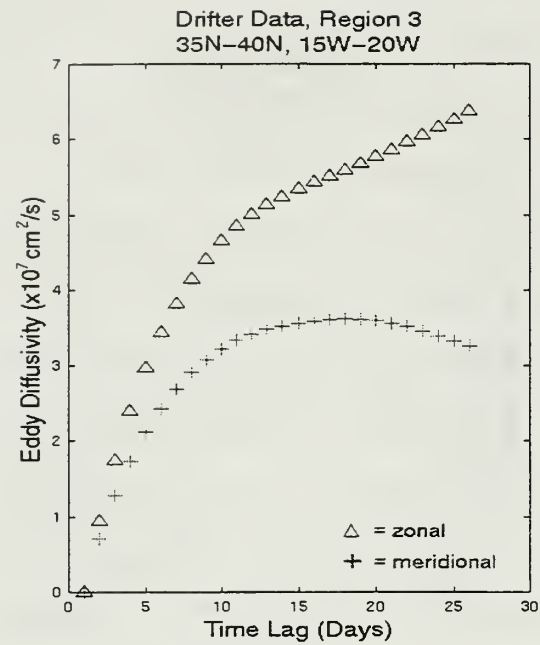
Figure 50. Integrals of zonal and meridional components of the sample Lagrangian velocity autocovariance functions (calculated per Appendix A) for regions 3 and 4. The diagonal components of eddy diffusivity, on which the Lagrangian integral time and length scales are based (equations 13,14), are taken as the maxima of the corresponding integrals over 25 days.

114

Region 2 (40°N-45°N, 60°W-65°W): This box is to the south of Nova Scotia, in the path of the Gulf Stream. It characterizes the western North Atlantic between latitudes 35°N and 45°N. This entire region is under direct Gulf Stream influence. Inhomogeneities are evident in most of the drifter diffusivity plots. Zonal diffusivity magnitudes are significantly larger than meridional values, and quite large in an absolute sense (exceeding 5x108 cm2/sec for the drifters). In about half the cases, for both drifters and model, zonal diffusivities do not plateau within 25 days. Model diffusivities are smaller than those of the drifters, and the zonal magnification is absent in the model over the southern half of the region.

Region 3 (35°N-40°N, 15°W-20°W): This is an area midway between the Azores and the southern coast of Spain. It characterizes most of the lower east between latitudes 40°N and 30°N, and most of the west basin between 30°N and 35°N. Both diagonal components of diffusivity are distinctly underestimated in this region. Drifter diffusivities are moderate, ranging from about $0.5x10^7$ cm^2/s^2 to $2.0x10^8$ cm^2/s^2. Both model and drifter diffusivities tend to plateau within 25 days. Inhomogeneities are seen in the drifter diffusivities at the extreme west and east boundaries, associated with the Gulf Stream and the Canary Current, respectively.

Region 4 (35°N-40°N, 15°W-20°W): This region is located at the edge of the North American Basin, paralleling the

Florida peninsula. It is representative of gradually rising diffusivities from east to west in the latitude band 20°N-30°N, but is distinct from the Gulf Stream region to the north in that the two components of diffusivity are roughly of the same magnitude, and the effects of inhomogeneities are not strong. The model underestimates diffusivities, particularly the meridional component, in this region, and excessive zonal autocorrelation is indicated in the model by the absence of plateaus.

As indicated by equation 13, the relative magnitudes of the eddy diffusivities seen in Figures 49 and 50 are related to the product of the zero-lag autocovariances and the Lagrangian integral time scales. The zero-lag autocovariances are mathematically equivalent (and computationally nearly equivalent) to the Eulerian variances.

In region 1 the integral time scales (see Figures 37, 38) are seen to be overestimated by a factor of about two. Meridional variances appear to be slightly underestimated by the model (Figures 18 and 19) while zonal variances are about half those of the model. This is consistent with the top two plots of Figure 49, which show nearly equal zonal components of diffusivity, while the model slightly exaggerates the meridional component. In region 2, zonal integral time scales are overestimated by a factor of about two, while meridional scales are roughly the same. Both components of variance are underestimated, but mainly in the

zonal direction. The result is that both diffusivity components are slightly smaller in the model, as shown in the bottom graphs of Figure 49. Region 3 shows model diffusivities to be significantly low (Figure 50). Time scales are nearly equal between model and data, but the distinctively low model variances in the eastern basin cause its diffusivities to be underestimated by over three times, as seen in the top plots of Figure 50. Finally, in region 4 the zonal time scale ratio is again about two and the meridional ratio nearly unity. Both variances are underestimated roughly by a factor of two, giving the expected result in diffusivities, as indicated by the bottom plots of Figure 50.

Though not shown, eddy diffusivity plots from the "random start" trajectories agree closely with those of the "same start" scheme over the entire study domain, reflecting the same patterns with respect to the drifter diffusivities.

THIS PAGE INTENTIONALLY LEFT BLANK

VI. CONCLUSIONS

Both Eulerian and Lagrangian comparisons are used in this study to explore the adequacy of the 1/6-degree POP model in representing the general surface circulation of the North Atlantic Ocean. A preliminary Eulerian analysis of the 1/10-degree model is done for a two-year subset of the period of the original data. The findings are in general agreement with previous studies of the North Atlantic circulation and comparisons of the model with various data sources.

The salient shortcomings of the 1/6-degree POP model are its under-representation of flow variability and spurious dynamic effects in the upper Gulf Stream and Subtropical Gyre. These in combination are the source of the discrepancies seen in comparison with our drifter data set.

The Eulerian comparisons show the 1/6-degree model to resolve the major flow features indicated by the drifters over the North Atlantic Ocean. The northern marginal currents are especially well modeled. Exceptions to the general agreement include the model's inaccurate representation of major direction changes in the Gulf Stream Extension, unrealistically high structure in the Subtropical Gyre's recirculation patterns, poor resolution of the Canary Current, and apparent inability to resolve the Azores Front. The effects of the model's artificial front in the southern Subtropical Gyre and anticyclone in the Gulf Stream between

Cape Hatteras and Cape Cod are clearly evident in the Eulerian plots.

The model's total contribution to MKE appears to be correct; drifter and model MKE histograms show almost identical frequency distributions as well. The spatial distribution of this energy seems to be perturbed by the model's artifacts and its inaccurate flow geometries in the Gulf Stream Extension, however. Energy is excessive where the Gulf Stream closely follows the continental shelf, and on the eastern side of the Mid Atlantic Ridge, where the model's Northwest Corner occurs. Elsewhere in the Gulf Stream MKE is underestimated. There is both overestimation and underestimation in the Subtropical Gyre, associated with the model's spurious front and its unresolved Azores Current, respectively. No significant tendency of underestimation or overestimation by the model as a function of energy level is found.

The 1/6-degree model appears to nearly uniformly under-represent variance about the surface mean flow, though the singularities of the model both amplify and diminish the contrast. The model's spurious anticyclone gives elevated values in the region 34°N-38°N, 70°W-76°W. The North Atlantic Current and northeast drift north of the Rockall Plateau appear closely matched in EKE. This result is misleading, though, because the model's displacement of the Northwest Corner produces reciprocal effects of underestimation and overestimation west and east,

respectively, of the Mid Atlantic Ridge. Comparisons in other areas are not complicated by the model's spurious effects; the continental boundary currents in the northeast Atlantic Ocean, for example, are unambiguously well modeled, while EKEs are clearly underestimated over most of the Subtropical Gyre and in the central Labrador Sea.

A frequency histogram shows a large overabundance of model EKE values below 50 cm^2/s^2 and too few above 1500 cm^2/s^2. As with MKE, the model shows no strong trend toward underestimating or overestimating EKE as a function of energy level.

The model represents eddy diffusivities fairly closely at latitudes north of 50N. With the exception of the Gulf Stream, diffusivities are distinctly underestimated by the model south of 50°N. Zonal diffusivities are also markedly underestimated in the Gulf Stream. These patterns, in conjunction with the model's nearly uniformly low variances, determine the spatial distribution of the integral length and time scales.

Inhomogeneities are most evident along the course of the Gulf Stream, and to a much lesser extent the other continental boundary currents; they generally appear less pronounced in the model than in the drifter data. Failure of diffusivities to reach plateaus within 25 days, indicating persistent temporal autocorrelation, is pronounced for the zonal-zonal component of model diffusivity over most of the mid and lower east basin and lower west basin.

The model's integral time scales are high, by average factors of about 1.9 and 1.8 in the zonal and meridional directions, respectively. Spatially, the overestimates occurred mostly in northern latitudes, with the Gulf Stream providing a demarcation over most of the northern basin. Zonal time scales are particularly overestimated in the latitude band range 20°N – 30°N. Meridional time scales are overestimated by factors upwards of three in latitudes south of 30°N.

Length scales are more closely matched; they are underestimated, but only by average factors of 1.1 and slightly greater than unity in the zonal and meridional directions, respectively. Again, the Gulf Stream divides higher values to the north and lower values to the south. The zonal length scale plots show the same band of elevated values in the latitude range 20°N – 30°N. A significant exception to the pattern of high time and length scales to the north is that the East Greenland Current is consistently well represented by the model.

For both Lagrangian integral time and length scales, spatial patterns shown by the "random start" and "same start" regimes are similar; frequency histograms also tally fairly closely for both regimes. We evidently do not incur substantial bias by sampling the model's velocity fields in a deterministic manner.

Preliminary Eulerian comparisons of the NOGAPS model run with the drifter data over the period January 1, 1993 – December 31, 1994 show a substantial improvement in EKE representation. The turbulence of the Subtropical Gyre is very well represented in the NOGAPS run, where the 1/6-degree model shows far too much structure in the surface flow. The Azores Current appears in the 1/10-degree model output, a result also noted by Smith et al. (1999), and the spurious front at latitudes 26°N – 30°N is much attenuated. The Northwest Corner appears in the correct longitude band, and the model's artificial anticyclone seems to be absent. There continues to be little evidence for the Canary Current in the 1/10-degree run, but this may be the result of the sparsity of the data; the current is also more poorly represented in the two-year subset of drifter data than in the full drifter data set.

Difficulties remain in connection with the energy balance for the NOGAPS formulation. While the overall distribution of EKE shows a large improvement over that of the 1/6-degree model, the different formulation apparently has the attendant effect of exaggerating MKE. Energies above 500 cm^2/s^2 are much more frequent than in the 1/6-degree model. Though the large surplus of EKE in the 0 – 50 cm^2/s^2 range is corrected in the 1/10-degree model, an overabundance of energy appears above 1000 cm^2/s^2. Geographically, there appears to be a meridional mismatch in EKE along the course of the Gulf Stream. The gradient of

EKE, in the "stream coordinate" sense, is too large along the southwest boundaries of the North American Basin. The region of elevated EKE where the Gulf Stream breaks from the continental shelf extends too far to the south and east; likewise, the region of high EKE associated with the Northwest Corner has an excessive peripheral reach.

The low variability of surface flow in the 1/6-degree model is probably attributable to its relatively low grid resolution and lack of a surface mixed layer. This study makes no attempt to discern the relative degrees of improvement in adding a mixed layer and increasing resolution. However, comparisons of sea level height data with a previous 1/10-degree run using ECMWF winds and no mixed layer (Smith et al., 1999) show improvement on about the same order as that which we observe. Resolution is therefore probably the dominant factor.

Evidently more experimentation is needed in order to achieve a more accurate distribution of EKE in the 1/10-degree model, particularly to attenuate the higher energies while still elevating energies out of the 0 to 50 cm^2/s^2 range. Ideally, this would done in a way that does not inflate MKE on the whole, as apparently occurs in the present version. Varying forcing frequencies, and friction coefficients may achieve an adequate decoupling of the two effects.

On the basis of Eulerian statistics, the 1/6-degree model appears to perform fairly well at latitudes above

60°N. Northern boundary currents are particularly well modeled. The major flow structures of the North Atlantic are well described by the 1/6-degree model over much of the domain, with the exceptions of the Gulf Stream Extension, the spurious anticyclone, and the Subtropical Gyre recirculation. Outside of these regions, the model mainly suffers from generally low variability, but even this is not pronounced over much of the upper latitudes. The Lagrangian integral time and length scales, on the other hand, tend to be overestimated in the upper latitudes, except for the southwest continental margin of Greenland.

Our overall assessment is that the generally low variability, limited feature resolution, displaced branching of the North Atlantic Current, and spurious circulation effects observed in the 1/6-degree model make it inadequate for use in an integrated global forecast system. Based on our preliminary results from the 1/10-degree run, we find this higher-resolution version to substantially correct the problems observed in the 1/6-degree model. It appears that the 1/10-degree model may well satisfy the requirements of the coupled global forecast system, and accordingly we recommend further testing at this resolution.

THIS PAGE INTENTIONALLY LEFT BLANK

APPENDIX A. CALCULATION OF THE SAMPLE
LAGRANGIAN VELOCITY AUTOCOVARIANCE FUNCTION

The following approach is that of Poulain et al.
(1996). As described in section V.A, the Lagrangian mean
velocity of an ensemble of particles is referenced to their
deployment from a single point $\mathbf{x}$ at a given time t_0. In
practice, buoys are not deployed from one location but
rather across an extended geographical area. Therefore, to
obtain the sample Lagrangian velocity autocovariance for a
collection of actual buoys in a given neighborhood, the
spatial domain of the definition is expanded (from zero) to
2 dimensions. Any buoy that inhabits the 2-dimensional area
at any time during its entire record is considered to
contribute to the "ensemble" of deployments within the
region. There is one "deployment" corresponding to each
time step spent in the region, however, each deployment is
considered to take place at the same reference time, t_0
(hence, we assume stationarity). For our purposes, the
specific value of t_0 is irrelevant and set to zero.

Consider a buoy whose displacements from an arbitrary
point are measured over a discrete time interval [m,n] as
$(\mathbf{r}_m, \mathbf{r}_{m+1}, \mathbf{r}_{m+2}, ..., \mathbf{r}_n)$. Let some contiguous segment $(\mathbf{r}_i, \mathbf{r}_{i+1}, \mathbf{r}_{i+2}, ..., \mathbf{r}_j)$
of its track pass through the region of interest, and
suppose the sample Lagrangian autocovariance function over a
time lag interval $[-\tau, \tau]$ is sought for that region. Then

that segment's contribution to the function is derived from
the series of overlapping "pseudotracks" given by

$$\left(\mathbf{r}_{i-\tau},\mathbf{r}_{i-(\tau-1)},\mathbf{r}_{i-(\tau-2)},\ldots,\mathbf{r}_{i-2},\mathbf{r}_{i-1},\mathbf{r}_{i},\mathbf{r}_{i+1},\mathbf{r}_{i+2},\ldots,\mathbf{r}_{i+(\tau-2)},\mathbf{r}_{i+(\tau-1)},\mathbf{r}_{i+\tau}\right)$$

$$\left(\mathbf{r}_{(i+1)-\tau},\mathbf{r}_{(i+1)-(\tau-1)},\mathbf{r}_{(i+1)-(\tau-2)},\ldots,\mathbf{r}_{(i+1)-2},\mathbf{r}_{(i+1)-1},\mathbf{r}_{i+1},\mathbf{r}_{(i+1)+1},\mathbf{r}_{(i+1)+2},\ldots,\mathbf{r}_{(i+1)+(\tau-2)},\mathbf{r}_{(i+1)+(\tau-1)},\mathbf{r}_{(i+1)+\tau}\right)$$

$$\vdots$$

$$\left(\mathbf{r}_{(j-1)-\tau},\mathbf{r}_{(j-1)-(\tau-1)},\mathbf{r}_{(j-1)-(\tau-2)},\ldots,\mathbf{r}_{(j-1)-2},\mathbf{r}_{(j-1)-1},\mathbf{r}_{j-1},\mathbf{r}_{(j-1)+1},\mathbf{r}_{(j-1)+2},\ldots,\mathbf{r}_{(j-1)+(\tau-2)},\mathbf{r}_{(j-1)+(\tau-1)},\mathbf{r}_{(j-1)+\tau}\right)$$

$$\left(\mathbf{r}_{j-\tau},\mathbf{r}_{j-(\tau-1)},\mathbf{r}_{j-(\tau-2)},\ldots,\mathbf{r}_{j-2},\mathbf{r}_{j-1},\mathbf{r}_{j},\mathbf{r}_{j+1},\mathbf{r}_{j+2},\ldots,\mathbf{r}_{j+(\tau-2)},\mathbf{r}_{j+(\tau-1)},\mathbf{r}_{j+\tau}\right)$$

where velocity information is available for all pseudotrack
elements whose time indices are within the time domain [m,n]
of the track.   Velocities for elements whose indices fall
outside the time domain are assigned null values.   This
process is repeated for all track segments that pass through
the region, generating one velocity time series for each
observation. For the kth discrete lag τ_k in $[-\tau,\tau]$, the
"ensemble average" $\mathbf{V}(\tau_k,t_0,\mathbf{x})$ = $<\mathbf{v}(t_0+\tau_k|\mathbf{x},t_0)>_L$ is then
computed as the mean of the non-null velocities
corresponding to the kth pseudotrack elements. The residuals
$\mathbf{v}'(t_0+\tau_k|\mathbf{x},t_0)$ about the kth lag averages follow directly,
where the zero-lag residual is the special case $\mathbf{v}'(t_0|\mathbf{x},t_0)$.
The value of the sample Lagrangian autocovariance function
at time lag τ_k for components i and j (where i and j may be
either zonal or meridional) is then given by the mean of the
cross-products $v_i'(t_0+\tau_k|\mathbf{x},t_0)\ v_j'(t_0|\mathbf{x},t_0)$.

128

APPENDIX B. NUMERICAL GENERATION OF PARTICLE TRAJECTORIES USING THE RUNGE-KUTTA METHOD

The generation of numerical particle trajectories for the "random start" and "same start" schemes involves a series of initial value problems to the first order differential equation

$$\mathbf{v}(t) = f(\mathbf{r}, t), \quad \mathbf{r}(0) = \mathbf{r}_0.$$

Here, $\mathbf{r}$ is a displacement vector defined over the spatial domain of the model, and $\mathbf{v}$ is a velocity vector obtained by bilinear interpolation of the model velocity field at $\mathbf{r}$. Given displacement $\mathbf{r}(t)$ at time t, the displacement $\mathbf{r}(t+\Delta t)$ at time $t + \Delta t$, is given by

$$\mathbf{r}(t+\Delta t) = \mathbf{r}(t) + \int_{t}^{t+\Delta t} \mathbf{v}(\mathbf{r}, t')dt'.$$

For the model's discrete time step Δt, a practical algorithm for advancing a solution from $\mathbf{r}(t)$ to $\mathbf{r}(t+\Delta t)$ employs the fourth order Runge-Kutta method, described in detail in Press et al. (1992). The method derives from the simpler Euler Method, which uses the first term of the Taylor expansion of $\mathbf{r}$ about t. In the context of our problem this results in the familiar formula

$$\mathbf{r}(t+\Delta t) = \mathbf{r}(t) + \mathbf{v}(\mathbf{r}, t)\Delta t.$$

The disadvantage of the Euler method is that it uses derivative information (**v**) only at the start of the time interval. The method has an error only one power smaller than the error of the time step, or $O((\Delta t)^2)$. A more stable and accurate method uses the derivative at time t to take a step to the midpoint **r**(t+Δt/2) of the interval. The derivative **v**(**r**(t+Δt/2), t+Δt/2) is then substituted for the original **v**(r,t) to extrapolate to the next point; mathematically,

$$\mathbf{k}_1 = \mathbf{v}(\mathbf{r},t)\Delta t,$$

$$\mathbf{k}_2 = \mathbf{v}(\mathbf{r} + \frac{1}{2}\mathbf{k}_1, t + \frac{1}{2}\Delta t),$$

$$\mathbf{r}(t + \Delta t) = \mathbf{r}(t) + \mathbf{k}_2 + \mathbf{O}((\Delta t)^3).$$

The error term $O((\Delta t)^2)$ is eliminated by symmetry, giving higher accuracy. The fourth order Runge-Kutta method (a method is called n^{th} order if its error term is of order n+1) uses similar symmetric canceling with derivatives evaluated at the initial point, twice at trial midpoints, and once at a trial endpoint. The result is

$$k_1 = v(r,t)\Delta t,$$

$$k_2 = v(r + \frac{1}{2}k_1, t + \frac{1}{2}\Delta t)\Delta t,$$

$$k_3 = v(r + \frac{1}{2}k_2, t + \frac{1}{2}\Delta t)\Delta t,$$

$$k_4 = v(r + k_3, t + \Delta t)\Delta t,$$

$$r(t + \Delta t) = r(t) + \frac{k_1}{6} + \frac{k_2}{3} + \frac{k_3}{3} + \frac{k_4}{6} + O((\Delta t)^5).$$

The method is illustrated graphically in Figures 51 and 52.
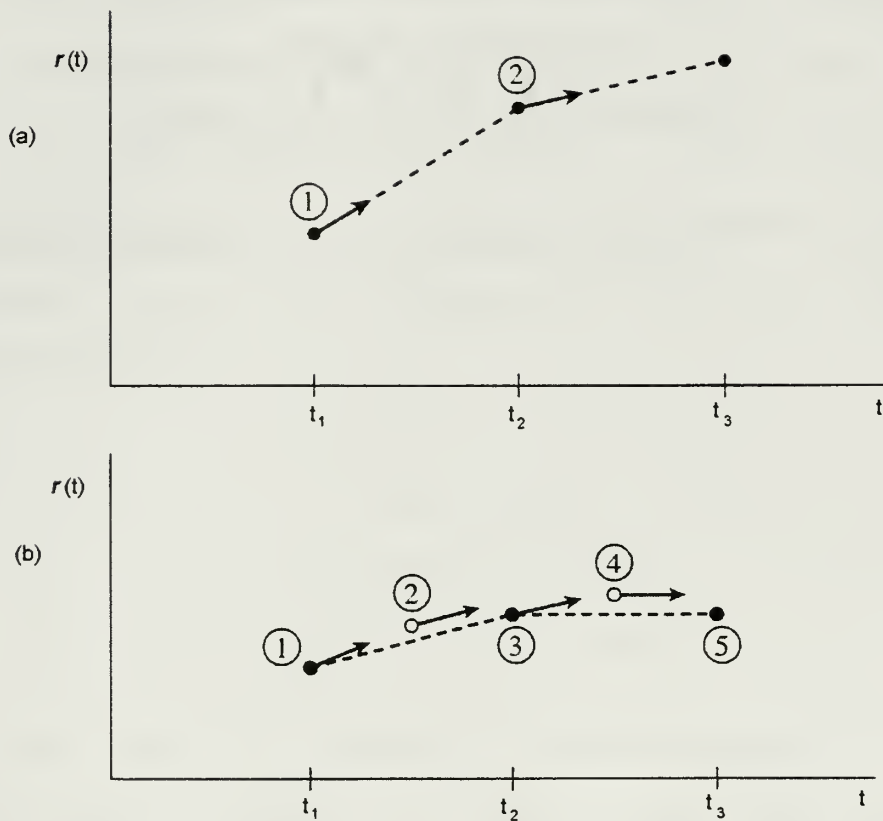
Figure 51. The Euler and Midpoint methods for numerical integration of ordinary differential equations. The notation is adapted to the problem of generating trajectories. The dependent variable, **r**, is actually two-dimensional. Plot (a) illustrates the Euler method, which uses derivative ($v(t)$) information only at the lower endpoint of the time interval to advance the solution to the next point. Plot (b) shows the more accurate midpoint method, in which the derivative at the lower endpoint is used to take a trial step to the midpoint of the interval. The derivative at the midpoint is then used to extrapolate the function value over the interval. After Press et al., (1992).

132
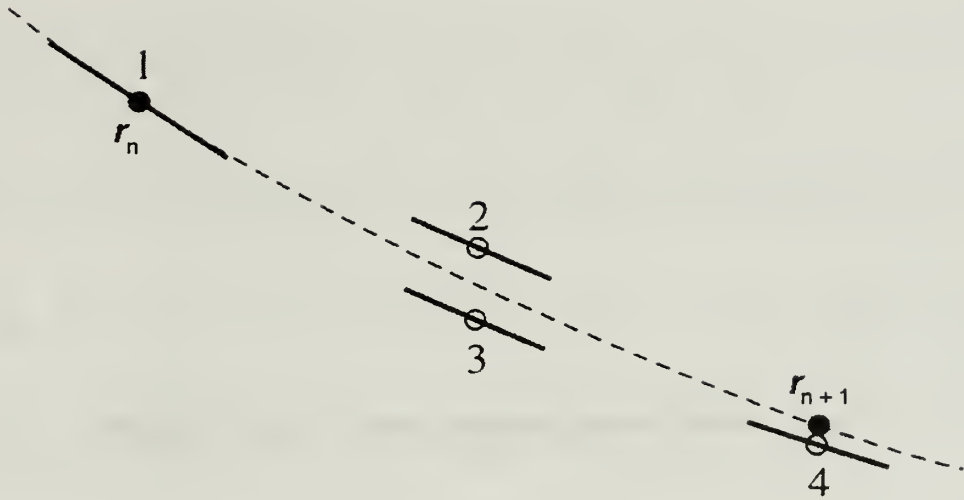
Figure 52. The Fourth Order Runge-Kutta method, used to
generate simulated trajectories for the "same start" and
"random start" schemes. The method is based on the Euler and
Midpoint methods, but uses derivative information once at
the lower endpoint of the interval, twice at trial
midpoints, and once at the endpoint. The four derivatives
are then used to advance the solution across the interval.
After Press et al. (1992).

THIS PAGE INTENTIONALLY LEFT BLANK

LIST OF REFERENCES

Auer, S. J., 1987: Five-year climatological survey of the Gulf Stream system and its associated rings, *J. Geophys. Res.*, **92**, 11,709-11726.

Barnier, B., L. Siefridt, and P. Marchesiello, 1995:Thermal forcing for a global ocean circulation model using a three-year climatology of ECMWF analyses, *J. Marine. Sys.*, **6**, 363-380.

Bryan, K., 1969: A numerical method for the study of the circulation of the world ocean, *J. Comput. Phys.*, **4**, 347-376.

Chao, Y., A. Gangopadyay, F. O. Bryan, and W. R. Holland, 1996: Modeling the Gulf Stream system: how far from reality?, *Geophys Res. Lett.*, **22**, 3155-3158.

Colin de Verdière, A., 1983: Lagrangian eddy statistics from surface drifters in the eastern North Atlantic, *J. Mar. Res.*, **41**, 375-398.

Cox, M. D., 1970: A mathematical model of the Indian Ocean, *Deep Sea Res.*, **17**, *45-75*.

Cox, M. D., 1984: A primitive equation three dimensional model of the ocean, GFDS Ocean Group Tech. Rep. 1, Geophys. Fluid Dyn. Lab./NOAA, Princeton Univ., Princeton, N. J., 250 pp.

Davis, R. E., 1991: Observing the general circulation with floats, *Deep-Sea Res.*, **38**, Suppl. 1, S531-S571.

Dukowicz, J. K., and R. D. Smith, 1994: Implicit free-surface method for the Bryan-Cox-Semtner ocean model, *J. Geophys. Res.*, **99**, 7991-8014.

Freeland, H. J., P. B. Rhines, and T. Rossby, 1975: Statistical observations of the trajectories of neutrally buoyant floats in the North Atlantic, *J. Mar. Res.*, **33**, 383-404.

Fu, L., and R. Smith, 1996: Global ocean circulation from satellite altimetry and high-resolution computer simulation, *Bull. Am. Meteorol. Soc.*, **77**, 2625-2636.

Gianetti, P., *The Velocity Field in the Northeast Atlantic from Satellite-Tracked Drifting Buoys*, Master's Thesis, Naval Postgraduate School, Monterey, California, September 1993.

Hansen, D. V., and P.-M. Poulain, 1996: Quality control and interpolations of WOCE-TOGA drifter data, *J. Atmos. and Oceanic Tech.*, **13**, *900-909*.

Johns, W. E., T. J. Shay, J. M. Bane, and D. R. Watts, 1995: Gulf Stream structure, transport, and recirculation near 68°W, *J. Geophys. Res.*, **100**, 817-838.

Killworth, P. D., D. Stainforth, D. J. Webb, and S. M. Patterson, 1991: The development of a free-surface Bryan-Cox-Semtner ocean model, *J. Phys. Oceanogr.*, **21**, 1333-1348.

Krauss, W., and R. H. Käse, 1984: Mean circulation and eddy kinetic energy in the eastern North Atlantic, *J. Geophys. Res.*, **89**, 3407-3415.

Krauss, W., 1986: The North Atlantic Current, *J. Geophys. Res.*, **91**, 5061-5074.

Krauss, W., 1995: Currents and mixing in the Irminger Sea and in the Iceland Basin, *J. Geophys. Res.*, **100**, 10851-10871.

Krauss, W., and C. W. Böning, 1987: Lagrangian properties of eddy fields in the northern North Atlantic as deduced from satellite-tracked buoys, *J. Mar. Res.*, **45**, 259-291.

Large, W. G., J. C. McWilliams, and S. C. Doney, 1994: Oceanic vertical mixing: a review and a model with a nonlocal boundary layer parameterization, *Reviews of Geophysics*, **32**, 363-403.

Larson, J. C., and M. Bushnell, 1995: Decadal transport changes in the Florida Current, *Proceedings from the principal investigators meeting, Atlantic Climate Change Program*/ NOAA, University of Miami, Miami, FL, 203 pp.

Lemon, M. R., *Comparison of Los Alamos National Laboratory (LANL) Parallel Ocean Program (POP) Model Fields with Pacific Surface Drifter Measurements*, Master's Thesis, Naval Postgraduate School, Monterey, California, September 1997.

Levitus, S., 1982: Climatological atlas of the world ocean, *NOAA Prof. Pap.* **13**, *193 pp*.

Maltrud, M. E., and R. D. Smith, 1998: Global eddy-resolving ocean simulations driven by 1985-1995 atmospheric winds, *J. Geophys. Res.*, **103**, 30825-30853.

McClean, J. L., and A. J. Semtner, Comparisons of mesoscale variability in the Semtner-Chervin 1/4° model, the Los Alamos Parallel Ocean Program 1/6° model, and TOPEX/POSEIDON data, *J. Geophys. Res.*, **102**, 25203-25226.

Milliff, R. F., W. G. Large, W. R. Holland, and J. C. McWilliams, 1996: The general circulation responses of high-resolution North Atlantic Ocean models to synthetic scatterometer winds, *J. Phys. Oceanogr.*, **26**, 1747-1768.

Niiler, P. P., 1995: Global Drifter Program: measurements of velocity, SST, and atmospheric Pressure, *International WOCE Newsletter*, **20**, 3-6.

Niiler, P. P., and W. S. Richardson, 1973: Seasonal variability of the Florida Current, *J. Mar. Res.*, **31**, 144-167.

Niiler, P. P., A. S. Sybrandy, K. Bi, P.-M. Poulain, and D. Bitterman, 1995: Measurements of the water-following capability of holey-sock and TRISTAR drifters, *Deep-Sea Res.*, **42**, 1951-1964.

Otto, L., and H. M. Van Aken, 1996: Surface circulation in the northeast Atlantic as observed with drifters, *Deep-Sea Res.*, **43**, 467-499.

Pickard, G. L., and Emery, W. J., *Descriptive Physical Oceanography. An Introduction.* Pergamon Press, 1990.

Poulain, P.-M., 1993: Estimates of horizontal divergence and vertical velocity in the equatorial Pacific, *J. Phys. Oceanogr.*, **23**, 601-607.

Poulain, P.-M., A. Warn-Varnas, and P. P. Niiler, 1996: Near-Surface circulation of the Nordic seas as measured by Lagrangian drifters, *J. Geophys. Res.*, **101**, 18237-18258.

Press, W. S., Teukolsky, W. Vetterling, and B. Flannery, *Numerical Recipes in Fortran 77*, Cambridge Univ. Press, London, 1992.

Richardson, P. L., 1983: Eddy kinetic energy in the North Atlantic from surface drifters, *J. Geophys. Res.*, **88**, 4355-4367.

Semtner, A. J., 1974: An oceanic general circulation model with bottom topography, Tech. Rep. 9, Dept. of Meteorol., Univ. of Calif., Los Angeles, 99 pp.

Semtner, A. J., 1997: Very high-resolution estimates of global ocean circulation, suitable for carbon-cycle modeling, *Proceedings of the 1993 Snowmass Global Change Institute on the Global Carbon Cycle*, T. Wigley, ed., Cambridge Univ. Press., 217 pp.

Semtner, A. J., and R. M. Chervin, 1988: A simulation of the global ocean circulation with resolved eddies, *J. Geophys. Res.*, **93**, 15502-15522 and 15767-15775.

Service Argos, 1984: Location and Data Collection Satellite System User's Guide, Tech. Report, Service Argos, 36 pp.

Smith, R. D., J. K. Dukowicz, and R. C. Malone, 1992: Parallel ocean circulation modeling, *Physica D*, **60**, 38-61.

Smith, R. D., Maltrud, M. E., Bryan, F. O., and M. W. Hecht, 1999: Numerical simulation of the North Atlantic ocean at 1/10º, *J. Phys. Oceanogr.*, Submitted.

Seber, G. A. F., *Multivariate Observations*, John Wiley and Sons, 1984.

Sybrandy, A. S. and P. P. Niiler, 1991: The WOCE/TOGA SVP Lagrangian drifter construction manual. SIO Ref. 91/6, WOCE Report No. 63/91, 58 pp.

Taylor, G. I., 1921: Diffusion by continuous movements, *Proc. London Math. Soc.*, **20**, *196-212*.

Tokmakian, R., 1996: Comparisons of time series from two global models with tide-gauge data, *Geophys. Res. Lett.*, **23**, 3759-3762.

Tomczak, M., and J. S. Godfrey, 1994: *Regional Oceanography: an Introduction*. Pergamon Press, Tarrytown, NY. 422 pp.

Treguier, A. M., 1992: Kinetic energy analysis of an eddy resolving, primitive equation model of the North Atlantic, *J. Geophys. Res.*, **97**, 687-701.

Wilken, J. L., and R. A. Morrow, 1994: Eddy kinetic energy and momentum flux in the Southern Ocean: Comparison of a global eddy-resolving model with altimeter, drifter, and current-meter data, *J. Geophys. Res.*, **99**, 7903-7916.

Worthington, L, V., 1976: On the North Atlantic circulation, Johns Hopkins Oceanographic Studies, No. 6, 110 pp.

INITIAL DISTRIBUTION LIST

No. Copies

1. Defense Technical Information Center 2
    8725 John J. Kingman Rd., Ste 0944
    Cameron Station
    Ft. Belvoir, VA 22060-6218

2. Dudley Knox Library 2
    Naval Postgraduate School
    411 Dyer Rd.
    Monterey, CA 93943-5101

3. Superintendent 1
    Attn: Professor Roland W. Garwood
    Code OC/Gd
    Naval Postgraduate School
    411 Dyer Rd.
    Monterey, CA 93943-5000

4. Superintendent 1
    Attn: Professor Richard E. Rosenthal
    Code OR/Rl
    Naval Postgraduate School
    411 Dyer Rd.
    Monterey, CA 93943-5000

5. Superintendent 1
    Attn: Research Assistant Professor J. L. McClean
    Code OC/Mn
    Naval Postgraduate School
    411 Dyer Rd.
    Monterey, CA 93943-5000

6. Superintendent 2
    Attn: Assistant Professor P.-M. Poulain
    Code OC/Pn
    Naval Postgraduate School
    411 Dyer Rd.
    Monterey, CA 93943-5101

7. Superintendent 1
    Attn: Professor Albert Semtner
    Code OC/Se
    Naval Postgraduate School
    411 Dyer Rd.
    Monterey, CA 93943-5101

8. Dr. Mark S. Swenson 1
    National Oceanic and Atmospheric Administration
    Atlantic Oceanographic and Meteorological Laboratory
    4301 Rickenbacker Causeway
    Miami, FL 33149

9. Mr. R. Michael Clancy 1
    Fleet Numerical Meteorology and Oceanography Center
    Code 400A
    7 Grace Hopper Rd. Stop 1
    Monterey, CA 93943-5501

10. Dr. Steve Piascek 1
    Code 7320
    Stennis Space Center
    MS 39529

11. Dr. Matthew W. Maltrud 1
    Los Alamos National Laboratory
    MS B216
    Los Alamos, NM, 87545

12. Dr Theresa Paluszkiewicz 1
    Office of Naval Research
    Code 32, Boston Tower 1, Rm 428-3
    800 North Quincy St.
    Arlington VA 22217-5660